MICROSTRUCTURE CHARACTERIZATION, MECHANICAL PROPERTIES, AND CORROSION BEHAVIORS OF FRICTION STIR WELDED AA5086 AND AA6061

A THESIS SUBMITTED TO THE GRADUATE DIVISION OF THE
UNIVERSITY OF HAWAIʻI AT MĀNOA IN PARTIAL FULFILLMENT
OF THE REQUIREMENTS FOR THE DEGREE OF

MASTER OF SCIENCE
IN
MECHANICAL ENGINEERING

August 2014

By

Zhitong Chen

Thesis Committee:

Lloyd H. Hihara, Chairperson

Scott F. Miller

Jingjing Li

Keywords: Corrosion, Friction Stir Weld, Aluminum Alloy, Mechanical Properties

ACKNOWLEDGEMENTS

I would like to express my sincere gratitude and respect to my advisor, Dr. Lloyd H. Hihara, for his support, endless enthusiasm and encouragement. This thesis has benefited immensely from his comments, reviews, and opinions. I would like to thank him for his time, patience, and help. I also would like to thank Dr. Scott F. Miller and Dr. Jingjing Li for serving as my thesis committee members.

I would like to express my appreciation to my colleagues Mr. Ryan Sugamoto, Dr. Atul Tiwari, Dr. Shengxi Li, Dr. Raghu Srinivasan, Dr. Shruti Tiwari, Ms. Jan Kealoha, and Mr. Daniel Hong of the Hawaii Corrosion Lab for their valuable contributions. I am thankful to Dr. Scott F. Miller and Mr. Jonathan Jaberina for friction-stir-weld jointing sheets of aluminum alloy. I am also thankful to Mr. Aaron Toyama from the engineering shop and Joanne Yee from Department of Mechanical Engineering.

I am grateful for support of the financial support from the Office of the Under Secretary of Defense for the project entitled **"**Correlation of Field and Laboratory Studies on the Corrosion of Various Alloys in a Multitude of Hawaii Micro-Climates**"** (U.S. Air Force Academy, Contract no.: FA7000-10-2-0010). The authors are particularly grateful to Mr. Daniel Dunmire, Director, Corrosion Policy and Oversight, Office of the Under Secretary of Defense.

Finally, I would like to express my love and affection to my parents for their enduring love and encouragement.

ABSTRACT

The objective of this research was to study microstructure characterization, mechanical properties, and corrosion behavior of friction stir welding AA5086 and AA6061. The microstructure of six distinct zones (NZ, TMAZ, HAZ, BM, downside, and cross-section) of friction stir welding AA5086-AA5086, AA5086-AA6061, and AA6061-AA6061 were investigated using etching technology and optical microscope. The hardness of friction stir welding AA5086-AA5086, AA5086-AA6061, and AA6061-AA6061 was measured by Wilson Rockwell Vickers Micro-hardness Tester to study how distinct regions affect mechanical properties. Tensile tests were conducted to study tensile and yield strength of friction stir welding AA5086-AA5086, AA5086-AA6061, and AA6061-AA6061. The results indicate that the fracture occurred in the relatively weaker TMAZ/HAZ.

In this study, two major corrosion evaluation methods were used: the polarization test and the immersion test. Polarization experiments of critical regions of friction stir welding AA5086-AA5086, AA5086-AA6061, and AA6061-AA6061 were conducted in deaerated 3.15 wt% NaCl to study the governing corrosion mechanisms. Cathodic polarization of critical zones of friction stir welding AA5086-AA5086, AA5086-AA6061, and AA6061-AA6061 were conducted in aerated 3.15 wt% NaCl and 0.5 M Na_2SO_4 solutions. These results show that friction stir welding improves the corrosion resistance of AA5086 and AA6061 and that the HAZ and downside regions have better corrosion resistance than other regions. The immersion experiments were conducted to study corrosion properties of friction stir welding AA5086-AA5086, AA5086-AA6061, and AA6061-AA6061. Specimens of friction stir welding AA5086-AA5086, AA5086-AA6061, and AA6061-AA6061 were soaked in 3.15 wt% NaCl, 0.5 M Na_2SO_4 and

American Society for Testing and Materials (ASTM) seawater for 90 days and 120 days at 30°C. The X-Ray Diffraction (XRD) and Raman spectroscopy were used to characterize the immersion samples and revealed that aluminum hydroxide was the main corrosion product. Intergranular attack was observed in the NZ and downside by scanning electron microscopy (SEM).

Keywords: Corrosion, Friction Stir Weld, Aluminum Alloy, Mechanical Properties

Contents

List of Tables

List of Figures

Chapter 1

Introduction

Friction stir welding (FSW), a new solid state joining technique, was invented by The Welding Institute in 1991 [1]. This technique is now increasingly used to join a wide range of aluminum alloys for numerous applications because there is far lower heat input during the process than with conventional welding methods such as insert gas and metal insert gas (MIG). This solid-state process leads to minimal microstructural changes and better mechanical properties than does conventional welding [2-4]. FSW is used in critical load-bearing structures, and the corrosion at the welds in these structures can have severe consequences. Therefore, it is critical to evaluate and understand corrosion behavior as well as mechanical properties of these welds. Few studies have taken into consideration the microstructure and corrosion of FSW joints of AA5086-AA5086, AA5086-AA6061, and AA6061-AA6061.

1.1 Objectives of this Study

The areas of focus in this project were as follows:

- to characterize the microstructure of FSW joints of AA5086-AA5086, AA5086-AA6061, and AA6061-AA6061;
- to study mechanical properties of FSW joints of AA5086-AA5086, AA5086-AA6061, and AA6061-AA6061; and
- to assess the corrosion properties and mechanism of FSW joints of AA5086-AA5086, AA5086-AA6061, and AA6061-AA6061 Al alloys in various environmental conditions.

Chapter 2

Literature Review

2.1 Friction Stir Welded

Aluminum alloys, which can be difficult to weld with conventional fusion welding, are used extensively in aerospace, automotive, and marine applications. FSW is a solid-state joining technique invented by TWI in 1991 [1]. The technique involves a non-consumable cylindrical tool rotating at a very high speed and plunging into adjacent edges of the alloys pieces, thereby joining them. The basic principle of FSW is shown in Figure 2.1. The two workpieces to be welded are brought into contact, positioned on a backing plate and securely clamped. When a cylindrical rotating tool is inserted into the workpieces, frictional heating occurs that brings the two workpieces to a plasticized state. Due to the tool translating along the joint line, the material is stirred and forged behind the trailing face of the pin, where it consolidates and cools down to form a solid-state weld.

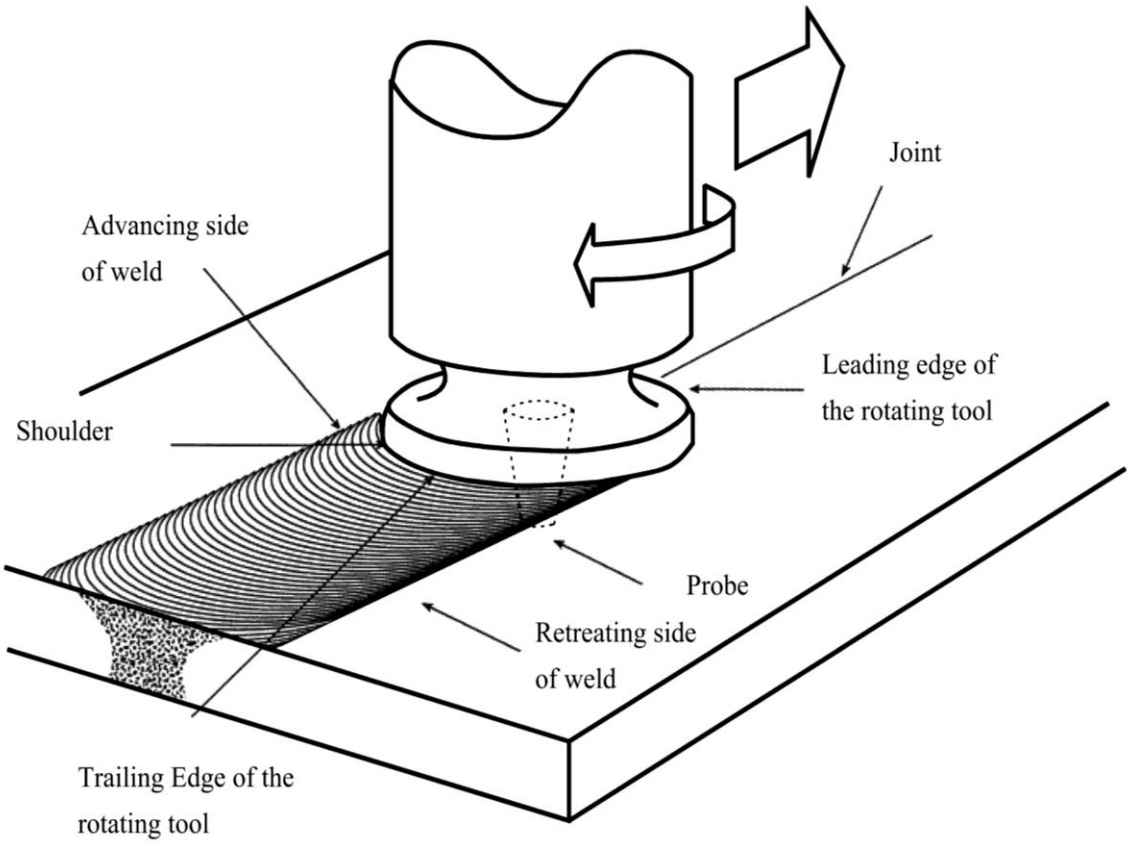

Figure 2.1 Friction stir welding technique [5]

The high frictional temperatures are below the melting temperature but are sufficient to produce plastic deformation necessary for welding. Therefore, no filler wire or shielding gas is required and up to 10% weight is saved in comparison to conventional welding [6]. This is an environmentally benign process and there does not require external cutting fluids or generate metal chips. During this solid state welding process, problems such as liquation cracking, porosity, and distortion that take place during other welding process viz. tungsten insert gas (TIG) and MIG do not occur [7, 8]. In addition, FSW leads to improved mechanical properties at the weld that is not possible with conventional joining techniques such as TIG and MIG. FSW also reduces the residual stress in the weld.

Additionally, the microstructure of the weld is significantly modified due to severe plastic deformation.

2.2 Microstructure

Frictional heat causes the alloys to soften and allows the tool to traverse along the joint line. As described by numerous authors, the welded joint of aluminum alloy is composed of four distinct zones [9-14]: the nugget zone (NZ), the thermomechanical-affected zone (TMAZ), the heat-affected zone (HAZ) and the base material (BM). NZ is a region of heavily deformed material that corresponds to the location of the pin during welding. The grains within NZ are generally equiaxed and an order of magnitude smaller than the grains in the BM. In the TMAZ region, which occurs on either side of the NZ, the strain and the temperature are lower than in the NZ. The effect of welding on the microstructure of the TMAZ is correspondingly smaller. Unlike in the NZ, the microstructure in the TMAZ is similar to that of the BM, although it is significantly deformed and rotated. The HAZ is common to all welding processes subjected to a thermal cycle, but it is not deformed during welding. The temperatures in the HAZ are lower than those in the TMAZ, but they may still have a significant effect on the microstructure. The BM is unaffected by the welding process.

When Wadeson et al. [15] examined the microstructure of FSW AA7108 T79 aluminum alloy, they found that the NZ consisted of relatively fine and equiaxed grains with an average size of 3–6 μm. The average grain size within the TMAZ is about 5–20 μm. The HAZ exhibited a more elongated grain structure than the other weld zones. Its grain length and width is 10–40 μm and 5–15 μm, respectively. The size of shape of grains of

the BM AA7108 T79 aluminum alloy is 10–40 μm long and 3–5 μm wide. Peak temperatures in different regions were reported to range from 200– 475 °C [16, 17]. The NZ experiences the highest temperature, while the lowest temperature is in the section of unaffected BM. The temperature reached within the TMAZ is sufficient to cause dissolution of precipitates. They also indicate that the edge regions of the TMAZ are the most susceptible to corrosion.

Jariyaboon et al. [4] investigated the effect of welding parameters on the microstructure of FSWAA2024-T351. The NZ consisted of fine equiaxed grains because of dynamic recrystallization [18-20], and the boundary between the NZ and the TMAZ regions showed a severe deformation of the grains. The grains are re-orientated due to the stirring action of the toolpiece pin. These researchers also indicated that the TMAZ/NZ boundary on the advancing side was slightly sharper than on the retreating side [21, 22]. The HAZ showed characteristic elongated grains of the BM. They also indicated that the welding parameters, especially rotation speed, affected the grain size in the NZ. Grain size can be maintained with changing travel speed at a fixed rotation speed, but it increased as the rotation speed accelerated and the fixed travel speed remained constant [23]. The corrosion attack was in the NZ due to the significant anodic reactivity in the HAZ because of the sensitized grain boundaries [3, 24].

In Fonda et al.'s [25] study of the microstructure of FSW AA5456 they learned that the NZ was well defined at the center, and the TMAZ was identified by the upward deflection of grains on each side of the NZ [26, 27]. In the HAZ, the density and distribution of precipitates were similar to those of the BM. In the welding process, the mobility of the dislocations increases as the temperature increases, a process that allows

the dislocations to migrate, coalesce, and form subgrain boundaries—proof that HAZ exhibited a gradual transition. The TMAZ grains, which have grain boundaries preferentially aligned with the precipitate orientation direction, are larger than the grains in HAZ and BM. The corrosion attack, which occurred primarily in the NZ, was markedly asymmetric. The advancing side of the NZ exhibited more corrosive attack, particularly towards the base of the NZ. The retreating side had less corrosion than did the top of the weld.

2.3 Mechanical Properties

Adjacent edges of the aluminum pieces plunged into by a high speed rotating non-consumable cylindrical pin create severe plastic deformation, which significantly modifies the mechanical properties and overall performance of the weld. Xu et al. [28] studied the mechanical properties of FSW thick AA2219-O joints. The maximum hardness was 95 HV (100g) in NZ at the weld top on the advancing side. The minimum vale was obtained at the BM. Xu et al. also shows that the weld top was much harder than the weld bottom. Fine recrystallized grains formed in the NZ and the grains in the TMAZ were elongated and bended [29]. The grains in the HAZ are smaller than the BM. The NZ has a much higher hardness than does the BM, a difference than can be explained by the Hall-Petch relationship [30]. Due to the non-uniform plastic flow field in two sides of weld center, maximum hardness in the NZ is on the advancing side rather than in the weld center [31]. Because the larger distorted grains and distortion energy causes strain-hardening, such hardness is asymmetrically distributed through the weld centerline.

Bala Srinivasan et al. [32] reported on mechanical properties and corrosion behavior of friction stir welded AA2219. They found that the hardness of the NZ was between 85–110 $HV_{0.5}$ and that the hardness of the TMAZ/HAZ region adjoining the NZ is lower than the NZ in range of 80–90 $HV_{0.5}$. The hardness of BM was 155 ± 5 $HV_{0.5}$ and the hardness gradient between the BM and the TMAZ/HZ was steep. It is notable that the variation in hardness in the NZ of welds cannot be attributed to Hall-Petch relationship since the smaller grain size of FSW gives a lower hardness [30, 33]. Bala Srinivasan et al. also found that the perceptible variations in the grain size in the NZ did not influence the hardness of the NZ.

Cho et al. [34] examined the mechanical properties during FSW of AA5083. They discovered a minor local variation in the hardness value around 100 HV (4.9 N). A steady hardness distribution was obtained across the welding region, making it difficult to differentiate the hardness of HAX, TMAZ and NZ. The redistribution of the second particles during the FSW process plays a crucial role in the strengthening of welded materials [35, 36]. Homogeneously distributed fine particles of Al_6 (Mn, Fe, Cr) inside grains in the welded region seem to play a more dominant role in the hardness.

When Hatamleh et al. [37] investigated the mechanical properties and corrosion susceptibility of FSW AA7075 joints, they discovered the “W” shaped hardness distribution characteristic of friction stir welds in precipitation hardening alloys. The minimum value of hardness that appeared in the advancing and retreating sides of the HAZ occurred because peak temperatures in those regions were optimal for precipitate coarsening. The variations in hardness are relative to the microstructure developed after the welding process. In a tensile test, the lowest properties appeared in the TMAZ at the

retreating side of the weld. The highest tensile values corresponded to the NZ. The reason for reduction in tensile properties at the TMAZ might be the coarsening or resolution of strengthening precipitates as a result of the welding process.

Hu et al. [38] conducted a quantitative investigation of the tensile plastic deformation for FSW AA2024. The fracture of the specimens occurred at the BM on the advancing side. By comparison with the BM, longitudinal tensile specimens of FSW joints exhibited a significant increased in both tensile and yield strength, while the ductility was unaffected. The observed plastic deformation behavior of the FSW joints was closely related to the micro-hardness. The grain size and precipitate distribution greatly affected the mechanical properties of the precipitation-hardening aluminum alloys [39]. Because the density of the precipitates in HAZ was slight higher than in the BM, the HAZ was stronger than the BM. During the welding thermal cycle, the dissolution and growth of strengthening precipitates in the weld zone worsened the mechanical properties [40-42]. However, the TMAZ which contained homogenously distributed precipitates showed a different result, and its strength was higher than the HAZ. The strength of NZ which contained higher dislocation density and finer dispersed precipitates was the highest due to intense plastic deformation, frictional heating, and dynamic recrystallization [35, 43, 44].

Srinivasan et al. [45] studied strain rate tensile behavior of FSW AA7075-AA6056 in a 3.5% NaCl solution at 20 °C at two strain rates— $10^{-6}s^{-1}$ and $10^{-7}s^{-1}$. For the first, a reduction in the TMAZ/HAZ of the AA6056 side occurred as well in the NZ towards the AA6056 side. The NZ towards to the AA6056 alloy side underwent a considerable degree of plastic deformation, while the failure was only in the TMAZ/HAZ of the

AA6056. A reduction value was 50±2%, which means that when immersed in the 3.5% NaCl solution, there was no stress corrosion cracking. There were pits in the AA7075 and NZ. More pronounced pits occurred in the AA7075. Mechanical stress, rather than the environment, caused the failure. An SEM analysis of the specimen immersed in the 3.5% NaCl solution shows a fibrous fracture surface with dimples. For the strain rate of $10^{-7}s^{-1}$, the fracture was on the AA7075 side and took place in the TMAZ/HAZ. The specimens tested at this speed failed at a much lower stress level and did not show any plastic deformation. The attack started as pits and resulted in a significant degree of deterioration. The pits not only shortened the fatigue life of the AA7075 by a factor of three but also decreased the fatigue crack initiation threshold by about 50% [46, 47].

2.4 Potentiodynamic Polarization

Potentiodynamic polarization is used to provide important and useful information relating to the corrosion mechanisms, corrosion rate, and susceptibility of specific materials to corrosion by electrochemical reactions. Polarization methods change the working electrode potential and monitor the current. In an anodic polarization process, the working electrode is made more electropositive and electrons are withdrawn from it. In a cathodic polarization process, the working electrode is made more electronegative and electrons are injected into it. In a galvanic couple, the material with a lower electrochemical potential is more active and acts as the anode.

Zucchi et al. [48] presented polarization curves on BM and NZ electrode of FSW AA5083 in 3.5% NaCl + 0.3 g/l H_2O_2 solutions. The corrosion potential of the NZ was more positive than that of the BM. Jariyaboon et al. [49] conducted the polarization

measurements of dissimilar FSW joining Al alloys AA2024 and AA7010. For anodic polarization measurements, the highest anodic reactivity (pitting potential, E_{pit}) was the NZ of AA7010, with values of about 0.1 V below the other regions of the weld. The TMAZ of AA 7010 was slightly more reactive than that of the BM. On the AA2024 side of weld, E_{pit} of the NZ was slightly more reactive than the TMAZ. For cathodic polarization measurements, the cathodic current density of AA7010 shows little variation and was relatively low and similar to that of the AA2024 BM. In contrast, the cathodic current density of the AA2024 TMAZ was significantly greater than that of the AA2024 BM. The AA2024 NZ shows a cathodic current density that was three times that of the AA2024 BM. Overaging of AA2024 can result in an increase in cathodic current density due to enhanced precipitation of cathodically active S phase particles [4].

Paglia et al. [50] investigated the corrosion of a FSW AA7075 with different tempers and microzones. Compared to the corrosion potential (E_{corr}: -0.964 V/SCE) and pitting potential (E_{pit}: -0.812 V/SCE) of AA7075-O temper, the BM of the AA7075-T7451 temper generally exhibited a slightly higher E_{corr} (-0.911 V/SCE) and E_{pit} (-0.761 V/SCE). The NZ and HAZ of the AA7075-O temper exhibited similar values with the BM, while the NZ and HAZ of AA7075-T7451 temper indicate a general trend to a slightly lower E_{corr} and E_{pit}. Compared with the BM, both AA7075 with O and T7451 temper in the longitudinal orientation generally exhibited lower E_{corr} and E_{pit} values for the NZ and HAZ. In contrast to the transverse orientation, the AA7075 with T7451 temper exhibited slightly higher values than did the O temper. In the HAZ, AA7075-O exhibited slightly higher E_{corr} and E_{pit} values than did the 7075-T7451.

Zeng et al. [51] reported polarization curves of FSW magnesium alloy AM50. The Ecorr of the welded joint and the BM were -1520 mV/SCE and -1553 mV/SCE, respectively. The Icorr value of the welded joint was lower than that of the BM because the finer grain structure evolves in this region [52]. They also reported polarization measured by the mini cell (a working electrode contacting with a plastic tip having a diameter of 0.5 mm and filled with 3.5% NaCl solution; inside, a saturated calomel electrode (SCE) and a platinum plate were used as reference electrode and auxiliary electrode, respectively.). The E_{corr} in the HAZ was the lowest in the joint, and E_{corr} in the BM was the highest. The E_{pit} of the HAZ was the highest. By measuring the I_{corr}, they learned that the corrosion rate of the TMAZ was the highest, followed by those of the HAZ and the NZ. Srinivasan et al. [32] studied corrosion behavior of the FSW AA2219. The E_{corr} values of the BM, TMAZ/HAZ and NZ were -605 mV, -575 mV, and -525 mV vs. Ag/AgCl, respectively. The I_{corr} values of the BM, TMAZ/HAZ and NZ were 2.0 μAcm^{-2}, 1.7 μAcm^{-2}, and 1.2 μAcm^{-2}, respectively. The TMAZ/HAZ and NZ exhibited better corrosion resistance than did the BM, which was reported in the 2xxx series aluminum alloys [53]. The dissolution of precipitates in the NZ and the coarsening of precipitates in the TMAZ/HAZ might be the reasons for the improved corrosion resistance and the nobler corrosion potentials of these two regions.

2.5 Aqueous Corrosion

The aqueous corrosion of metals reveals that a complex process involving chemical, electrochemical, and physical changes to the metal has taken place [54-56]. Corrosion of metal often results in significant material degradation and failure due to the metal's interaction with the surrounding electrochemical media. Interaction of metal, the

electrolyte, dissolved oxygen or halide ions is usually involved in the underlying physical and chemical processes that trigger the coupled electrochemical dissolution of metal and reduction of agents in the environment [57].

Wadeson et al. [15] studied the corrosion behavior of FSWAA7108-T79. The most severe attack occurred at the edges of the TMAZ immersed for 72 hours in a modified solution (15 vol. % dilution of a solution of 4.0 M NaCl, 0.5 M KNO_3, and 0.1 M HNO_3). Some of the ridges at the surface of the TMAZ were completely removed; the corrosion extended through the TMAZ into the HAZ. The remaining ridges were also severely corroded, suggesting that the ridges are highly susceptible to corrosion, partly because of the highly deformed microstructure caused by the thermomechanical processing.

Paglia et al. [50] studied corrosion behavior of an FSW AA7075. The corrosion immersion tests were carried out in a $NaCl/H_2O_2$ solution at 30 °C according to the ASTM G110-92 standard [58]. Corrosion products were observed on both the AA7075-T7451 and the AA7075-O, the latter having less. On the other hand, the AA7075-O-FSW-T7451 (T7451 temper was applied to the 7075-O weld) only occasionally exhibited corrosion products. An investigation of the localized corrosion of the HAZ showed microstructural pits in the AA7075-O temper and an increase attack of the AA7075-T7451 temper. A similar increase in the extent of intergranular corrosion of the AA7075-T7451 was observed in the NZ, especially along the onion rings bands. The AA7075-O-FSW-T7451 temper exhibited a less sharp intergranular attack than did the AA7075-O and AA7075-T7451.

Jariyaboon et al. [4] conducted immersion experiments (0.1 M NaCl for 24 h) to study the corrosion behavior of FSW AA2024-T351. For low rotation speeds of FSW samples,

the corrosion was localized in the NZ and intergranular attack was found in the nugget. For the higher rotation speeds, the corrosion attack predominately occurred in the HAZ. A predominately intergranular attack was found in the HAZ, although isolated areas of attack were observed in the NZ, where there was also evidence of grooves around constituent intermetallic particles. In addition, some intergranular attack was found at the bottom of the NZ. For low and high rotation speeds, the BM alloy showed grooves around intermetallic particles. The grooves around the constituent particles occurred because of the cathodic reduction of oxygen, which occurs at the constituent particles and causes an increase in alkalinity in the solution around the particles, a process that leads to the dissolution of the Al matrix.

The corrosion properties of a diode laser melted FSW of AA2024-T351 was studied by Kalita [59]. An immersion test was performed at room temperature in a quiescent condition in a 300 ml 0.5M NaCl solution. No pitting occurred in the laser-melted region; however, in the un-melted region there was severe pitting. The size of pits formed in the un-melted native weld was about 700 μm in diameter. There was a complete melt track with no visible pitting inside and a small pit about 40 μm in diameter in thick planar boundary zone. Only one significant pit was observed in the thick planar boundary zone of a melt tract in the sample with some melt tracks and overlap regions. Overlapping regions did not show preferential pitting corrosion. Laser melting enhanced the pitting resistance of FSW AA2024-T351. Pitting did not initiate at the overlapping regions of the laser treated specimen. These results show that an untreated native weld is more prone to pitting corrosion by formation of much larger pits.

Jariyaboon et al. [49] examined corrosion of dissimilar FSW joints of AA2024 and AA7010. The immersion test was performed in a 0.1 M NaCl solution for 15 hours. Localized corrosion attack, particularly at the bottom of the weld, occurred in the NZ of AA7010. In the NZ, intergranular attack was observed in the AA2024 region. Cathodically active particles produce local alkalinity as a result of oxygen reduction which causes grooves to form the matrix next to these particles [60-62]. Grooves were also observed around the particles in the BM of AA7010 as well as in the BM of AA2024. The NZ was more anodically reactive than was the BM in an immersion test of AA2024. Overaging of AA2024 can lead to an increase in cathodic reactivity because of enhanced precipitation of cathodically active S phase particles [4]. The increase alkalinity in this region of the weld suppressed the intergranular attack. Corrosion was particularly severe in the NZ of FSW AA2024 and AA7010 because there was a strong couple between the most anodically active region of the structure (NZ of AA7010) and the most cathodically active region (NZ of AA2024).

2.6 Principal Conclusions

FSW is a solid state joining technique. FSW aluminum alloys are composed of four distinct microstructure zones: NZ, TMAZ, HAZ and BM. Two theories explain the hardness of the NZ: the Hall-Petch relationship (grain-boundary strengthening) and the Orowan mechanism (dislocation bowing). The Hall-Petch relationship is used to explain the phenomenon that the hardness of HAZ is much higher than that of the BM, while Orowan mechanism plays a more dominant role in lower hardness of the NZ. The NZ has higher density dislocation and finer dispersed precipitates, which is not only because of the intense plastic deformation and frictional heating, but also because of dynamic

recrystallization. The variation in microstructures is complex and can produce differing polarization trends in various alloys and temper conditions. For example, the NZ, HAZ, and BM of the AA7075-O temper exhibited similar corrosion resistance, while the TMAZ/HAZ and NZ of AA2219-T87 exhibited better corrosion resistance than did the BM. In aqueous corrosion, the corrosion and intergranular attacks were generally localized in the NZ/HAZ/TMAZ. There remains a limited understanding of the relationship between microstructure and corrosion behavior of FSW aluminum alloys, especially in FSW AA5086-AA5086, AA5086-AA6061, and AA6061-AA6061 aluminum alloys. There has not been any systematic study reporting the relationship between microstructure, mechanical properties, and corrosion behaviors of FSW AA5086-AA5086, AA5086-AA6061, and AA6061-AA6061. The aim of this work is to investigate how corrosion behavior can be related to microstructure and mechanical properties.

Chapter 3

Materials and Methods

3.1 Materials

The base materials used in this study were AA5086-H32 and AA6061-T6511 plate (300 mm × 50 mm × 6 mm). These materials were supplied by McMaster-Carr. The chemical composition of the AA5086 and AA6061 is listed in Table 3.1.

Table 3.1 Chemical composition of AA5086 and AA6061

	Cu	Mn	Mg	Zn	Cr	Ti	Si	Fe	Al
6061 (%)	0.05~0.4	≤0.15	0.8~1.2	≤0.25	0.4~0.8	≤0.15	0.4~0.8	≤0.7	Balance
5086 (%)	≤0.10	0.2~0.7	3.5~4.5	0.25	0.05~0.25	0.15	≤0.4	≤0.5	Balance

3.2 Processing of Friction Stir Weld

Figure 3.1 Vectrax CL Series Milling machine used in the current FSW research

The friction stir welding was performed on a Vectrax CL Series Milling Machine (Figure 3.1). A welding tool with a shoulder of 25 mm and a pin of 8 mm wide and 6.35mm long was used. The tool rotation speed was preset at 1000 RPM. The travel feed rate was preset at 20 mm/min, 15 mm/min, and 12 mm/min with the tool titled at 3° towards the fed material. The pin was manually driven into the panels for some *z* distance and was maintained throughout the process. The Al alloy pieces AA5086-AA5086, AA5086-AA6061, and AA6061-AA6061 after FSW are shown in Figure 3.2.

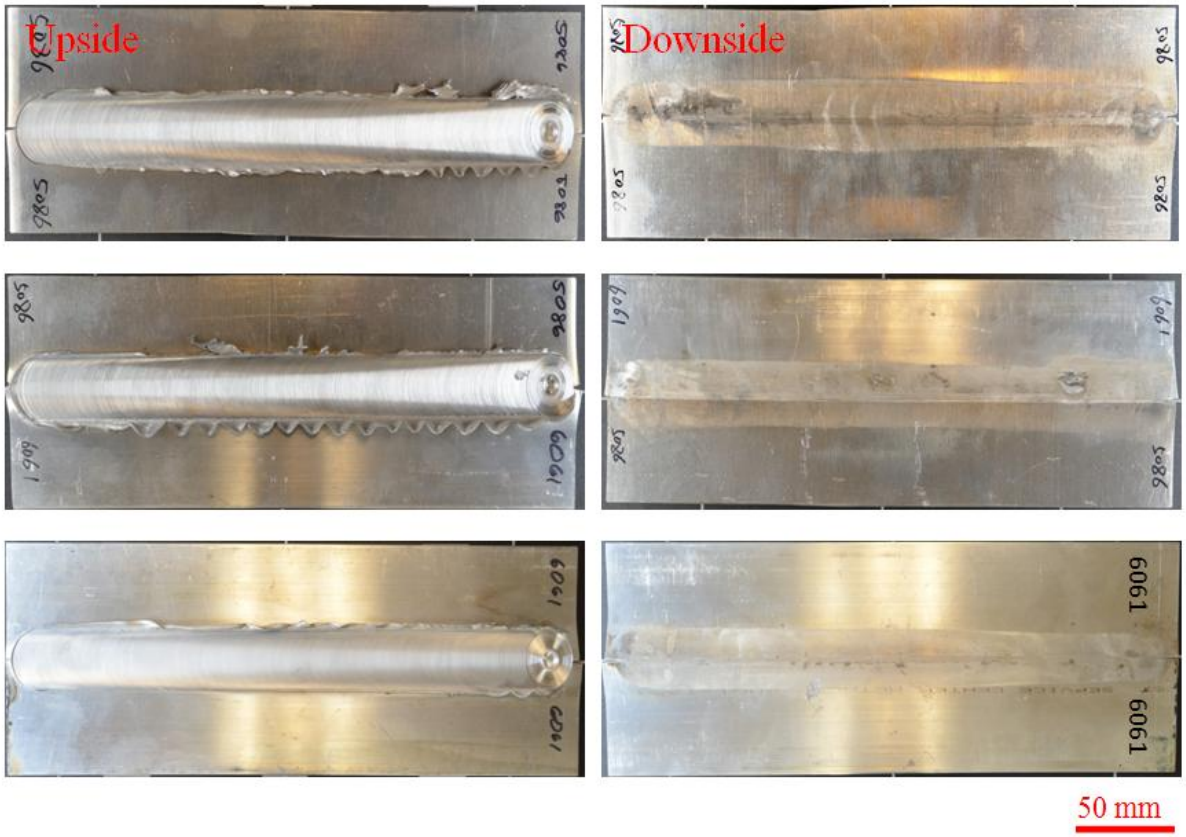

Figure 3.2 Upside and downside of FSW AA5086-AA5086, AA5086-AA6061, and AA6061-AA6061

3.3 Electrochemical Experiments

3.3.1 Electrolytes

Electrolytes used in polarization and immersion experiments were 3.15 wt% NaCl, 0.5 M Na_2SO_4, and ASTM seawater. The 18.1 MΩ-cm water was dispensed using the Barnstead/Thermolyne Nanopure® Diamond™ Life Science Ultrapure water system. The 3.15 wt% NaCl and 0.5 M Na_2SO_4 solutions were prepared from reagent-grade chemicals and 18.1 MΩ-cm water. The ASTM seawater was prepared using ASTM D-1141-52 sea salt. Table 3.2 shows the standard composition of the ASTM sea salts in weight percent [63].

Table 3.2 Composition of ASTM seawater

Salts	Wt%
NaCl	58.490
$MgCl_2 \cdot 6H_2O$	26.460
Na_2SO_4	9.750
$CaCl_2$	2.765
KCl	1.645
NaHCO3	0.477
KBr	0.238
H_3BO_3	0.071
$SrCl_2 \cdot 6H_2O$	0.095
NaF	0.007

3.3.2 Electrode Fabrication

The critical regions of FSW AA5086-AA5086, AA5086-AA6061, and AA6061-AA6061 Al alloys electrodes were fabricated in the laboratory. The FSW AA5086-AA5086,

AA5086-AA6061, and AA6061-AA6061 Al alloys plates were machined to the following dimensions: 100 mm × 25 mm × 5mm. Then they were cut into 5 mm × 5 mm squares using an Isomet™ low speed saw with a Buehler diamond wafer blade (series 15 LC diamond). The four corners of each Al alloy square were rounded off to reduce stress concentration, and one of the faces was ground using Buehler-Met II Silicon Carbide 320-grit grinding paper. The Al alloy squares were first cleaned in acetone and then cleaned ultrasonically in 18.1 MΩ-cm water for 20 minutes. A 200 mm cooper wire was attached to the ground face of each Al alloy square with Silver Paint II and cured in the oven at 70°C for 20 minutes. A glass tube 160 mm in length was made by scribing and breaking it from a longer section. To dull the edges, the ends of the glass tube were heated to a molten state with a gas torch and then allowed to cool. The glass tube was slid over the copper wire. A clear LOCTITE 0151 Hysol Epoxi-Patch Adhesive was used to attach the Al alloy and copper to the end of glass tube. The glass tube end was sealed with epoxy and no copper was exposed. The adhesive was applied in such a way that the Al alloy bonded to the glass tube and left a surface area (critical regions) of 5 mm × 5mm exposed. It was cured at 70°C for 120 minutes.

The electrodes were ground using a Buehler Ecomet® 6 variable speed grinder-polisher. The surface area that was exposed was ground flat with 180-grit SiC paper, followed by 320-grit and 600-grit SiC papers. The electrodes were then examined under an optical microscope to detect and avoid any crevices around the edges of the exposed area and the epoxy surface. Electrodes were then polished to a mirror-like finish using Buehler microcloth and slurries of 1 μm alpha alumina, 0.3 μm alpha alumina, and 0.05 μm

gamma alumina powder. Figure 3.3 shows a typical ground and polished FSW AA6061-AA6061 electrode. After the electrode was polished, it was rinsed with purified water.

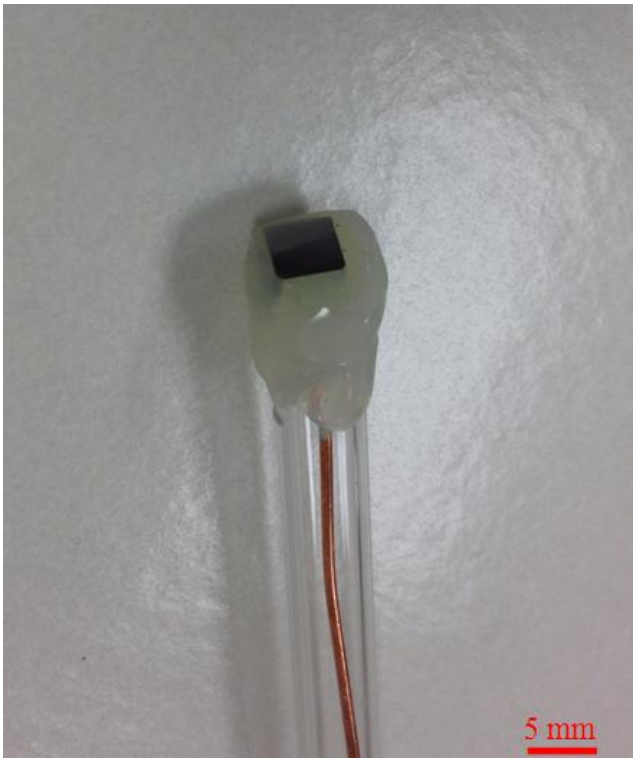

Figure 3.3 A typical ground and polished FSW AA6061-AA6061 electrode

3.4 Coupons Characterization

3.4.1 X-Ray Diffraction

X-ray diffraction (XRD) spectra were obtained directly from three regions— the upside, downside, and BM—of the friction stir welded surfaces after immersion in the test solutions. A Rigaku MiniFlex^{TM} II benchtop XRD system equipped with a Cu (Kα) radiation was used for XRD measurements. The scans were done in the range of 3–90° (2θ). A scan speed of 1° (2θ)/min was used.

3.4.2 Scanning Electron Microscope (SEM)

A Hitachi S-3400N SEM equipped with an Oxford Instruments energy dispersive X-Ray analyzer system was used to characterize five regions (NZ, TMAZ, HAZ, BM, and downside) of immersion FSW Al alloy coupons.

3.4.3 Raman Spectroscopy

Raman analysis was conducted on the friction stir welding Al alloy coupons after immersion using a Nicolet Almega XR dispersive Raman Spectrometer (Thermo Scientific Corp.). The Raman spectra were collected at five regions for each coupon. An objective with magnification of 50X and estimated spatial resolution of 1.6 μm was used. A green Nd: YAG laser source with 532 nm wavelength excitation was used to operate the instrument. The laser power was maintained at approximately 8 mW. The maximum spectra resolution was up to 2.2–2.6 cm^{-1} using a 25 μm pinhole or slit, which requires longer acquisition time and produces more noise. To reduce the collecting time, an aperture of 100 μm pinhole was used, giving a resolution in the range of 8.4–10.2 cm^{-1}. The accumulation time was 120 seconds.

3.5 Weight Loss Technique

In the immersion experiments, the specimens were completely immersed in the solutions, resulting in galvanic action between the various welded zones. To obtain the total mass loss, the FSW Al alloy coupons were cleaned with a solution of phosphoric acid (H_3PO_4) and chromium trioxide (CrO_3) at 90 °C for 5–10 min to remove the corrosion products. The solution of phosphoric acid and chromium trioxide wash procedure was described in ASTM G01-03 [64]. After being washed, the FSW Al alloy coupons were weighted and compared to their respective initial mass values to obtain the total mass loss.

The corrosion rate was calculated for each FSW Al alloy coupon based on the total loss. The following equation was used to calculate the corrosion rate for FSW Al alloy coupon samples:

$$Corrosion\ Rate = \frac{\Delta m}{A \cdot t}$$

where Δm is the change in mass in grams, A is the area of the sample in m^2, and t is the time in days.

Chapter 4

Microstructure and Mechanical Properties

4.1 Introduction

The microstructure of six distinct zones (NZ, TMAZ, HAZ, BM, downside, and cross-section) of FSW AA5086-AA5086, AA5086-AA6061, and AA6061-AA6061 were investigated using etching technology and an optical microscope. The hardness of FSW AA5086-AA5086, AA5086-AA6061, and AA6061-AA6061 was measured by Wilson Rockwell Vickers Micro-hardness Tester to study how these six distinct regions affect mechanical properties. Tensile tests were conducted to study tensile and yield strength of FSW AA5086-AA5086, AA5086-AA6061, and AA6061-AA6061. The results indicate that fracture occurred in the relatively weaker TMAZ/HAZ.

4.2 Microstructure

Generally, FSW aluminum alloys are composed of four distinct microstructural zones: NZ, TMAZ, HAZ, and BM. In this study, we selected six critical regions (NZ, TMAZ, HAZ, cross-section, downside of the NZ, and BM) to characterize the microstructure of FSW AA5086-AA5086, AA5086-AA6061, and AA6061-AA6061. The downside microstructure corresponds to the downside NZ, and the cross-section cuts through the NZ

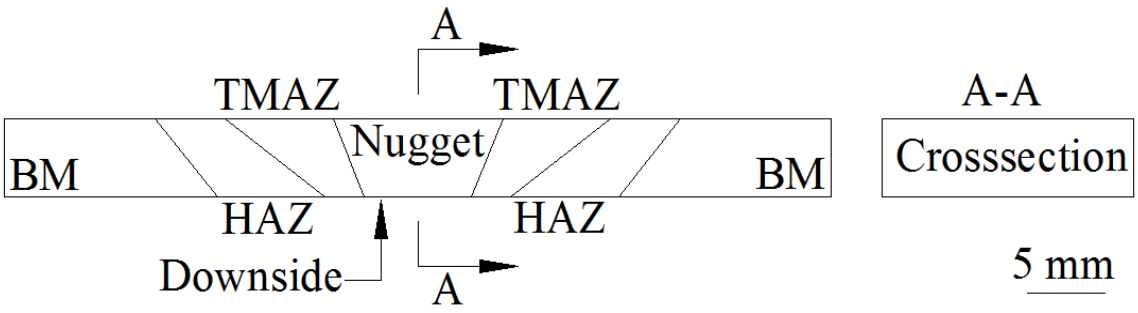

Figure 4.1 Six critical regions of FSW aluminum alloys

Etching was accomplished using Keller's reagent, which is the standard for etching aluminum and aluminum alloys. It was prepared by mixing 345 mL of deionized water, 125 mL of 10% HNO_3 (nitric acid), 20 mL of 37% HCl (hydrochloric acid), and 10 mL of 49% HF (hydrofluoric acid). This is produced 500 mL of solution that was 2.5% HNO_3, 1.5% HCl, and 1% HF. The samples were etched for increments of approximately 20 seconds to ensure that the samples were not over-etched. This iterative procedure involved immersion in the solution, rinsing and drying, viewing under optical microscope, and repeating. This procedure was repeated until grain structure was evident.

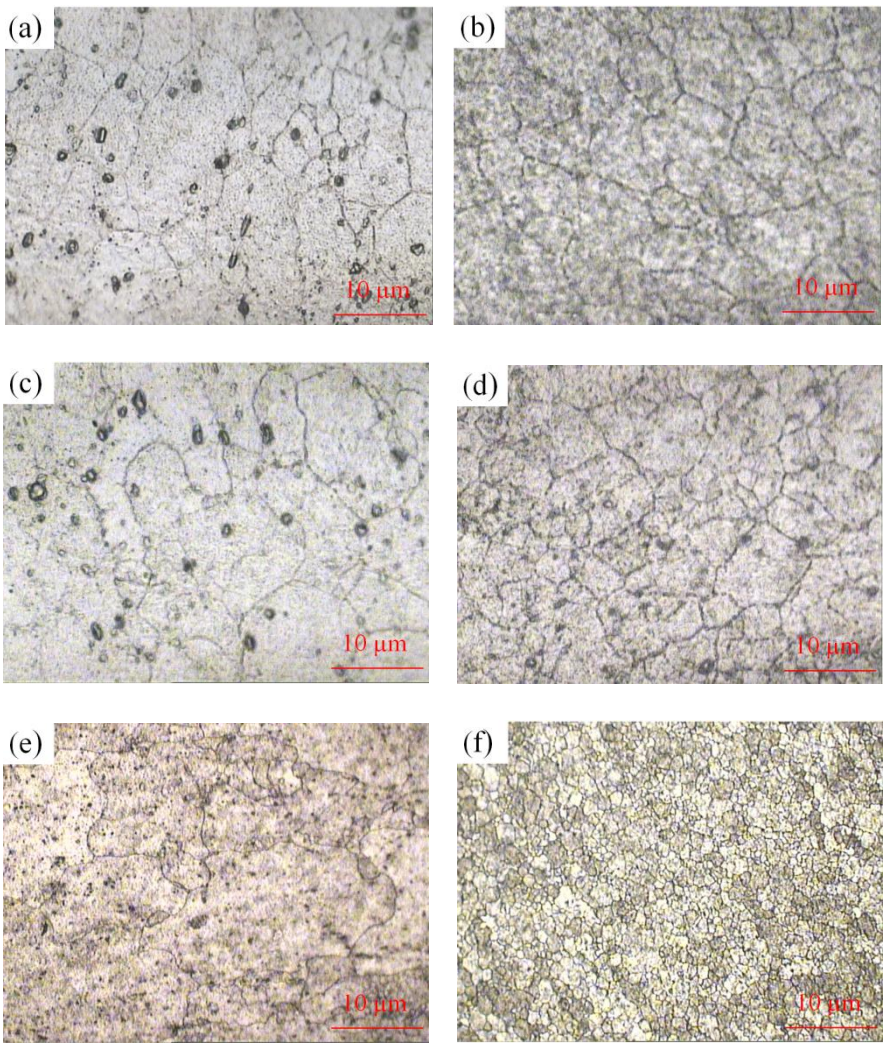

Figure 4.2 Typical microstructures at different regions of FSW AA6061-AA6061 after etching with Keller's reagent: (a) cross-section, (b) downside, (c) HAZ (, (d) TMAZ, (e) BM, and (f) NZ

Figure 4.2 is an example of the grain structure at different regions of FSW 6061-6061. The NZ consists of fine equiaxed grains due to dynamic recrystallization [18, 20]. The grains within NZ are much smaller than those in other regions. For the average grain size, the order of the largest to the smallest for FSW zones in AA6061-AA6061 is as follows: BM > HAZ > cross-section > downside > TMAZ > NZ. TMAZ was adjacent to the NZ. In the TMAZ, the strain and the temperature were lower than in the NZ and the effect of

welding on the microstructure was correspondingly smaller. Unlike NZ, the microstructure was recognizably that of the parent material, although significantly deformed and rotated. The grain size of the downside (underside of the NZ) was similar to that of the TMAZ. The grain size of the HAZ was similar to that of the BM. The HAZ was common to all welding processes subjected to a thermal cycle, but it was not deformed during welding.

4.3 Hardness

The plates of FSW AA5086-AA5086, AA5086-AA6061, and AA6061-AA6061 were machined and ground to the following dimensions: 100 mm × 25 mm × 5 mm. The Wilson Rockwell Vickers micro-hardness Tester was used to characterize the hardness. The experiments were carried out vertical to the weld with a distance between neighboring measured points of 2 mm. A load of 60 g was applied for 3 s, with a dwell of 10 s. The hardness values of FSW AA5086-AA5086, AA5086-AA6061, and AA6061-AA6061 Al alloy were carried out using three samples cut from the same position from different FSW plates.

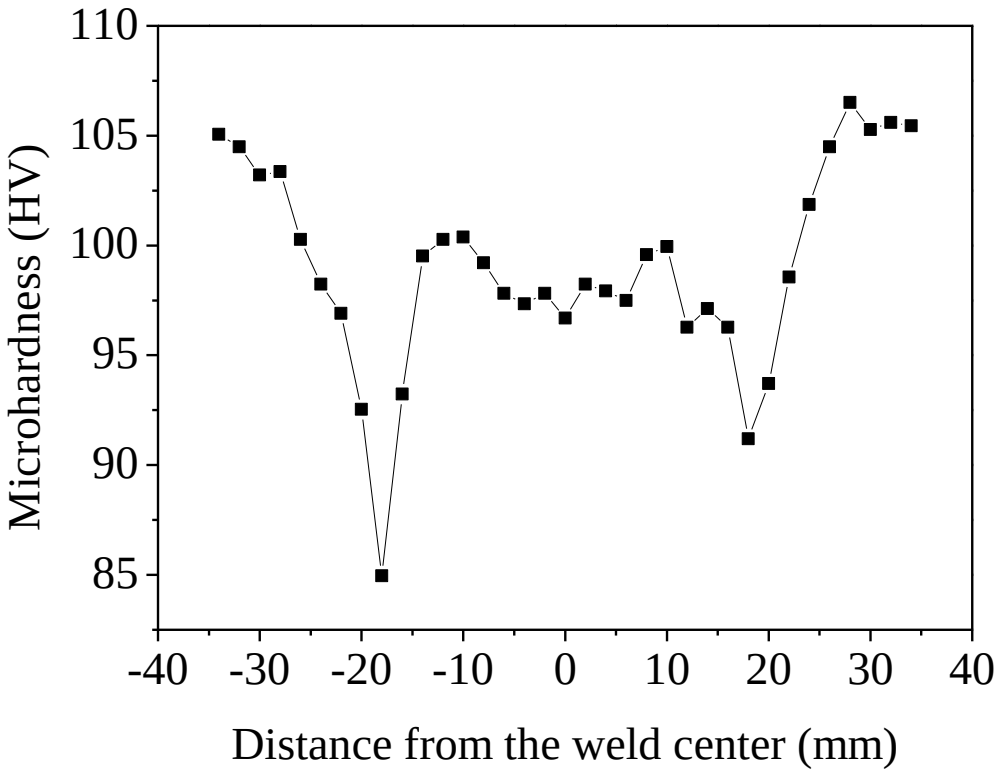

Figure 4.3 Microhardness distribution across the top surface of FSW AA6061-AA6061 measured with a 2 mm step

Figure 4.3 shows the typical microhardness distribution across the top surface of FSW AA6061-AA6061. The hardness curve is asymmetrical with respect to the weld centerline because the plastic flow field in the two sides of the weld center is not uniform [28, 65]. The larger distorted grains and distortion energy causes the strain-hardness to increase, resulting in the asymmetrical microhardness distribution. The minimum hardness of 85.0 HV was obtained in the HAZ region, suggesting that the tensile specimens are prone to fracture in this zone. The maximum value was present in the BM. The hardness of the TMAZ was higher than that of the NZ. However, according to the Hall-Petch relationship, the hardness value in the NZ should be higher than others zones because of its fine equiaxed grain structure. This may be because the thermal history of the FSW AA6061-AA6061 creates a softened region around the weld center. The

possible reasons for softening are that the thermal cycle of FSW causes strengthening precipitates to coarsen or dissolve. To analyze the hardness, the Orowan mechanism, which is based on the impediment of dislocation movement around small precipitates inside grains, may over shadow the Hall-Petch mechanism, which is based on grain size [30, 35].

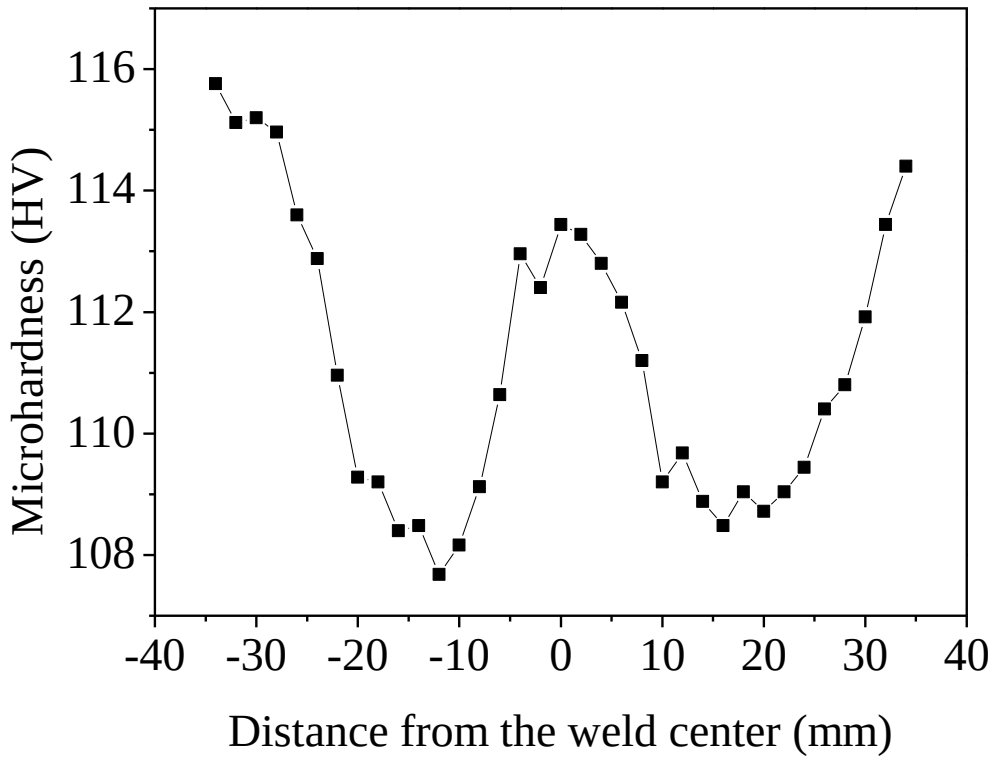

Figure 4.4 Microhardness distribution across the top surface of FSW AA5086-AA5086 measured with a 2 mm step

Figure 4.4 shows microhardness distribution across the top surface of FSW AA5086-AA5086. The hardness curve also demonstrates the "W" shaped hardness distribution characteristic, which is asymmetrical with respect to the weld centerline. The minimum hardness was obtained in the TMAZ/HAZ regions. The maximum value was in the BM. According to the Hall-Petch relationship, the hardness value in the NZ was higher than that of the TMAZ/HAZ due to its fine equiaxed grain structure. Also, since AA5086 is

strengthened by strain hardening and not by the presence of precipitates, it is possible that the thermal cycle of FSW causes the annihilation of dislocations and destroys the strain hardening mechanism.

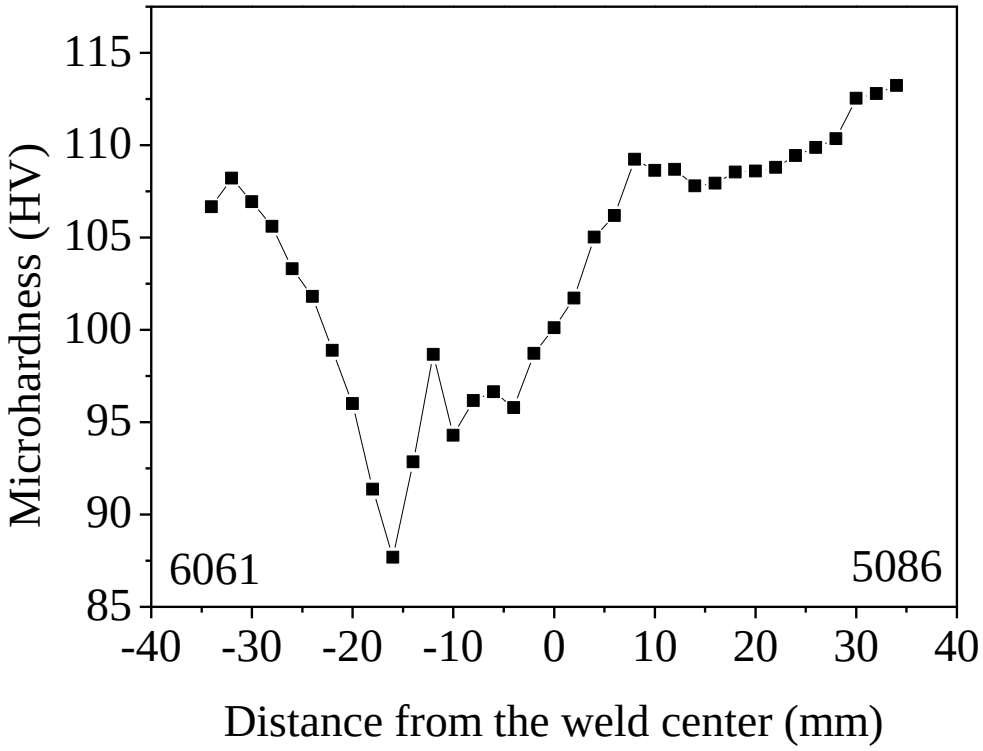

Figure 4.5 Microhardness distribution across the top surface of FSW AA5086-AA6061 measured with a 2 mm step

Figure 4.5 shows microhardness distribution across the top surface of FSW AA5086-AA6061 measured with a 2 mm step. The weld region does not demonstrate the "W" shaped hardness distribution characteristic. The minimum hardness of 88 HV is obtained in HAZ region of AA6061 side, which suggests that the tensile specimens are prone to fracture in this zone. The hardness distribution in AA6061 side of FSW AA5086-AA6061 was similar to that of the FSW AA6061-AA6061, but the hardness distribution in AA5086 side of FSW AA5086-AA6061 was not similar to that of the FSW AA5086-AA5086. For the AA5086 side, the hardness of BM was higher than that of the

TMAZ/HAZ. For the NZ, the hardness increased from the AA6061 side to the AA5086 side.

4.4 Tensile Experiments

The tensile tests were performed at a crosshead speed of 3 mm/min using an Instron-5500R testing machine. Tensile specimens were machined from the NZ in two directions from the weld: parallel (longitudinal) and normal (transverse). The configuration of the tensile specimens is shown in Figure 4.6. An axial extensometer with 25 mm gage length was attached to the test specimens at the gauge section. The strain analysis of each specimen was made by the ASAME automatic strain measuring system. The tensile properties of the joints were evaluated using three tensile specimens cut from the same joint.

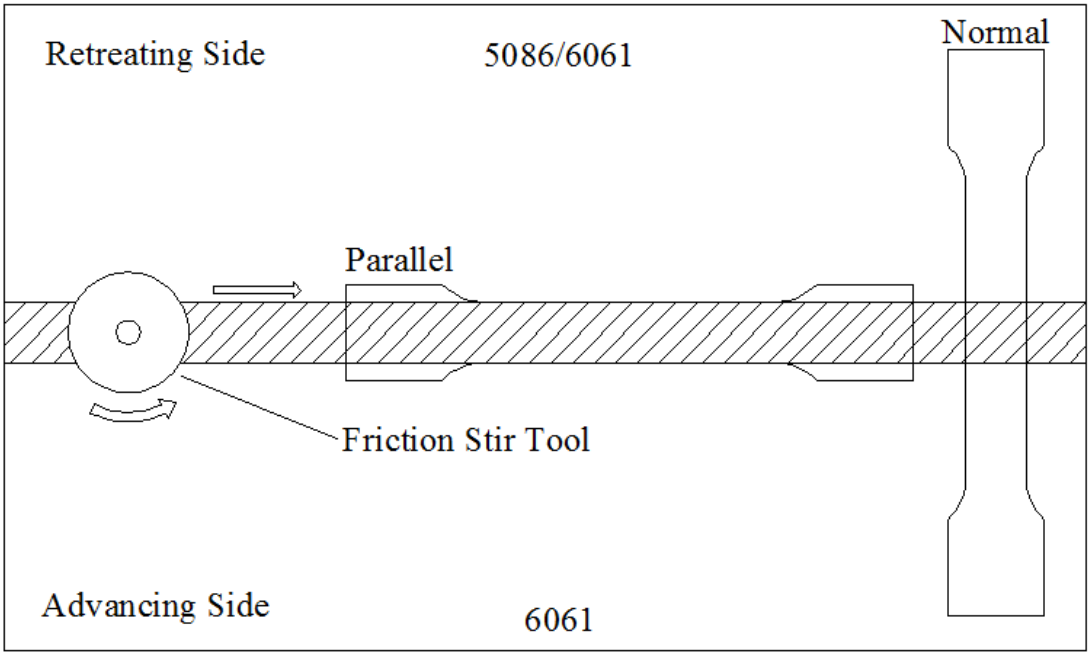

Figure 4.6 The configuration of FSW aluminum alloys for tensile test

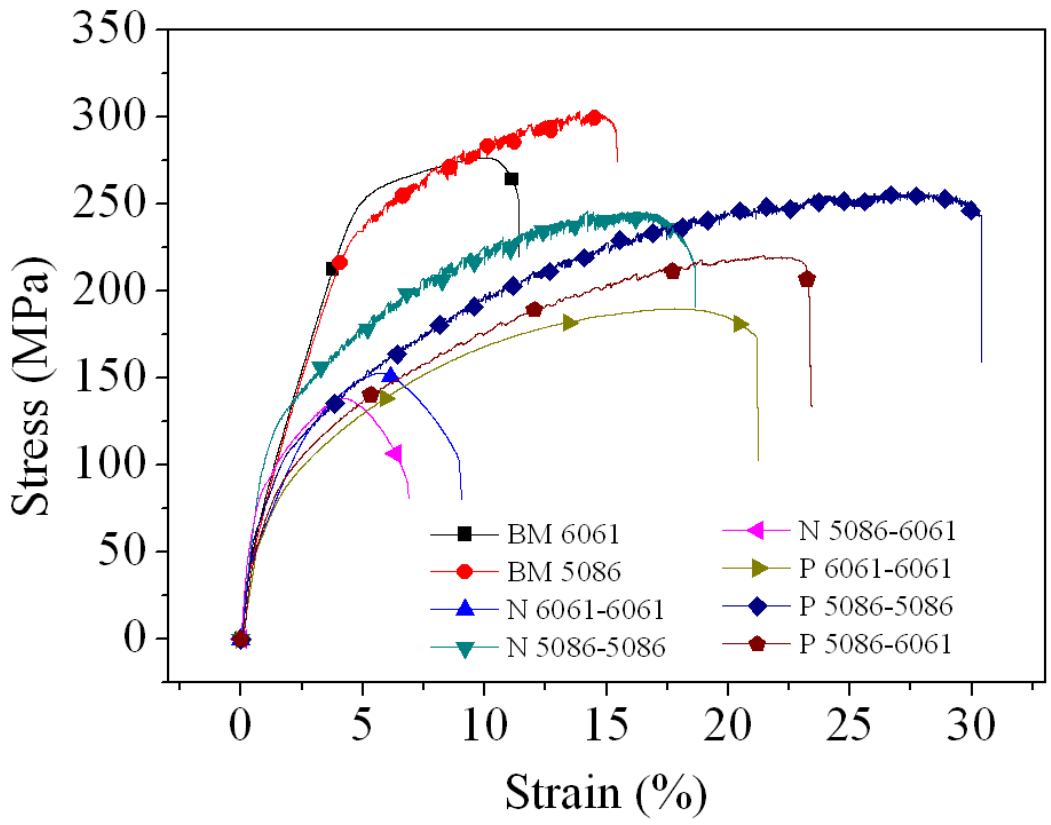

Figure 4.7 Tensile properties of the base materials and two directions (parallel and normal) FSW specimens

The tensile properties of FSW joints are shown in Figure 4.7. The elongation, yield strength, and tensile strength of the BM AA6061 and BM AA5086 were 12.1% and 16.7%, 242 MPa and 237 MPa, 276 MPa and 300 MPa, respectively. By comparison, all FSW tensile specimens showed a significant decrease in both tensile and yield strength. In direction parallel to the weld axis, the ductility for the longitudinal tensile specimens significantly increased compared to that of the BM. In the normal direction perpendicular to the weld axis, the ductility of the transverse specimens for FSW AA5086-AA5086 increased while those for FSW AA6061-AA6061 and AA5086-AA6061 decreased. As mentioned in Figure 4.6, the longitudinal tensile specimens contained only recrystallized grains from the NZ. From hardness results, we know that

the hardness values of the NZ were lower than that of the BM, possibly explaining why the longitudinal tensile specimens of FSW joints decreased in both tensile and yield strength. The transverse tensile specimens contained all four zones (i.e., BM, HAZ, TMAZ and NZ). The observed ductility was measured as average strain over the gage length, including the various zones that have different resistances to deformation due to differences in grain size and precipitate distribution. When a tensile load was applied to the joint, failure occurred in the weaker regions of the joint [38]. The fracture of the transverse direction tensile specimens occurred in the HAZ.

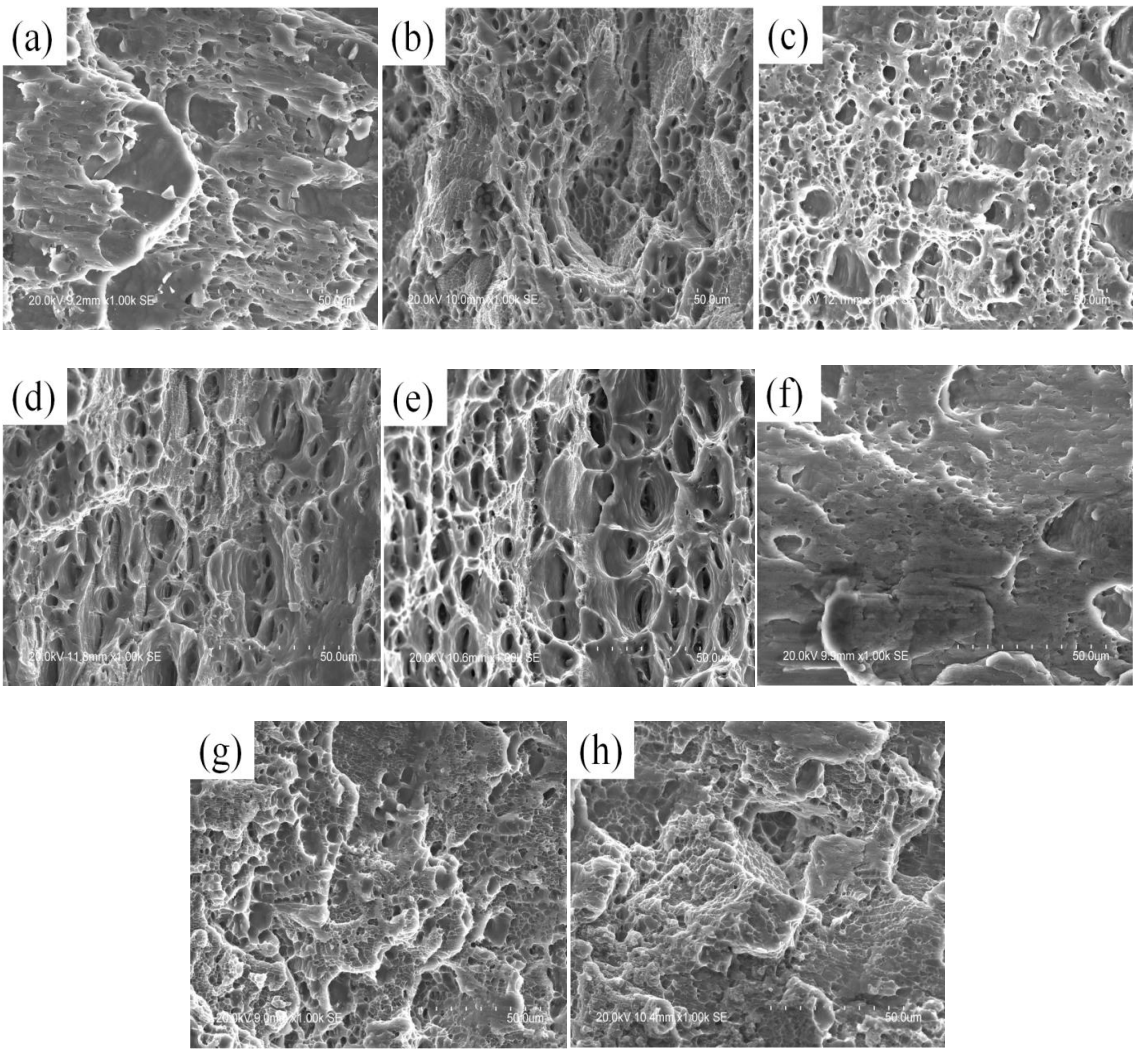

Figure 4.8 SEM fractographs of BM and two directions (Transverse and Longitudinal) FSW specimens: (a) BM AA5086, (b) BM AA6061, (c) T AA5086-AA5086 (Failure occurred in HAZ), (d) T AA5086-AA6061 (Failure occurred in HAZ in AA 6061 Side), (e) T AA6061-AA6061 (Failure occurred in HAZ), (f) L AA5086-AA5086 (Failure occurred in Weld Zone), (g) L AA5086-AA6061 (Failure occurred in Weld Zone), and L AA6061-AA6061 (Failure occurred in Weld Zone)

To understand the failure patterns, the fracture surfaces of tensile specimens were characterized using SEM. All of the tensile fractures presented a 45° angle shear fractures along the tensile axis with the exception of BM AA6061, T AA6061-AA6061(Failure occurred in HAZ), and T AA5086-AA6061 (Failure occurred in HAZ in AA 6061 side). Fractures in T AA5086-AA6061 appeared in the AA6061 side. All of the fracture surfaces of tensile specimen showed obvious necking/plastic deformation except the BM

AA5086 and BM AA6061. Figure 4.8 shows SEM fractographs of the BMs and two directions of FSW specimens. The fractographs reveal dimple fracture patterns with teared edges full of micropores. The dimples were of various sizes and shapes. Compared with BM AA5086, the dimples of BM AA6061 were deeper and teared edges were thinner. Therefore, the BM AA5086 exhibited much better mechanical properties than did the BM AA6061. Also, T AA5086-AA5086, T AA5086-AA6061, and T AA6061-AA6061 had much deeper dimples and thinner teared edges than did L AA5086-AA5086, L AA5086-AA6061, and L AA6061-AA6061, respectively. Thus, the longitudinal direction FSW specimens have much better mechanical properties than do the transverse direction specimens.

Chapter 5

Potentiodynamic Polarization

5.1 Introduction

This chapter discusses the polarization experiment results of FSW AA5086-AA5086, AA5086-AA6061, and AA6061-AA6061 in 3.15 wt% NaCl. Figure 5.1 shows a polarization diagram of different anodic and cathodic curves. The thermodynamic driving force and the kinetics are obtained by measuring the potential on the vertical axis and the current density on the horizontal axis, respectively. The intersection of anodic and cathodic reactions identifies the equilibrium potential$E^0_{H^+/H_2}$ for an H_2 reaction, and the intersection of tangent lines by Tafel extrapolation of anodic and cathodic reactions is the exchange current density$I^0_{H^+/H_2}$. For metal M, the rate of the anodic reaction and cathodic reaction is the same at the equilibrium potential. In an anodic reaction of M, active behavior results if a protective oxide film does not form on the metal surface, and passive behavior results if a protective passive oxide film forms on the metal surface. The passive film can break down at the potential E_{pit} by pitting that can be identified by a rapid increase in anodic current density.

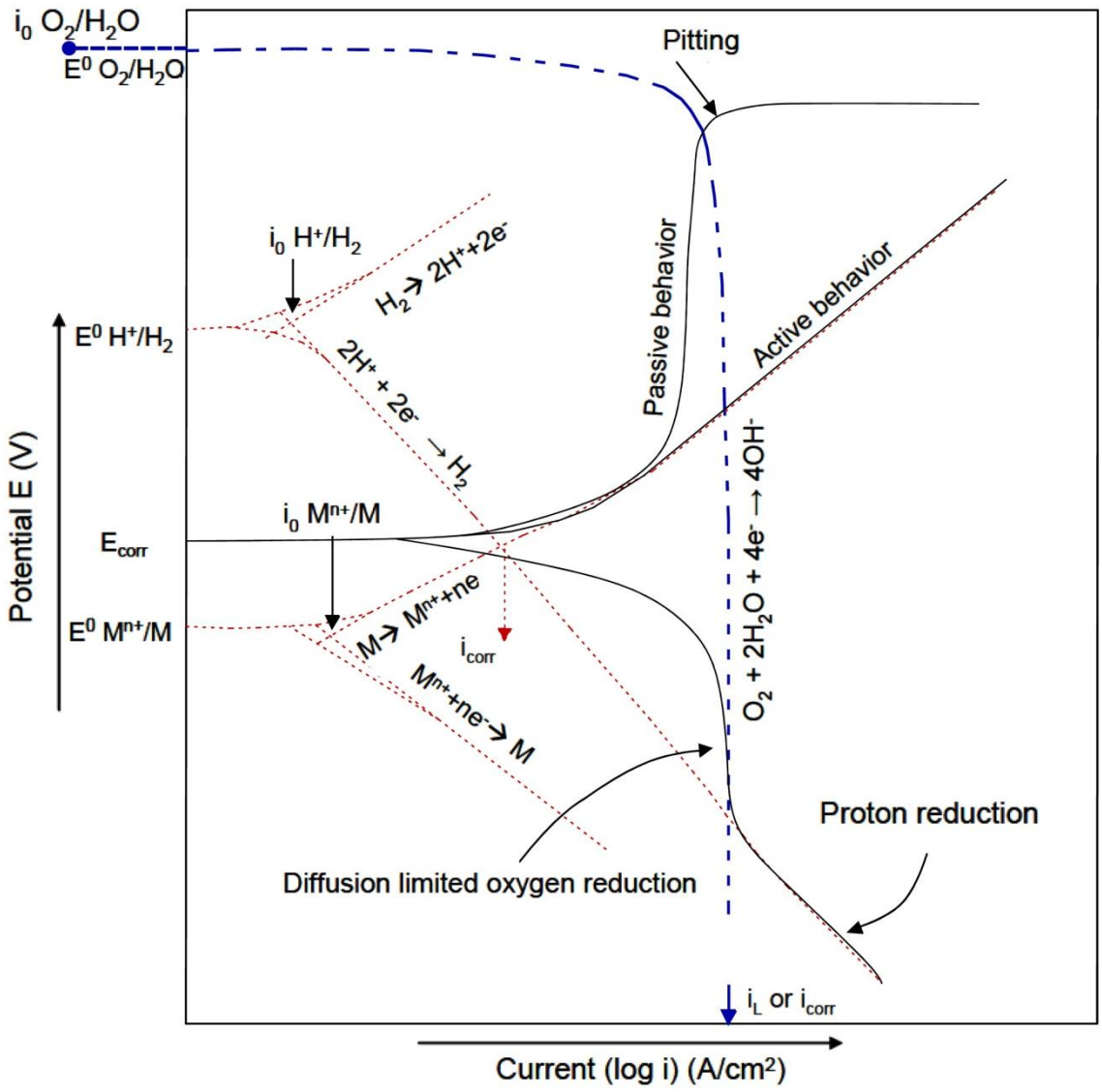

Figure 5.1 General description of potentiodynamic polarization diagram

5.2 Experimental

The anodic and cathodic polarization of critical regions of FSW AA5086-AA5086, AA5086-AA6061, and AA6061-AA6061 were conducted in deaerated 3.15 wt% NaCl. Cathodic polarization of critical zones of FSW AA5086-AA5086, AA5086-AA6061, and AA6061-AA6061 were conducted in aerated 3.15 wt% NaCl. Each anodic and cathodic polarization experiment was performed three times in deaerated and aerated conditions.

Deaerated electrolytes were sparged with compressed nitrogen and aerated electrolytes were sparged with compressed air. A platinum electrode was used as the counter electrode, and a saturated calomel electrode was used as the reference electrode. The specimens were stabilized at the corrosion potential for 60 minutes before scanning in either the anodic or cathodic direction at the rate of 1 mV/sec. During the experiments, the electrolytes were kept at a constant temperature of 30°C. The potential and current were recorded using Parstat 2273 Advanced Electrochemical potentiostat on a Windows operating system. Figure 5.2 shows a typical polarization experiments setup. In this chapter, the downside zone is the downside of the NZ.

Figure 5.2 A typical polarization experiments setup

5.3 Results and Discussion

5.3.1 Effect of deaerated solution

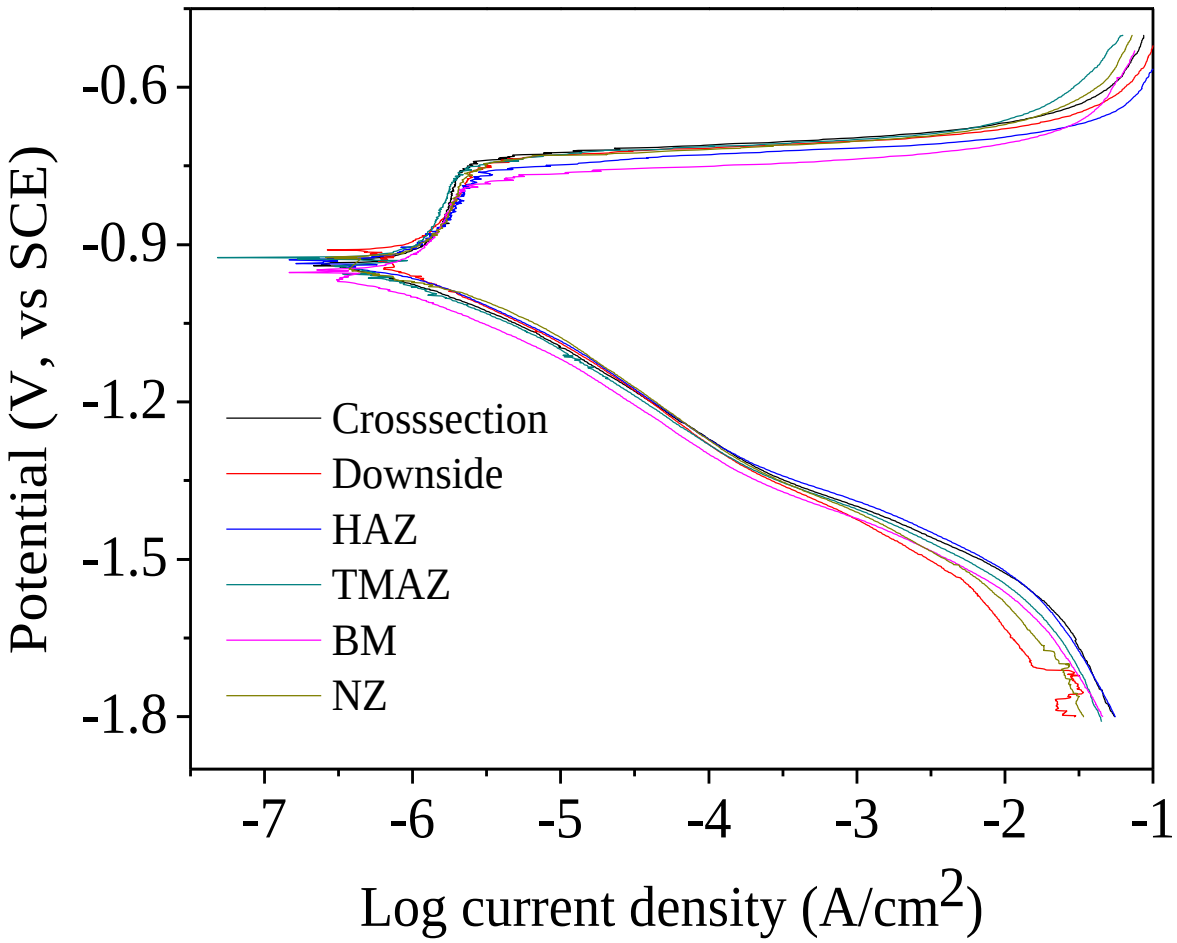

Figure 5.3 Polarization curves of different weld zones of FSW AA5086-AA5086 in deaerated 3.15 wt% NaCl solutions

Table 5.1 E_{corr}, I_{corr}, and E_{pit} values of the different weld zones of FSW AA5086-AA5086 in deaerated 3.15 wt% NaCl solutions and standard deviation (S.D.) of I_{corr}

Weld	E_{corr} (mV, vs SCE)	E_{pit} (mV, vs SCE)	I_{corr} (μA/cm^2)	*S.D. of* I_{corr}
Cross-section	-940	-741	1.08	0.40
Downside	-910	-737	0.80	0.35
HAZ	-929	-762	0.73	0.02
TMAZ	-924	-748	1.20	0.48
BM	-953	-767	1.70	0.07
NZ	-924	-730	1.15	0.02

Figure 5.3 shows typical polarization curves of different weld zones of FSW AA5086-AA5086 in deaerated 3.15 wt% NaCl solutions. The material of FSW AA5086-AA5086 shows a critical passive region below E_{pit}. The current density increased abruptly at potentials greater than E_{pit} due to the breakdown of the passive film. Table 5.1 shows E_{corr}, I_{corr} and E_{pit} values of the different weld zones of FSW AA5086-AA5086 in deaerated 3.15 wt% NaCl solutions. The potential E_{corr} of different weld zones shifted to more positive values from the BM (-953 mV_{SCE}). I_{corr} values of downside (0.80 μA/cm^2), NZ (1.15 μA/cm^2), cross-section (1.08 μA/cm^2), and the HAZ (0.73 μA/cm^2) decreased from those of the BM (1.70 μA/cm^2). It also can seen that susceptibility of the different weld zones to pitting decreased from the BM (E_{pit} = -767 mV_{SCE}). The increase in E_{pit} and decrease in I_{corr} values of downside of the NZ (E_{pit} = -737 mV_{SCE}, I_{corr} = -0.80 μA/cm^2), the HAZ (E_{pit} = -762 mV_{SCE}, I_{corr} = -0.73 μA/cm^2), TMAZ (E_{pit} = -748 mV_{SCE}, I_{corr} = -1.20 μA/cm^2), and NZ (E_{pit} = -730 mV_{SCE}, I_{corr} = -1.15 μA/cm^2) compared to the BM (E_{pit} = -767 mV_{SCE}, I_{corr} = -1.70 μA/cm^2) show that the corrosion resistance improved with the

use of FSW. The higher pitting potential did not necessarily correspond to a lower corrosion rate, while I_{corr} gave the direct measure of corrosion rate[66].

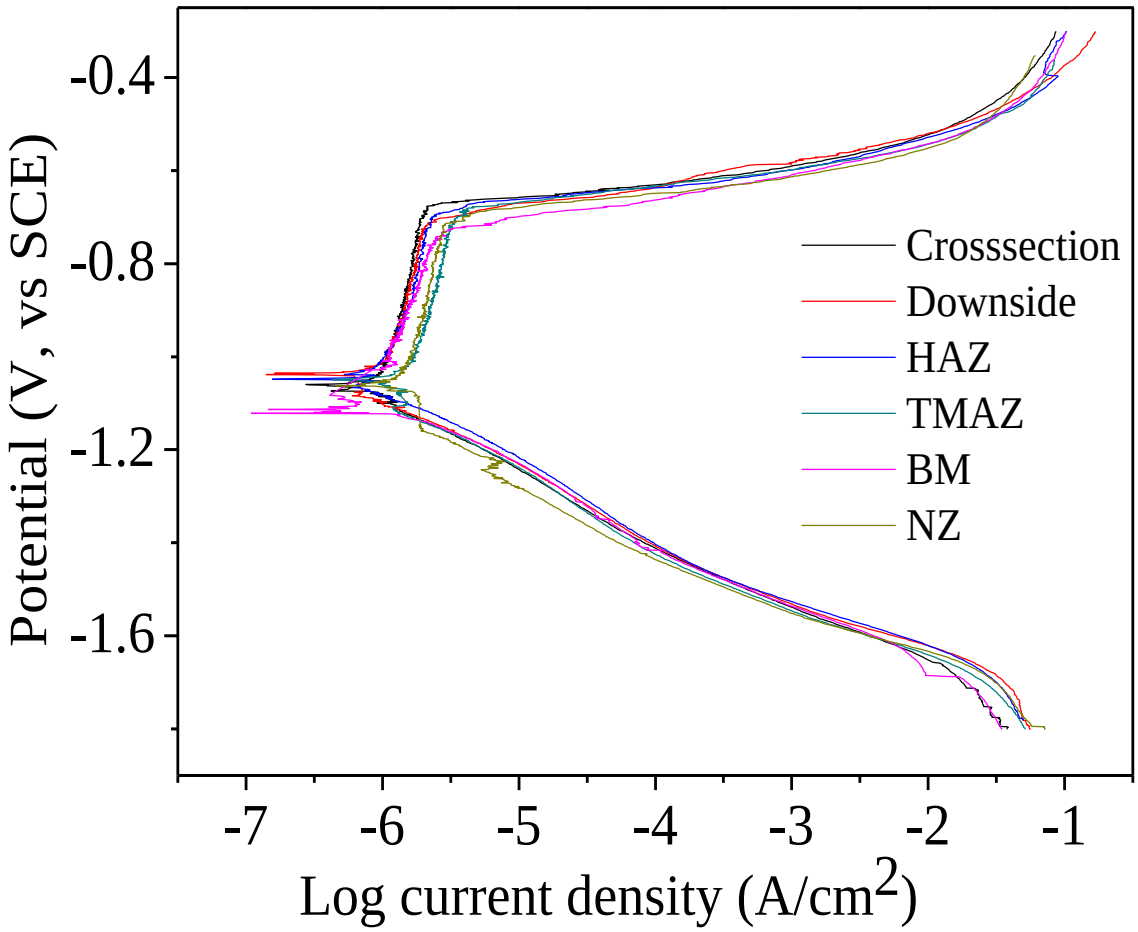

Figure 5.4 Polarization curves of different weld zones of FSW AA6061-AA6061 in deaerated 3.15 wt% NaCl solutions

Table 5.2 E_{corr}, I_{corr} and E_{pit} values of the different weld zones of FSW AA6061-AA6061 in deaerated 3.15 wt% NaCl solutions and standard deviation of I_{corr}

Weld	E_{corr} (mV, vs SCE)	E_{pit} (mV, vs SCE)	I_{corr} (μA/cm^2)	*S.D. of* I_{corr}
Cross-section	-1060	-678	0.93	0.32
Downside	-1039	-719	1.47	0.09
HAZ	-1048	-692	0.76	0.03
TMAZ	-1049	-685	1.54	0.27
BM	-1114	-724	2.44	0.71
NZ	-1063	-719	2.29	0.38

Figure 5.4 shows polarization curves of different weld zones of FSW AA6061-AA6061 in deaerated 3.15 wt% NaCl solutions. The FSW AA6061-AA6061 also showed passive region with current density, which was larger than that of FSW AA5086-AA5086. Compared to the BM, the potential E_{corr}, and E_{pit} shifted to more anodic potentials and the current I_{corr} values decreased, as shown in Table 5.2. The order of corrosion potential for FSW AA6061-AA6061 was as follows: downside (-1039 mV_{SCE}) > HAZ (-1048 mV_{SCE}) > TMAZ (-1049 mV_{SCE}) > cross-section (-1060 mV_{SCE}) > NZ (-1063 mV_{SCE}) > BM (-1114 mV_{SCE}). For the E_{pit}, the order was as follow: cross-section (-678 mV_{SCE}) > TMAZ (-685 mV_{SCE}) > HAZ (-692 mV_{SCE}) > downside and NZ (-719 mV_{SCE}) > BM (-724 mV_{SCE}). For I_{corr}, the values from highest to lowest were as follows: BM (2.44 μA/cm^2) > NZ (2.29 μA/cm^2) > TMAZ (1.54 μA/cm^2) > downside (1.47 μA/cm^2) > cross-section (0.93 μA/cm^2) > HAZ (0.76 μA/cm^2). The increase in E_{pit} and decrease in I_{corr} values of FSW AA6061-AA6061 also show that the corrosion resistance was improved by FSW. The dissolution of finer precipitates is in both the NZ and the downside. The coarsening of

precipitates in the TMAZ and HAZ could be the reason for the improved corrosion resistance [32].

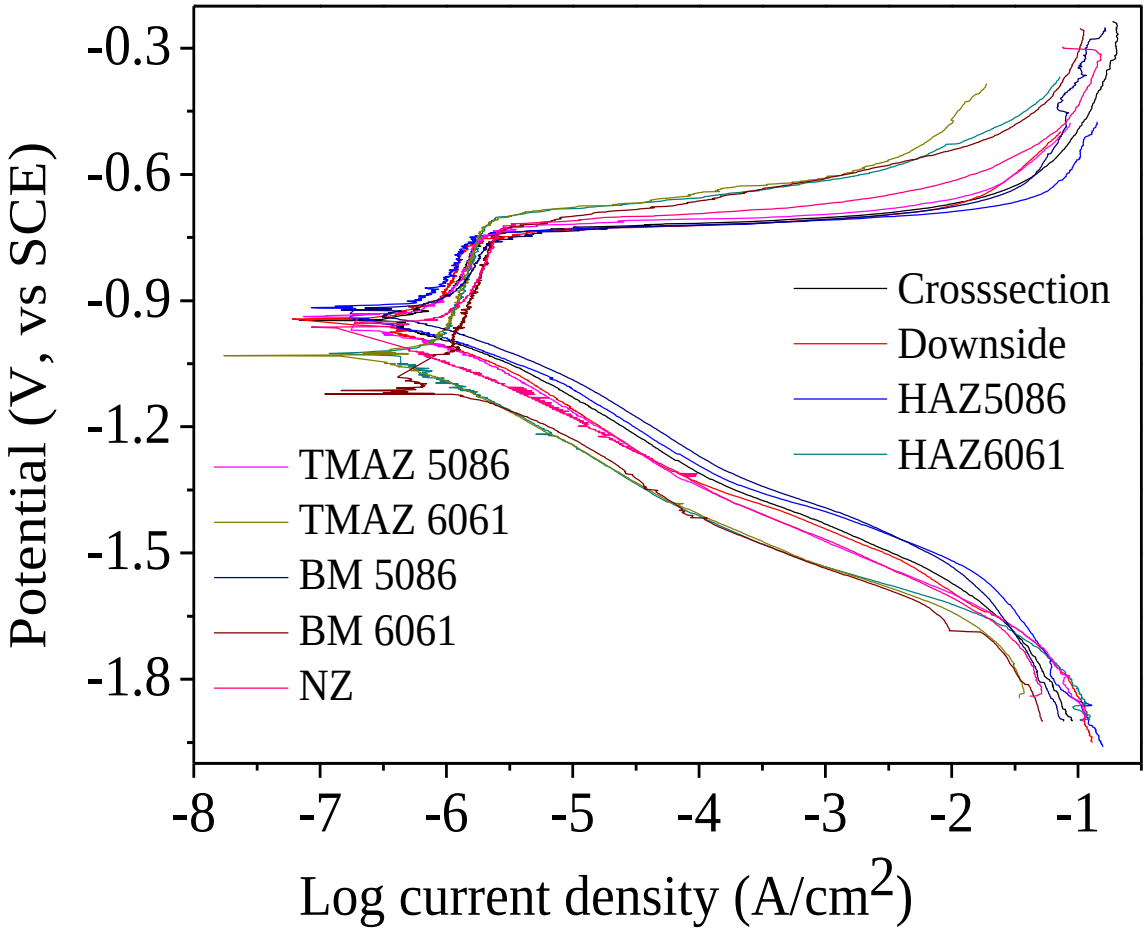

Figure 5.5 Polarization curves of different weld zones of FSW AA5086-AA6061 in deaerated 3.15 wt% NaCl solutions

Table 5.3 E_{corr}, I_{corr} and E_{pit} values of the different weld zones of FSW AA5086-AA6061 in deaerated 3.15 wt% NaCl solutions and standard deviation of I_{corr}

Weld	E_{corr} (mV, vs SCE)	E_{pit} (mV, vs SCE)	I_{corr} (μA/cm^2)	*S.D. of* I_{corr}
Cross-section	-947	-738	0.98	0.18
Downside	-944	-749	1.04	0.87
HAZ 5086	-917	-739	0.54	0.11
HAZ 6061	-1025	-705	1.17	0.46
TMAZ 5086	-937	-734	0.93	0.41
TMAZ 6061	-1031	-714	1.25	0.01
BM 5086	-953	-767	1.70	0.07
BM 6061	-1114	-724	2.44	0.71
NZ	-962	-718	1.21	0.33

Figure 5.5 shows polarization curves of different weld zones of FSW AA5086-AA6061 in deaerated 3.15 wt% NaCl solutions. The passive regions of FSW AA5086-AA6061 coupons in AA6061 side (BM-AA6061, HAZ-AA6061, and TMAZ-AA6061) were larger than those of the AA5086 side. E_{corr}, I_{corr} and E_{pit} values of the different positions of FSW AA5086-AA6061 in deaerated 3.15 wt% NaCl solutions are shown in Table 5.3. The E_{corr} values of cross-section (-947 mV_{SCE}) and downside (-944 mV_{SCE}) shifted to more anodic potentials from the BM-AA5086 (-953 mV_{SCE}) and BM-AA6061 (-1114 mV_{SCE}), while the E_{corr} value of the NZ was between the BM-AA5086 and BM-AA6061. The E_{corr} values of the HAZ-5086 (-917 mV_{SCE}) and the TMAZ-AA5086 (-937 mV_{SCE}) shifted to more positive potentials from those of the BM-AA5086 (-953 mV_{SCE}). The same results occurred on the AA6061 side. The I_{corr} values decreased compared to the BM, as shown in Table 5.3. The E_{pit} values of cross-section (-738 mV_{SCE}) and downside

(-749 mV_{SCE}) shifted to more negative potentials compared to those of the BM-AA5086 (-737 mV_{SCE}) and BM-AA6061 (-724 mV_{SCE}), while those of the NZ (-718 mV_{SCE}) shifted to more positive values. For the AA6061 side, the E_{pit} values of the HAZ-AA6061 (-705 mV_{SCE}) and the TMAZ-AA6061 (-714 mV_{SCE}) shifted to more positive values compared to those from the BM-AA6061 (-724 mV_{SCE}). The FSW improved corrosion resistance of the alloy mixtures compared to the AA5086 and AA6061 BM.

5.3.2 Effect of aerated solution

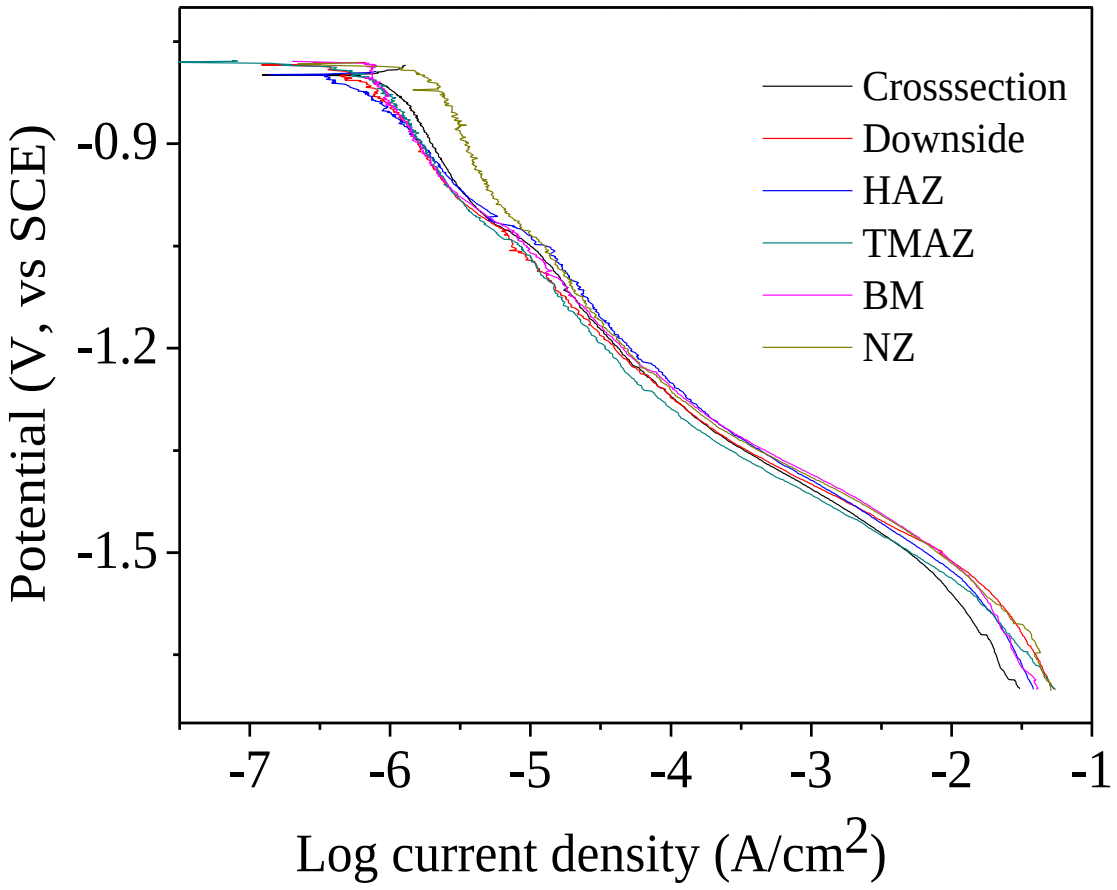

Figure 5.6 Cathodic polarization diagram of different weld zones of FSW AA5086-AA5086 in aerated 3.15 wt% NaCl solutions

Table 5.4 E_{corr} and I_{corr} values of the different weld zones of FSW AA5086-AA5086 in aerated 3.15 wt% NaCl solutions and standard deviation of I_{corr}

Weld	E_{corr} (mV, vs SCE)	I_{corr} (μA/cm^2)	*S.D. of* I_{corr}
Cross-section	-784	0.99	0.20
Downside	-780	0.64	0.03
HAZ	-793	0.65	0.07
TMAZ	-778	0.93	0.40
BM	-779	1.27	0.01
NZ	-780	0.98	0.40

Figure 5.6 shows cathodic polarization diagram of various weld zones of FSW AA5086-AA5086 in aerated 3.15 wt% NaCl solutions. In aerated 3.15 wt% NaCl, all of the weld zones of FSW AA5086-AA5086 generally showed Tafel behavior. Table 5.4 shows E_{corr} and I_{corr} values of the different weld zones of FSW AA5086-AA5086 in aerated 3.15 wt% NaCl solutions. The E_{corr} values of the cross-section (-784 mV_{SCE}), downside (-780 mV_{SCE}), HAZ (-793 mV_{SCE}), TMAZ (-778 mV_{SCE}), and NZ (-780 mV_{SCE}) shifted to slightly more negative than that of the BM (-779 mV_{SCE}). However, the I_{corr} values decreased from those of the BM (1.27 μA/cm^2). The I_{corr} values of HAZ (0.65 μA/cm^2) and downside (0.64 μA/cm^2) were similar. Also, the I_{corr} values of the cross-section (0.99 μA/cm^2), TMAZ (0.93 μA/cm^2), and NZ (0.98 μA/cm^2) were close.

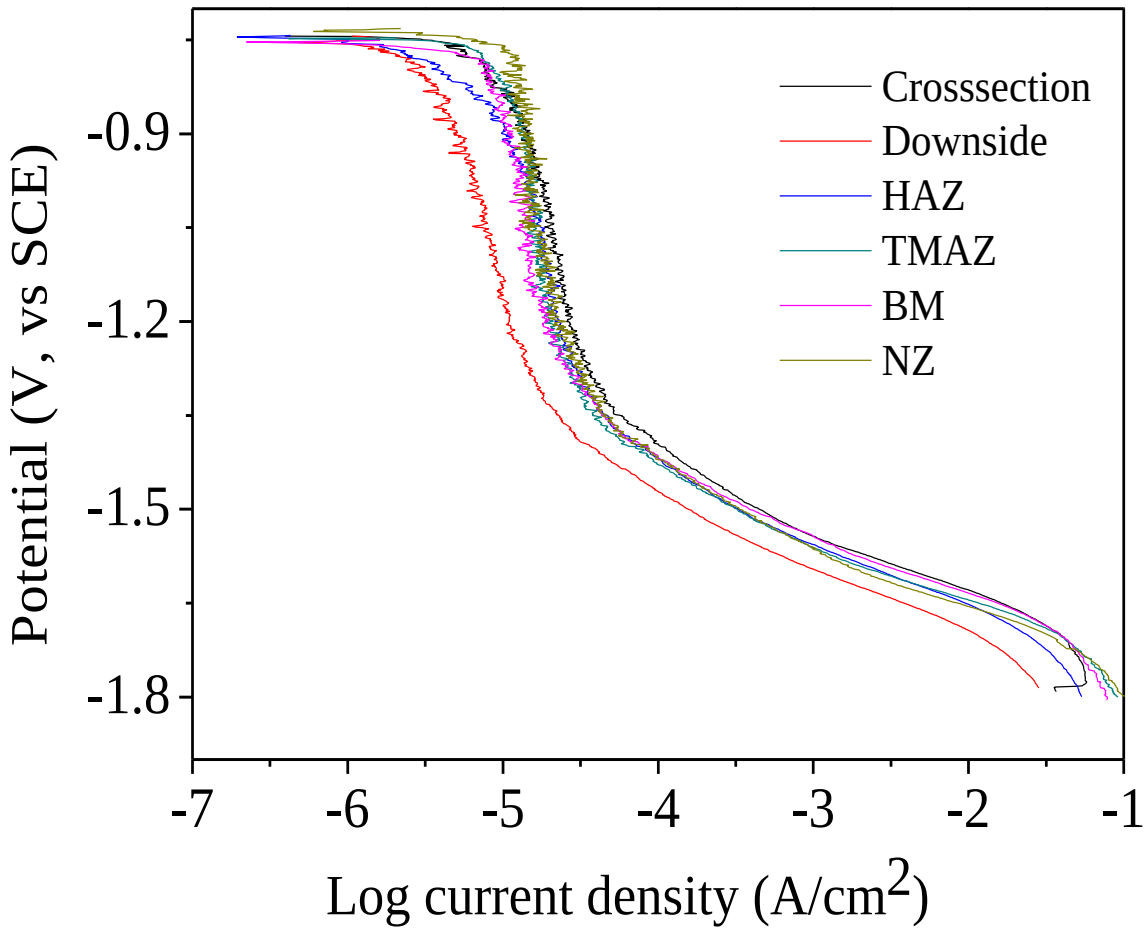

Figure 5.7 Cathodic polarization diagram of different weld zones of FSW AA6061-AA6061 in aerated 3.15 wt% NaCl solutions

Table 5.5 E_{corr} and I_{corr} values of the different weld zones of FSW AA6061-AA6061 in aerated 3.15 wt% NaCl solutions and standard deviation of I_{corr}

Weld	E_{corr} (mV, vs SCE)	I_{corr} (μA/cm^2)	*S.D. of* I_{corr}
Cross-section	-744	6.21	1.01
Downside	-743	3.85	0.58
HAZ	-742	2.87	0.82
TMAZ	-746	6.41	0.07
BM	-750	8.57	1.24
NZ	-731	5.02	1.56

Figure 5.7 shows cathodic polarization diagram of various weld zones of FSW AA6061-AA6061 in aerated 3.15 wt% NaCl solutions. In aerated 3.15 wt% NaCl, different weld zones of FSW AA6061-AA6061 showed behavior of diffusion limited oxygen reduction, which was different with FSW AA5086-AA5086. The E_{corr} and I_{corr} values of the various weld zones of FSW AA6061-AA6061 in aerated 3.15 wt% NaCl solutions are shown in Table 5.4. The E_{corr} values of the cross-section (-744 mV_{SCE}), downside (-743 mV_{SCE}), HAZ (-742 mV_{SCE}), TMAZ (-746 mV_{SCE}), and NZ (-731 mV_{SCE}) shifted to more positive values from that of the BM (-750 mV_{SCE}). The E_{corr} value was is also different from FSW AA5086-AA5086. The I_{corr} values decreased from that of the BM (8.57 μA/cm^2). Theses result show that FSW improved the corrosion resistance of welded AA6061-AA6061.

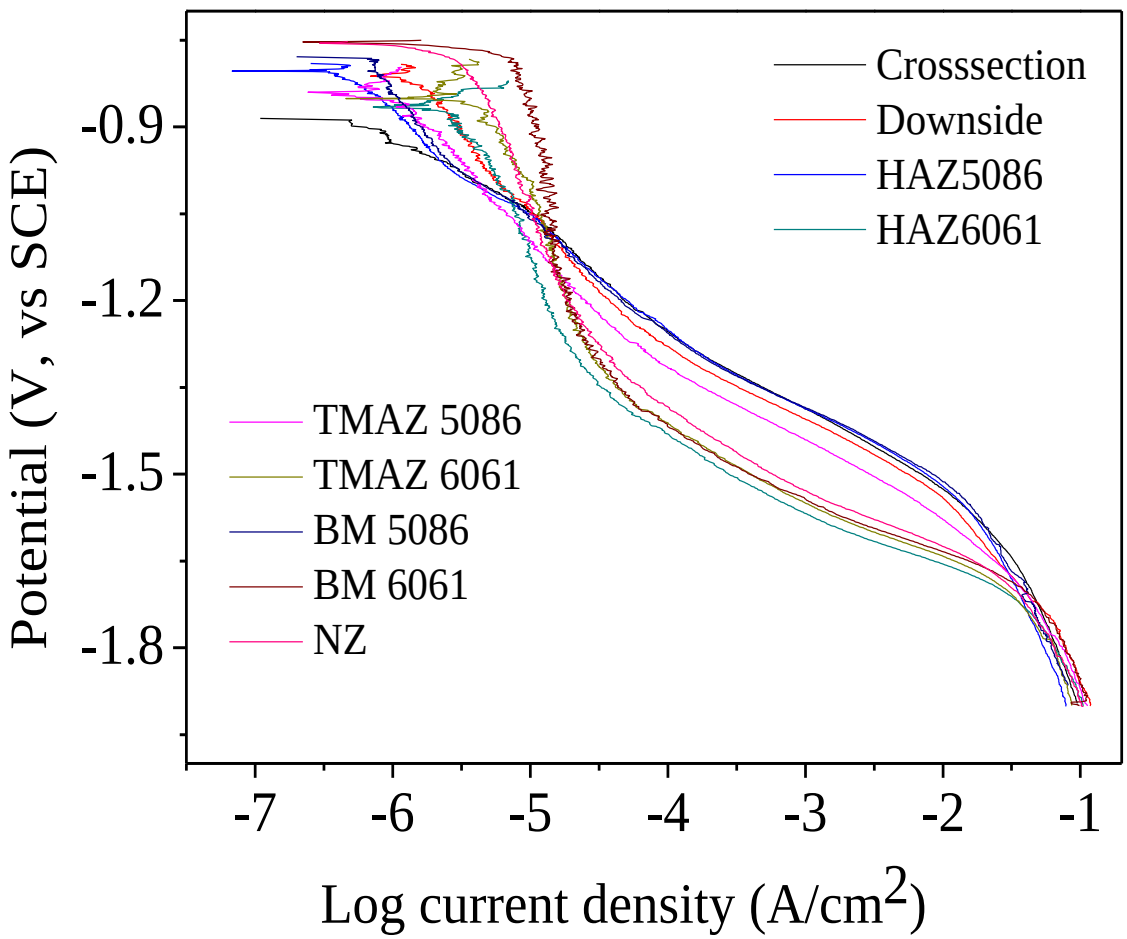

Figure 5.8 Cathodic polarization diagram of different weld zones of FSW AA5086-AA6061 in aerated 3.15 wt% NaCl solutions

Table 5.6 E_{corr} and I_{corr} values of the different weld zones of FSW AA5086-AA6061 in aerated 3.15 wt% NaCl solutions and standard deviation of I_{corr}

Weld	E_{corr} (mV, vs SCE)	I_{corr} (μA/cm^2)	*S.D. of* I_{corr}
Cross-section	-886	0.46	0.07
Downside	-792	1.88	1.59
HAZ 5086	-790	0.53	0.16
HAZ 6061	-820	0.56	0.17
TMAZ 5086	-797	0.87	0.15
TMAZ 6061	-783	4.73	2.09
BM 5086	-779	1.27	0.01
BM 6061	-750	8.57	1.24
NZ	-753	1.44	0.39

Figure 5.8 shows a cathodic polarization diagram of different weld zones of FSW AA5086-AA6061 in aerated 3.15 wt% NaCl solutions. In aerated 3.15 wt% NaCl the regions of HAZ-AA6061, TMAZ-AA6061, BM-AA6061, and upside show behavior of diffusion-limited oxygen reduction, while the regions of cross-section, downside, HAZ-AA5086, TMAZ-AA5086, and BM-AA5086 show Tafel behavior. Table 5.6 shows E_{corr} and I_{corr} values of the different weld zones of FSW AA5086-AA6061 in aerated 3.15 wt% NaCl solutions. The E_{corr} values of different weld zones of FSW AA5086-AA6061 shifted to more negative values those of BM-AA5086 (-779 mV_{SCE}) and BM-AA6061 (-753 mV_{SCE}). Compared to the BM-AA6061 (8.57 μA/cm^2), the I_{corr} values of the downside (1.88 μA/cm^2), HAZ-AA6061 (0.56 μA/cm^2), TMAZ-AA6061 (4.73 μA/cm^2), and NZ (1.44 μA/cm^2) decreased. Also, the I_{corr} values of cross-section (0.46 μA/cm^2),

HAZ-AA5086 (0.53 μA/cm^2), and TMAZ (0.87 μA/cm^2) decreased compared to those of BM-AA5086 (1.27 μA/cm^2).

Chapter 6

Corrosion Properties

6.1 Introduction

The immersion experiments were conducted to study the corrosion properties of FSW AA5086-AA5086, AA5086-AA6061, and AA6061-AA6061 Al alloys. Specimens of FSW AA5086-AA5086, AA5086-AA6061, and AA6061-AA6061 Al alloys were soaked in 3.15 wt% NaCl, 0.5 M Na_2SO_4, and ASTM seawater for 90 days and 120 days at 30°C. The ionic compositions of each solution are discussed in Chapter 3.

6.2 Experimental

Table 6.1 shows the immersion experiments that we designed. The FSW AA5086-AA5086, AA5086-AA6061, and AA6061-AA6061 Al alloys plates were machined to the following dimensions: 70 mm × 25 mm × 5mm. A BenchMark 320 marking system was used to pin stamps the coupons for identification. The FSW coupons were first cleaned in acetone to remove any oil residue. Next they were cleaned ultrasonically in 18.1 MΩ-cm water for 20 minutes after which they were dried at room temperature. All coupons were weighed three times to obtain the initial mass. The coupons were individually placed in each of the 250 ml beakers. The specimens were oriented in the beakers such that they made a 45° angle with the horizontal, and the "downside" (side with the smaller NZ (Figure 4.1)) of the samples was facing downward. Three different solutions were added to each beaker. Approximately 200 ml of each solution was poured into the beakers so that the coupons were completely immersed. We made sure there were no bulbs on the surface of the coupons. The 24 beakers were distributed and placed in a 76 cm × 31 cm ×

32 cm glass tank. Each glass tank was kept at 30°C in a de-ionized water bath using automatic aquarium heater. One aquarium pump was installed inside each glass tank to circulate the water in the bath. This setup maintained a uniform temperature in the water bath, which kept the solutions inside the beakers at a constant temperature. Each beaker was partially covered to keep the evaporation of the solution to a minimum, also ensuring an aerated condition. Figure 6.1 shows the immersion setup with couples immersed in different solutions inside the beakers.

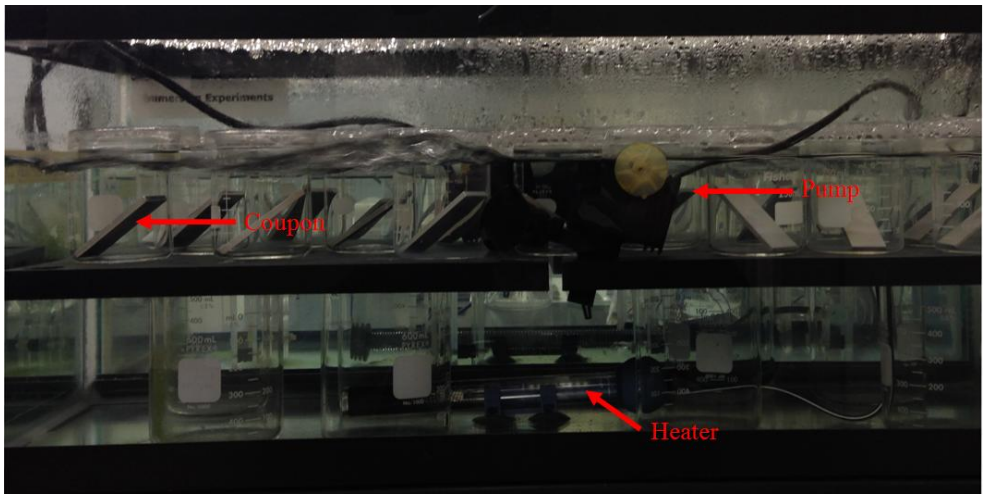

Figure 6.1 Immersion setup

Table 6.1 The number of coupons, duration of immersion, and types of electrolyte used for the corrosion tests at 30°C for the FSW AA5086-AA5086, AA5086-AA6061, and AA6061-AA6061 specimens

Name	Time	3.15 wt% NaCl	0.5 M Na_2SO_4	ASTM Sea Water
5086-5086	90 Days	4	4	4
	120 Days	4	4	4
5086-6061	90 Days	4	4	4
	120 Days	4	4	4
6061-6061	90 Days	4	4	4
	120 Days	4	4	4

6.3 Visual results of immersed FSW samples

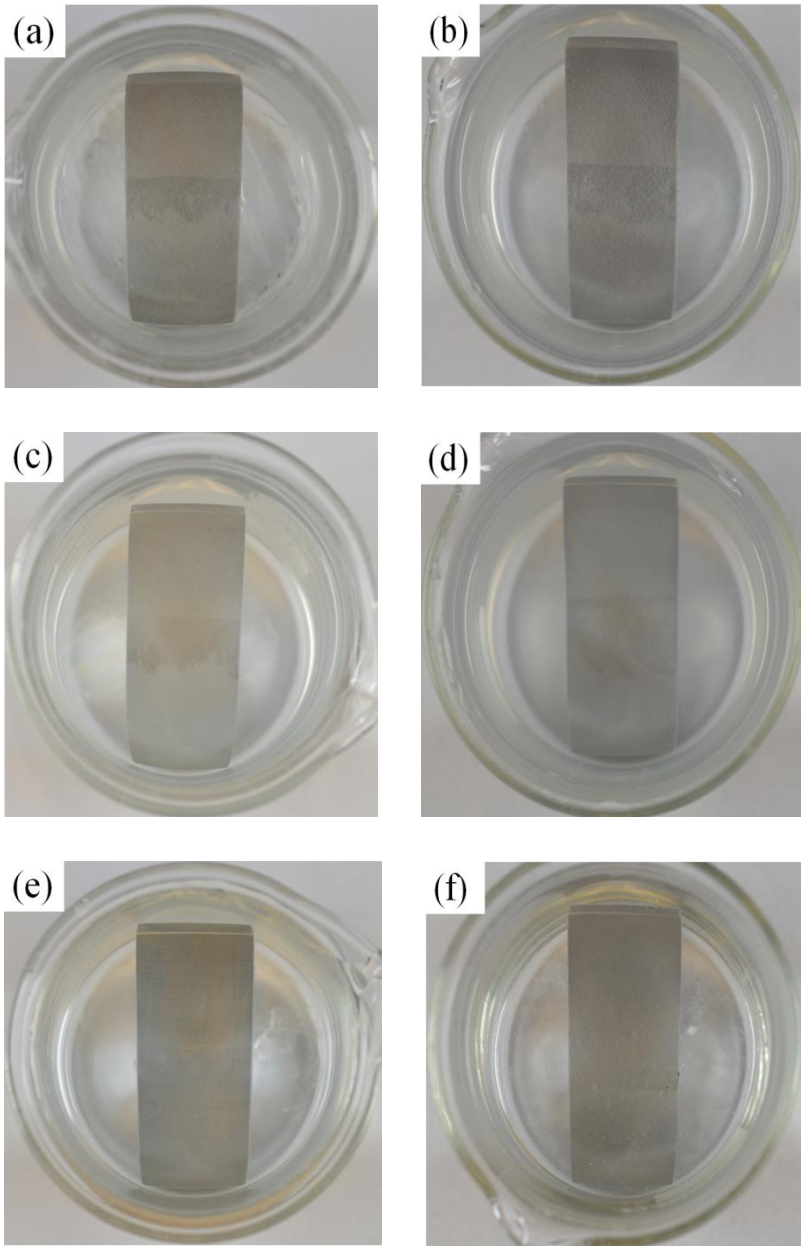

Figure 6.2 FSW 5086-5086 coupons after immersion in (a) 3.15 wt% NaCl for 90 days, (b) 3.15 wt% NaCl for 120 days, (c) ASTM seawater for 90 days, (d) ASTM seawater for 120 days, (e) 0.5 M Na_2SO_4 for 90 days, and (f) 0.5 M Na_2SO_4 for 120 days

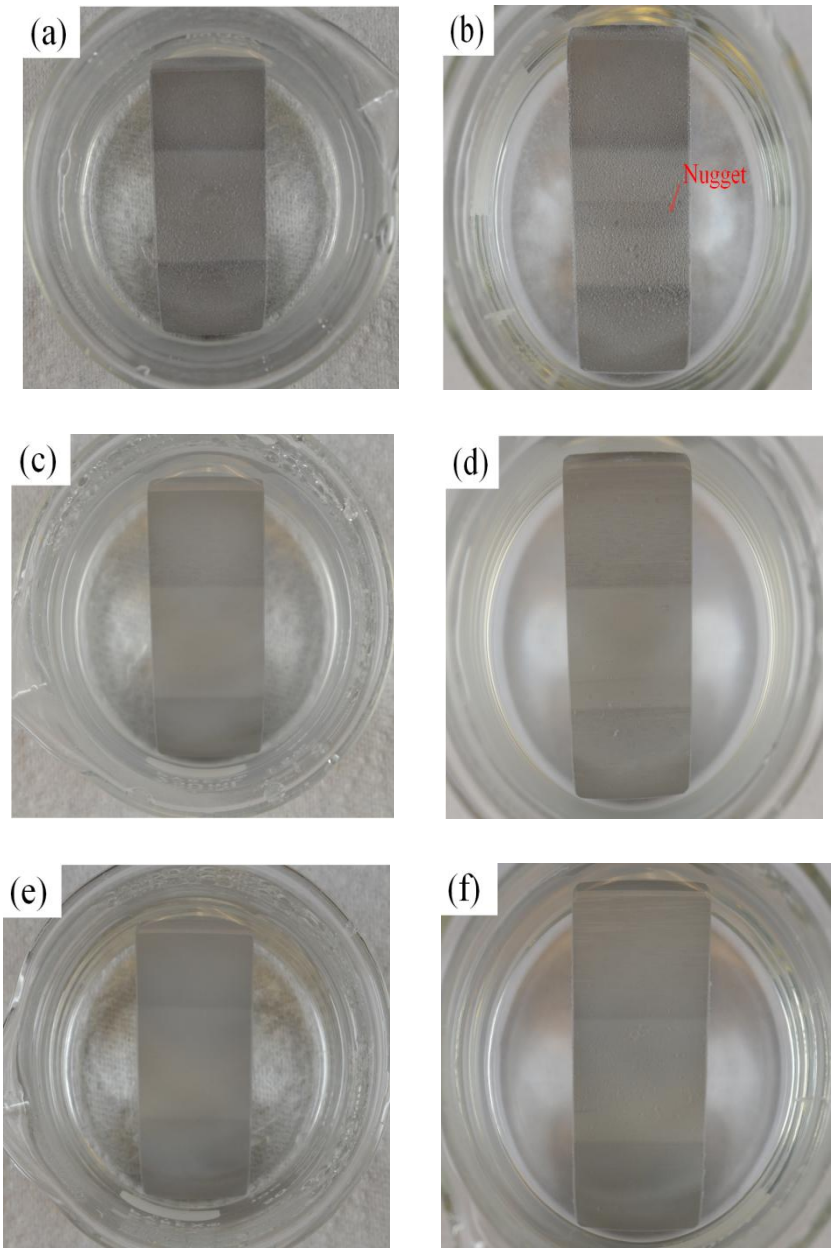

Figure 6.3 FSW 6061-6061 coupons after immersion in (a) 3.15 wt% NaCl for 90 days, (b) 3.15 wt% NaCl for 120 days, (c) ASTM seawater for 90 days, (d) ASTM seawater for 120 days, (e) 0.5 M Na_2SO_4 for 90 days, and (f) 0.5 M Na_2SO_4 for 120 days

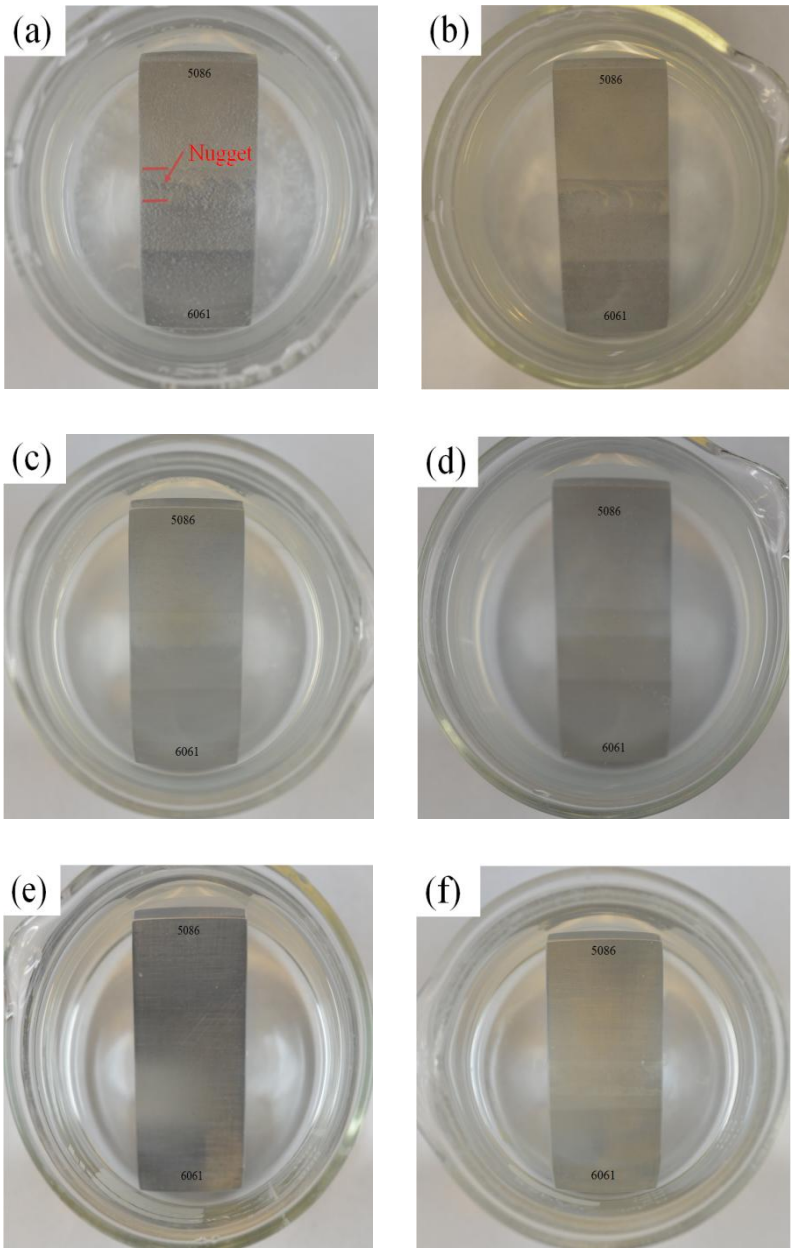

Figure 6.4 FSW 5086-6061 coupons after immersion in (a) 3.15 wt% NaCl for 90 days, (b) 3.15 wt% NaCl for 120 days, (c) ASTM seawater for 90 days, (d) ASTM seawater for 120 days, (e) 0.5 M Na_2SO_4 for 90 days, and (f) 0.5 M Na_2SO_4 for 120 days

Figure 6.2 shows FSW AA5086-AA5086 coupons after immersion in 3.15 wt% NaCl, ASTM seawater, and 0.5 M Na_2SO_4 solutions for 90 and 120 days. For the FSW AA5086-AA5086 specimens in the 90 and 120 day immersion tests, the highest amount of corrosion products were observed on the specimens in the 3.15 wt% NaCl followed by those in ASTM seawater, and then 0.5 M Na_2SO_4. The weld-affected regions (central section) of the FSW 5086-5086 coupons in 3.15wt% NaCl became dark in color after immersion for 90 and 120 days (Figure 6.2 (a) and (b)). The similar color changes were observed in ASTM seawater after immersion for 90 and 120 days (Figure 6.2 (c) and (d)). However, there was almost no corrosion observed in 0.5 M Na_2SO_4 after 90 and 120 days of immersion (Figure 6.2 (e) and (f)).

Figure 6.3 also shows FSW AA6061-AA6061 coupons in 3.15wt% NaCl, ASTM seawater, and 0.5 M Na_2SO_4 solutions after 90 and 120 days of immersion. In Figure 6.3 (a) after 90 days immersion, the BM of FSW AA6061-AA6061 became much darker than the welded region in 3.15 wt% NaCl. There was also more corrosion product on the BM. However after 120 days of immersion in 3.15 wt% NaCl, the NG region also became darker than the other welded regions, as shown in Figure 6.3 (b), After 90 and 120 days immersion in ASTM seawater and 0.5 M Na_2SO_4, the BM was much darker than the welded region (Figure 6.3 (c), (d), (e), and (f)). A comparison between Figure 6.2 and Figure 6.3 shows that there is more corrosion product on FSW AA6061-AA6061 coupons than FSW AA5086-AA5086 coupons in same immersion condition.

Figure 6.4 shows FSW AA5086-AA6061 coupons in 3.15wt% NaCl, ASTM seawater, and 0.5 M Na_2SO_4 solutions after 90 and 120 days immersion. In 3.15 wt% NaCl and ASTM seawater, the BM-AA6061 side was much darker than the BM-AA5086 side

(Figure 6.4 (a), (b), (c), and (d)), while the welded regions of those coupons were more complex. The NZ and adjacent regions contain a mixture of AA5086 and AA6061 due to solid-state mixing during the FSW process. Two colors indicate the different corrosion rates of AA5086 and AA6061. As shown in Figure 6.4 (e), there was almost no corrosion product on the surface of FSW AA5086-AA6061 coupons after 90 days immersion in 0.5 M Na_2SO_4 solution. After 120 days immersion in 0.5 M Na_2SO_4 solution, there was much more corrosion product on the BM-AA6061 side than on the BM-AA5086 side. Actually, there was almost no corrosion product on the BM-AA5086 side after immersion for 120 days in 0.5 M Na_2SO_4 solution.

6.4 X-Ray Diffraction

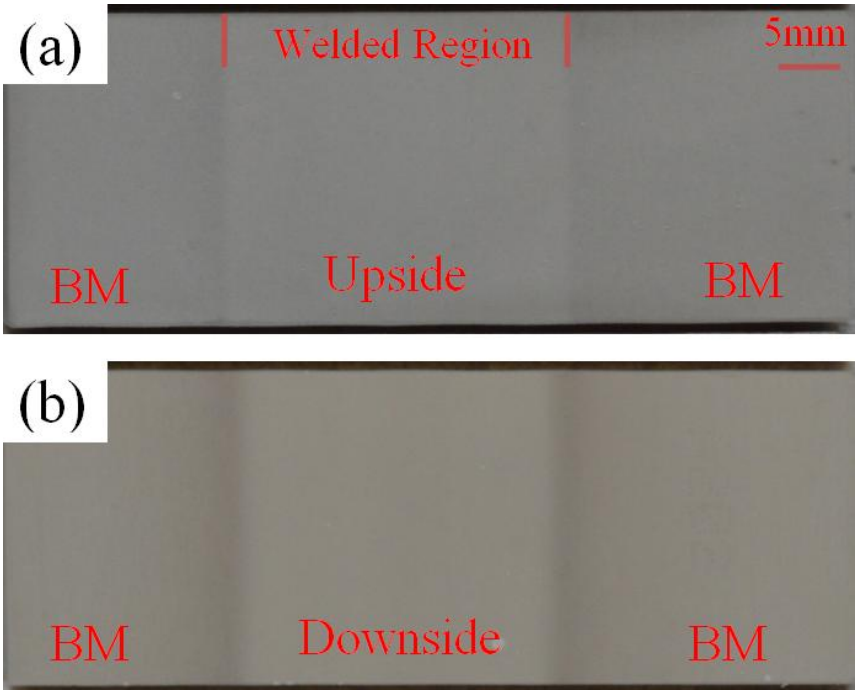

Figure 6.5 Coupon of FSW AA6061-AA6061 after 90 days immersion in ASTM seawater (a) upside and (b) downside

In Figure 6.5 it is apparent that the BM is much darker than the welded region. The size of the upside and downside of the welded region was also different as result of process of

the FSW. We used XRD to characterize corrosion product of the upside, downside and BM (from the FSW specimen). Due to the relatively large sampling region needed while obtaining the XRD spectra, the "downside" spectra contains the NZ, TMAZ, and HAZ.

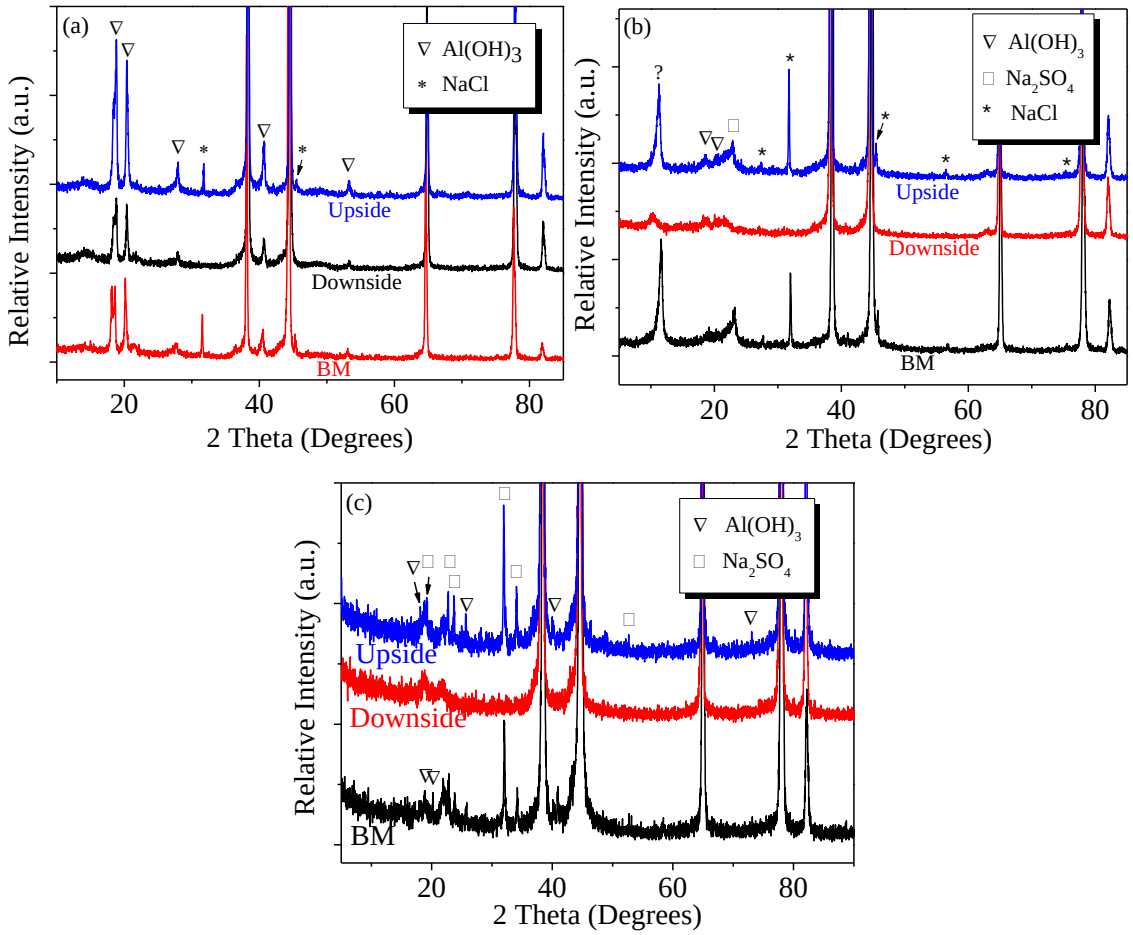

Figure 6.6 XRD of FSW AA5086-AA5086 after 90 days immersion in (a) 3.15 wt% NaCl, (b) ASTM seawater, and (c) 0.5 M Na_2SO_4 solution

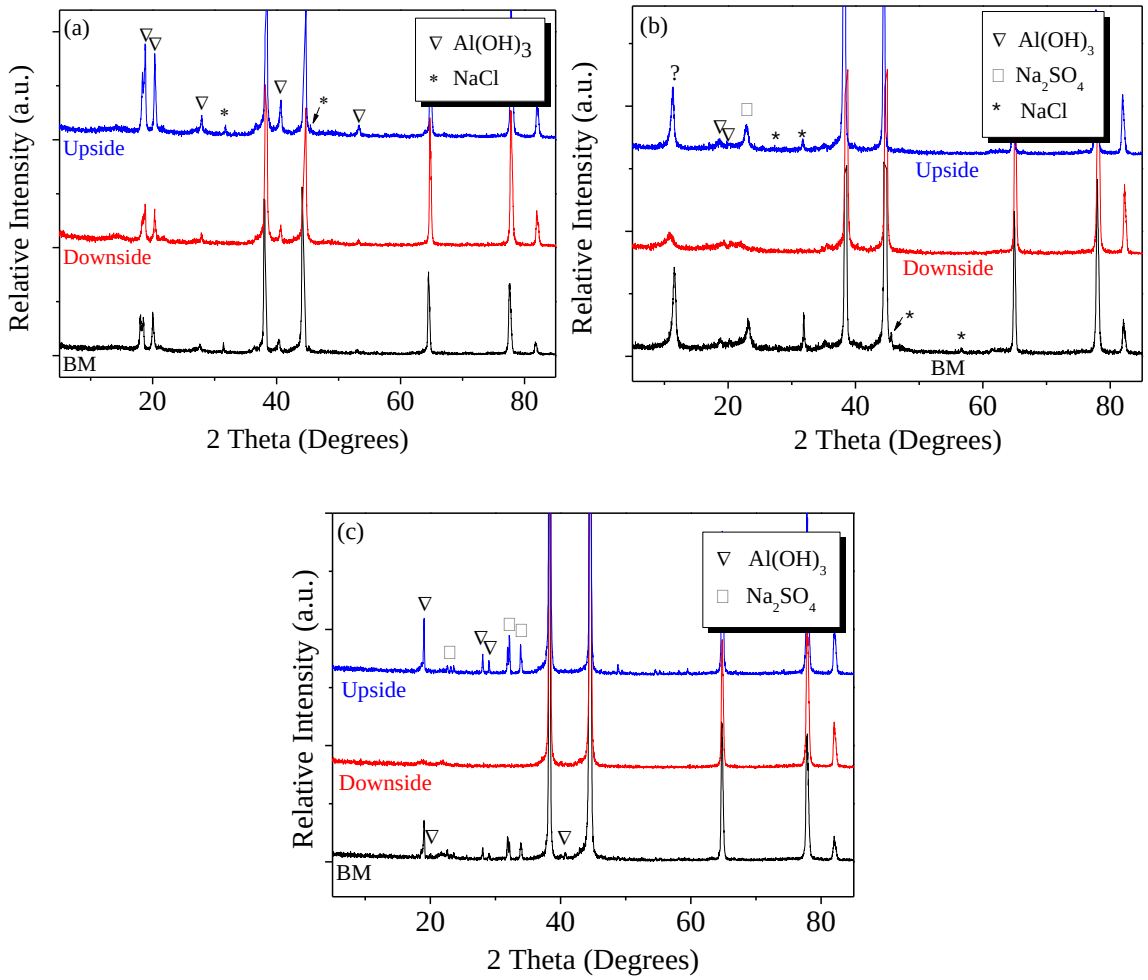

Figure 6.7 XRD of FSW AA5086-AA5086 after 120 days immersion in (a) 3.15 wt% NaCl, (b) ASTM seawater, and (c) 0.5 M Na_2SO_4 solution

Figure 6.6 shows XRD of FSW AA5086-AA5086 after 90 days immersion in 3.15 wt% NaCl, ASTM seawater, and 0.5 M Na_2SO_4 solution. XRD results reveal aluminum hydroxide ($Al(OH)_3$, Bayerite) as the main corrosion product on FSW AA5086-AA5086 coupons immersed in those three solutions. XRD results also contain sodium chloride (NaCl) in Figure 6.6 (a), NaCl and Na_2SO_4 in Figure 6.6 (b), and Na_2SO_4) in Figure 6.6 (c). The NaCl and Na_2SO_4 in XRD results from immersion solutions are not corrosion products, which is because we take coupons out from immersion solutions without cleaning. There is unknown peak in ASTM seawater solution (Figure 6.6 (b)). Figure 6.7

shows an XRD of FSW AA5086-AA5086 after 120 days immersion in 3.15 wt% NaCl, ASTM seawater, and 0.5 M Na_2SO_4 solution. Aluminum hydroxide ($Al(OH)_3$)was also main corrosion product after 120 immersion in three different solutions. The XRD results were identical in the same immersion solution, although the immersion times were different. As shown in Figures 6.6 and 6.7 there were fewer peaks of $Al(OH)_3$, NaCl Na_2SO_4 and in the downside region than in the upside and BM regions.

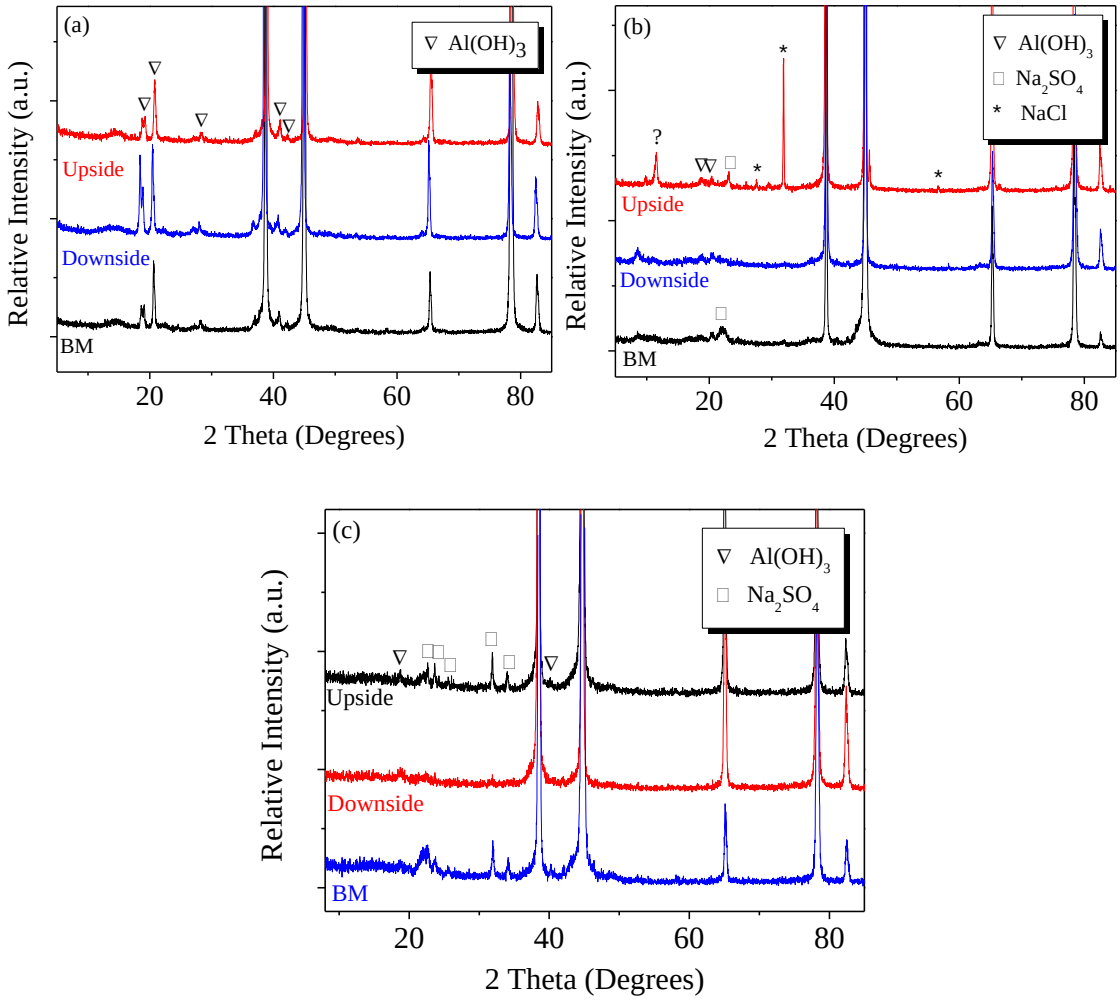

Figure 6.8 XRD of FSW AA6061-AA6061 after 90 days immersion in (a) 3.15 wt% NaCl, (b) ASTM seawater, and (c) 0.5 M Na_2SO_4 solution

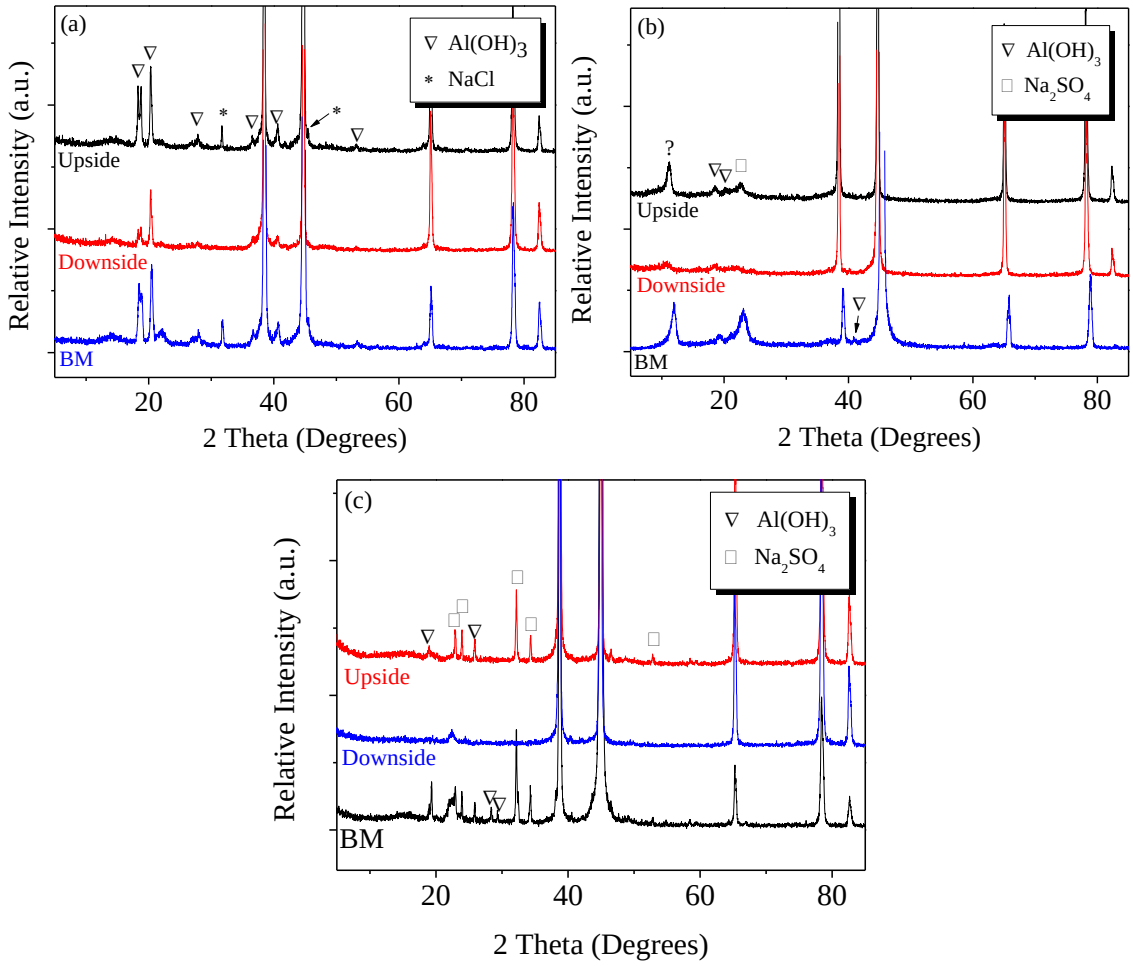

Figure 6.9 XRD of FSW AA6061-AA6061 after 120 days immersion in (a) 3.15 wt% NaCl, (b) ASTM seawater, and (c) 0.5 M Na_2SO_4 solution

Figures 6.8 and 6.9 show XRD of FSW 6061-6061 in 3.15 wt% NaCl, ASTM seawater, and 0.5 M Na_2SO_4 solution after 90 and 120 days immersion, respectively. For FSW 6061-6061 coupons, $Al(OH)_3$ was also main corrosion product in the three different solution immersion experiments. Because there were two weak peaks of NaCl, we did not mark them in the diagram (Figure 6.8 (a)). There were also unknown peaks in ASTM seawater after 90 and 120 days immersion (Figure 6.8 (b) and Figure 6.9 (b)). As shown in Figure 6.8 (c) and Figure 6.9 (c), there were more peaks of corrosion product $Al(OH)_3$ on the upside and BM regions after 120 days immersion than after 90 days. There were also fewer peaks of $Al(OH)_3$, NaCl, Na_2SO_4 in downside region than in the upside and

BM regions (Figures 6.8 and 6.9) The NaCl and Na_2SO_4 peaks shown in Figures 6.8 and 6.9 are smaller than those in with Figures 6.6 and 6.7.

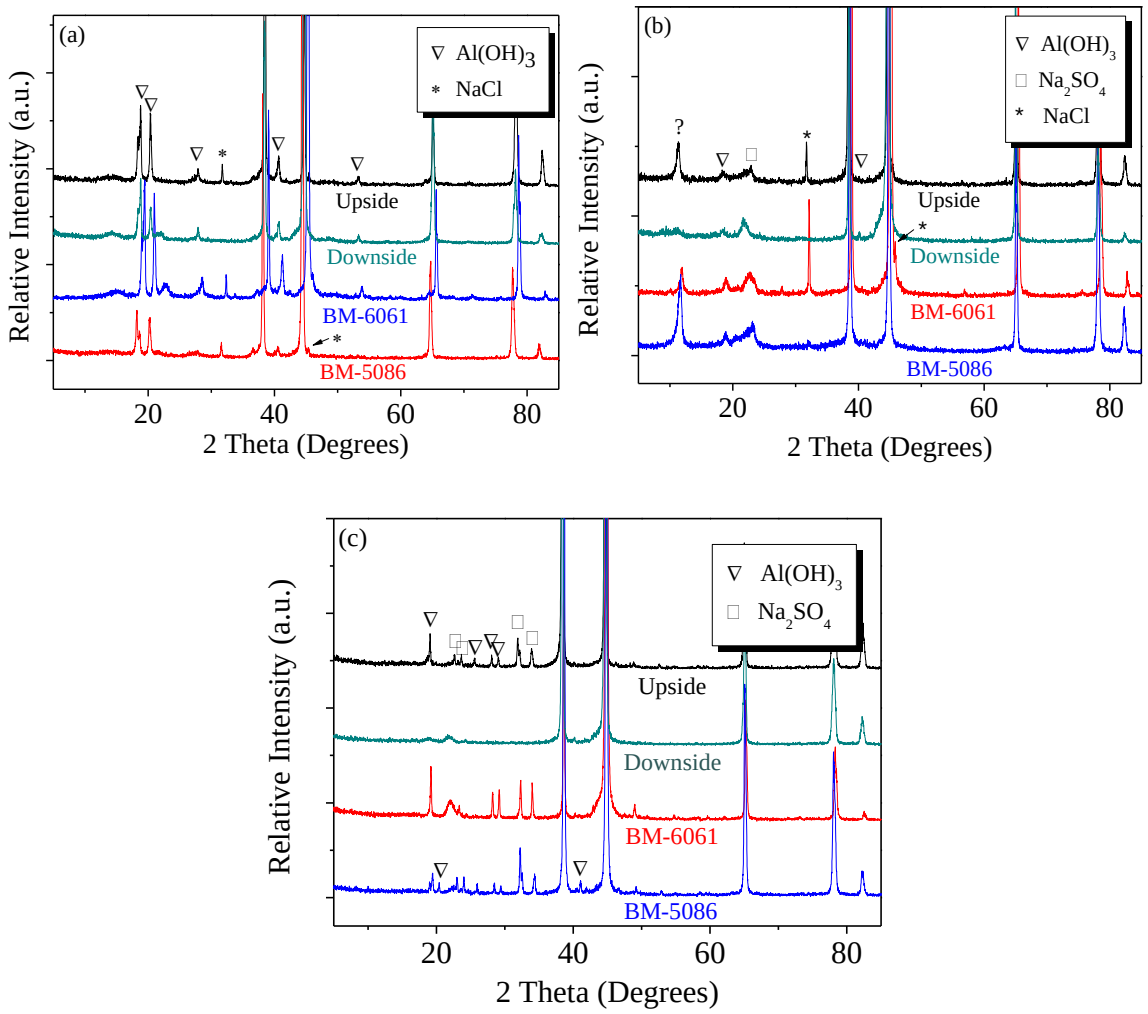

Figure 6.10 XRD of FSW AA5086-AA6061 after 90 days immersion in (a) 3.15 wt% NaCl, (b) ASTM seawater, and (c) 0.5 M Na_2SO_4 solution

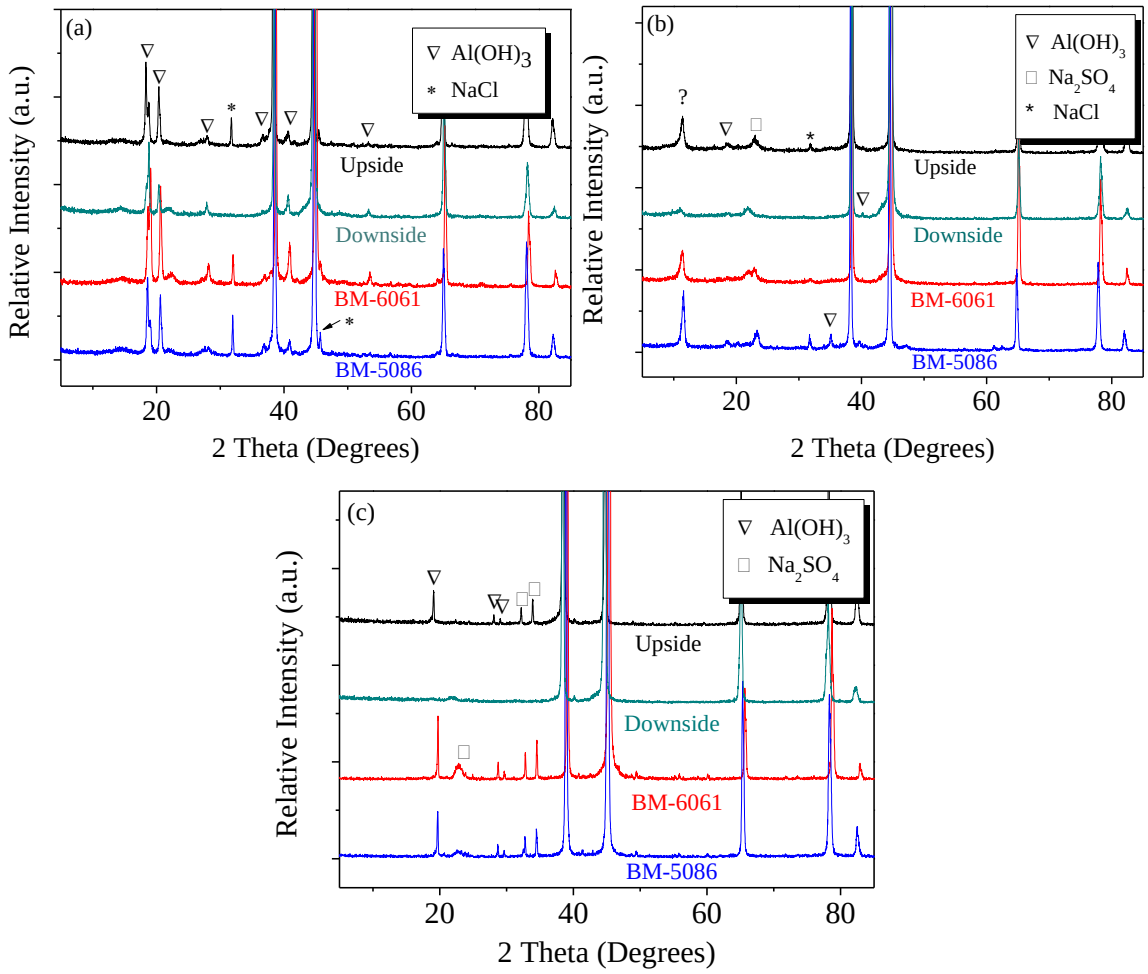

Figure 6.11 XRD of FSW AA5086-AA6061 after 120 days immersion in (a) 3.15 wt% NaCl, (b) ASTM seawater, and (c) 0.5 M Na_2SO_4 solution

Figures 6.10 and 6.11 reveal XRD results of FSW AA5086-AA6061 in 3.15 wt% NaCl, ASTM seawater, and 0.5 M Na_2SO_4 solution after 90 and 120 days immersion, respectively. Aluminum hydroxide was also the main corrosion product for FSW AA5086-AA6061 coupons in three different solution immersion experiments. There were still unknown peaks in ASTM seawater after 90 and 120 days immersion (Figure 6.10 (b) and Figure 6.11 (b)). Figure 6.4 showed that there was more corrosion product on the BM-AA6061 side than on the BM-AA5086 side. Therefore, in XRD results there were more peaks of $Al(OH)_3$ on the BM-AA6061 side than on the BM-AA5086 side. As shown in Figures 6.10 and 6.11, there were fewer peaks of $Al(OH)_3$, NaCl, and Na_2SO_4

in the downside region than in the upside, BM-AA6061, and BM-AA5086 regions, especially in ASTM seawater and 0.5 M Na_2SO_4. The peaks of NaCl and Na_2SO_4 were from immersion solutions for FSW AA5086-AA6061 coupons, which were similar to the result for immersion FSW AA5086-AA5086 and AA6061-AA6061.

6.5 Raman Spectroscopy

In Chapter 4 we discussed the microstructure of FSW AA5086-AA5086, AA6061-AA6061, and AA5086-AA6061, which includes six distinct zones: NZ, TMAZ, HAZ, BM, downside, and cross-section. For coupons of immersion experiments, we selected five distinct zones (NZ, TMAZ, HAZ, BM, and downside) to characterize corrosion products by using Raman spectroscopy. Because the Raman technique is highly localized, the downside contains only the NZ region, unlike that the XRD spectra of the downside that included the NZ, TMAZ, and HAZ. The figures that follow depict the results obtained via Raman spectroscopy for distinct regions of FSW AA5086-AA5086, AA5086-AA6061, and AA6061-AA6061 after 90 and 120 days in 3.15 wt% NaCl, ASTM seawater, and 0.5 M Na_2SO_4. The Y-axis for all Raman results was a relatively intensity value, whereas the X-axis was the more important Raman shift in cm^{-1}, which reveals the band locations of corrosion products.

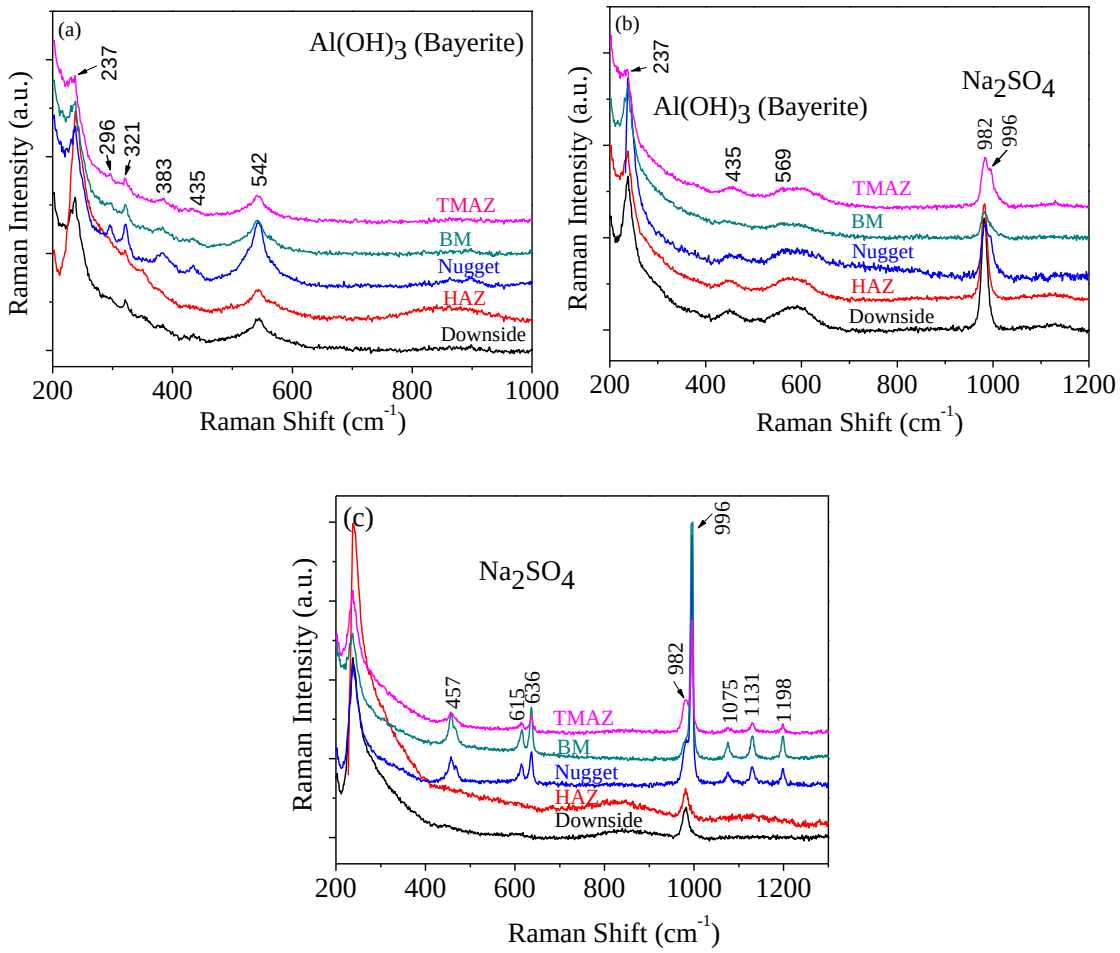

Figure 6.12 Raman spectroscopy of distinct zones of FSW AA5086-AA5086 after 90 days immersion in: (a) 3.15 wt% NaCl, (b) ASTM seawater, and (c) 0.5 M Na_2SO_4 solution

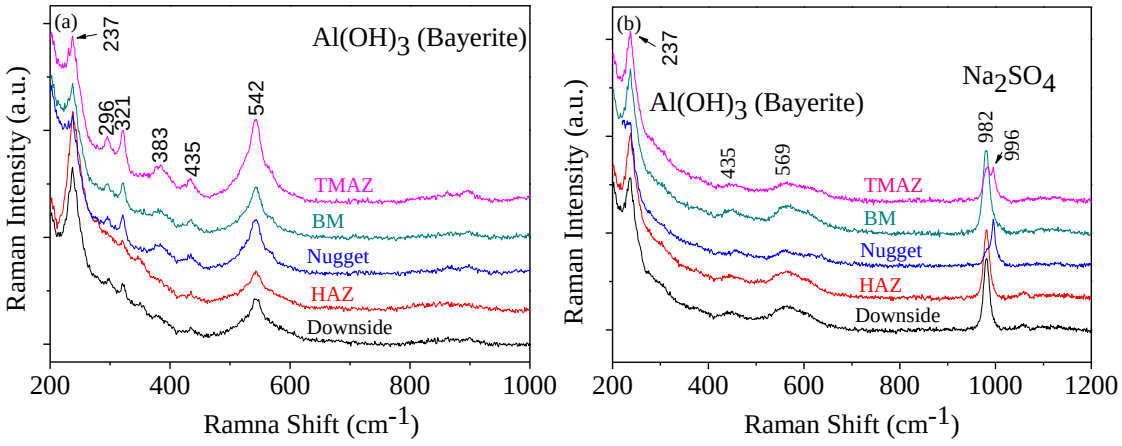

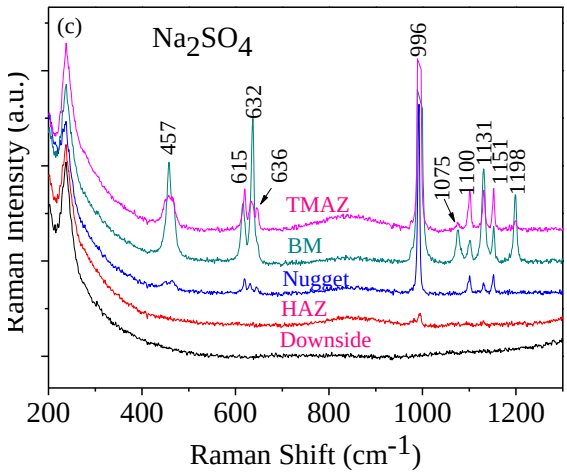

Figure 6.13 Raman spectroscopy of distinct zones of FSW AA5086-AA5086 after 120 days immersion in: (a) 3.15 wt% NaCl, (b) ASTM seawater, and (c) 0.5 M Na_2SO_4 solution

Figure 6.12 shows Raman spectroscopy of distinct zones of FSW AA5086-AA5086 after 90 days immersion in 3.15 wt% NaCl, ASTM seawater, and 0.5 M Na_2SO_4 solution. Characteristic bands of $Al(OH)_3$ (237, 296, 321 383,435, and 542 cm^{-1}) were observed for five distinct regions after immersion 90 days in 3.15 wt% NaCl (Figure 6.12 (a)) [67]. XRD results from Figure 6.6 (a) agree with this Raman analysis. In Figure 6.12 (b), characteristic bands of $Al(OH)_3$ (237, 435, and 569 cm^{-1}) and Na_2SO_4 (982 and 996 cm^{-1}) (identified by rruff.info) were observed for five distinct regions after immersion 90 days in ASTM seawater. Aluminum hydroxide was the main corrosion product for FSW 5086-5086 after 90 days immersion in 3.15 wt% NaCl, and ASTM seawater. In Figure 6.12 (c), characteristic bands of Na_2SO_4 (457, 615, 636, 996, 1075, and 1131 cm^{-1}) were observed in TMAZ, BM, and Nugget except zones of HAZ and downside. However, characteristic band (1198 cm^{-1}) cannot be identified. Figure 6.13 shows Raman spectroscopy of distinct zones of FSW AA5086-AA5086 after 120 days immersion in 3.15 wt% NaCl, ASTM seawater, and 0.5 M Na_2SO_4 solution. Characteristic bands in Figure 6.13 (a) are similar with Figure 6.12 (a), and Figure 6.13 (b) is also similar with Figure 6.12 (b). Figure 6.13

(b) appears new characteristic bands of 1075 cm^{-1}, which also cannot be identified. In Figure 6.12 (c) and 6.13 (c), Raman data of $Al(OH)_3$ bands immersed in 0.5 M Na_2SO_4 solution was missing as the amount of corrosion product present may have been insignificant for the Raman to detect.

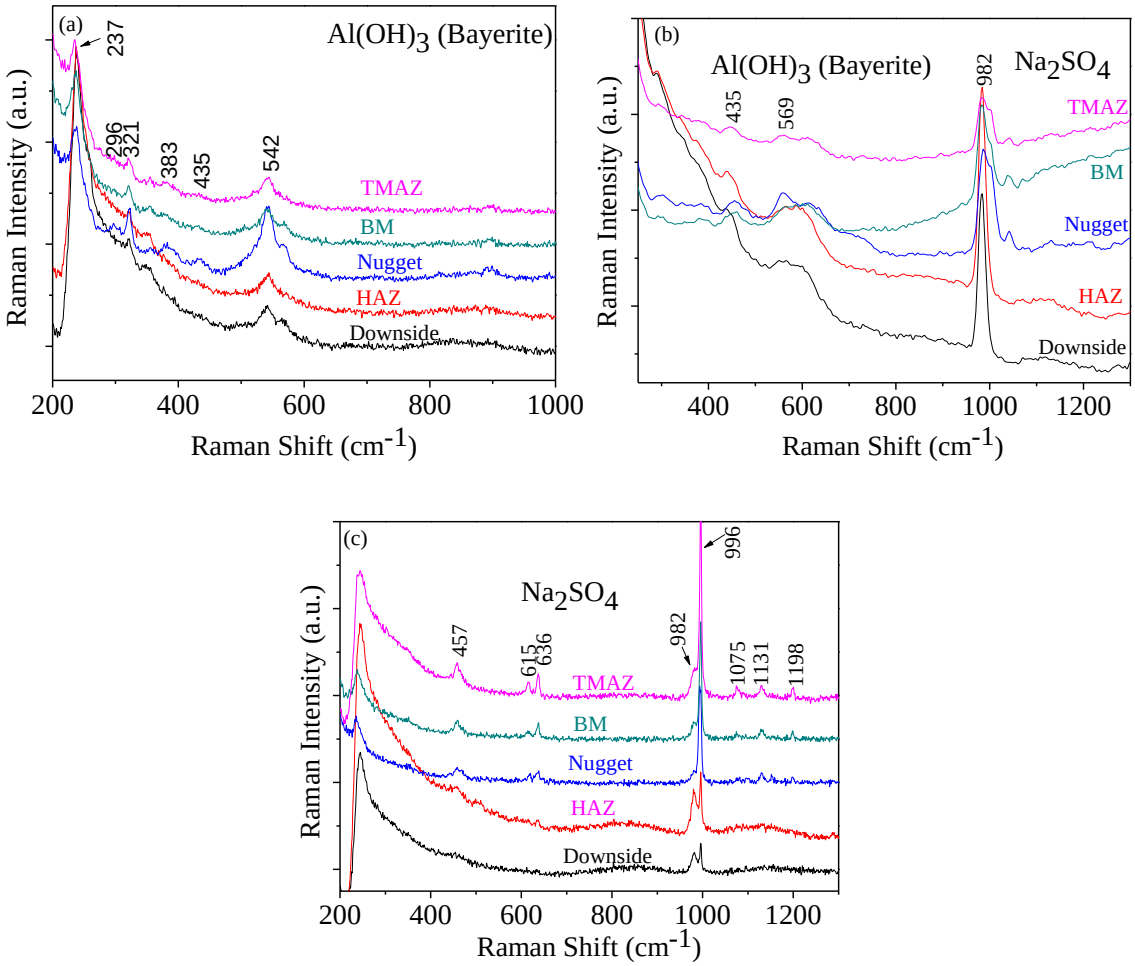

Figure 6.14 Raman spectroscopy of distinct zones of FSW AA6061-AA6061 after 90 days immersion in: (a) 3.15 wt% NaCl, (b) ASTM seawater, and (c) 0.5 M Na_2SO_4 solution

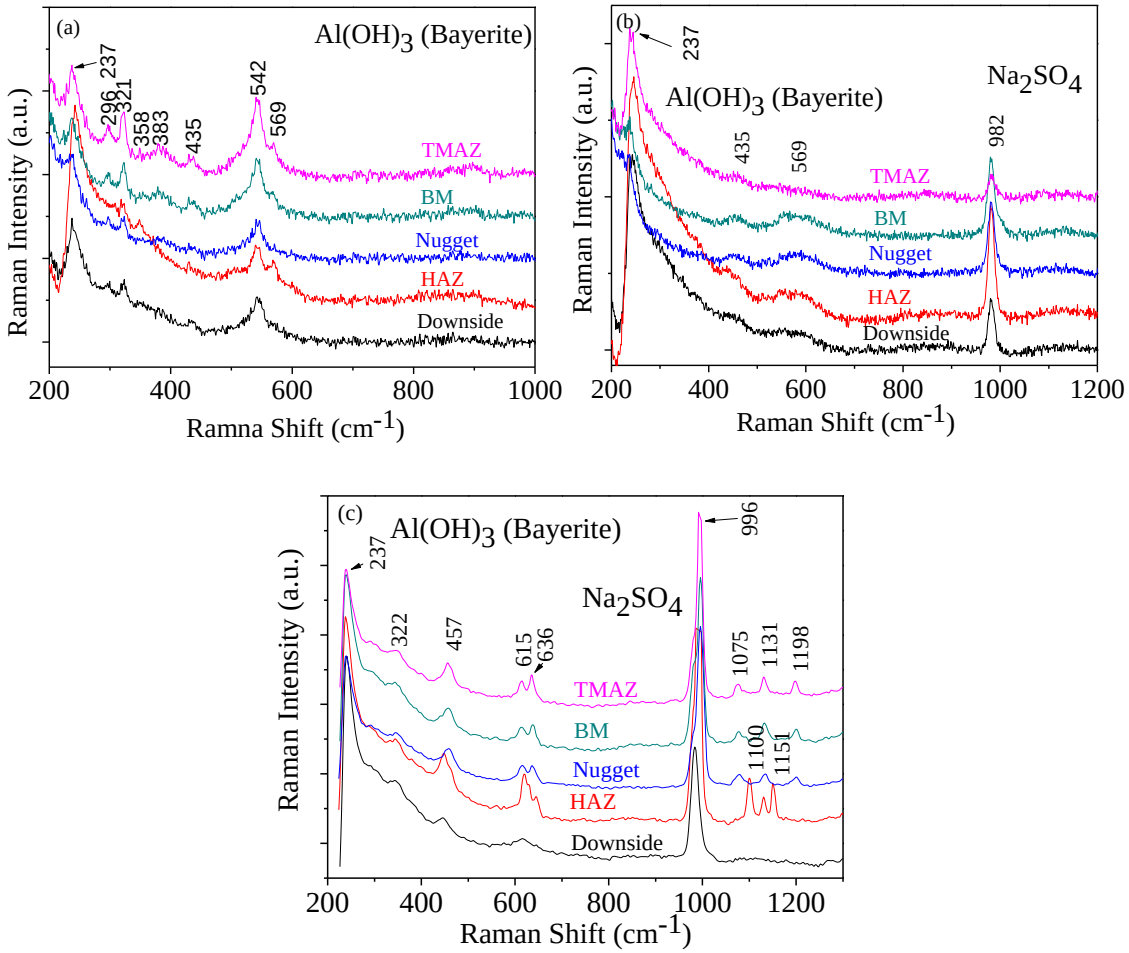

Figure 6.15 Raman spectroscopy of distinct zones of FSW AA6061-AA6061 after 120 days immersion in: (a) 3.15 wt% NaCl, (b) ASTM seawater, and (c) 0.5 M Na_2SO_4 solution

Figures 6.14 and 6.15 show Raman spectroscopy of distinct zones of FSW AA6061-AA6061 after 90 and 120 days immersion in 3.15 wt% NaCl, ASTM seawater, and 0.5 M Na_2SO_4 solution, respectively. In Figure 6.14 (a) and Figure 6.15 (a), $Al(OH)_3$ was the corrosion product of five distinct regions immersed for 90 and 120 days in 3.15 wt% NaCl . The Raman intensity of characteristic bands increased as the immersion time increased. In Figure 6.14 (b) and Figure 6.15 (b), characteristic bands of $Al(OH)_3$ (435 and 459 cm^{-1}) and Na_2SO_4 (982 cm^{-1}) were observed in the five distinct regions immersed in ASTM seawater. A characteristic band (237 cm^{-1}) was found only in Figure

15 (b). In Figure 6.14 (c), the characteristic bands of Na_2SO_4 (457, 615, 636, 982, 996, 1075, 1131, and 1151 cm^{-1}) were observed on the TMAZ, BM, and NZ, while only characteristic bands of Na_2SO_4 (982 and 996 cm^{-1}) were observed in the HAZ and downside regions. As shown in Figure 6.14 (c), the characteristic band that we did not mark was ghost band [68-70]. Raman spectra bands of $Al(OH)_3$ for FSW AA6061-AA6061 after immersion 90 days in 0.5 M Na_2SO_4 solution were also missing because the amount of corrosion product may have been insufficient to generate Raman peaks. As shown in Figure 6.15 (c), characteristic bands of $Al(OH)_3$ (237, 322, and 457 cm^{-1}) and Na_2SO_4 (615, 636, 996, 1100, 1131, and 1151 cm^{-1}) were observed in five regions, a finding that tells us that the amount of $Al(OH)_3$ increased for FSW 6061-6061 coupons immersed in 0.5 M Na_2SO_4 solution from 90 to 120 days. There were also characteristic bands (1075 and 1198 cm^{-1}) that cannot be identified.

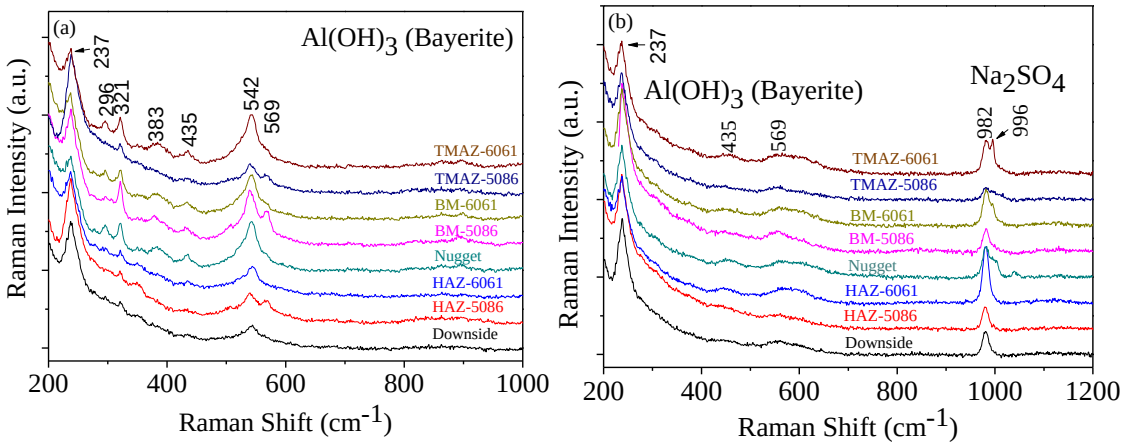

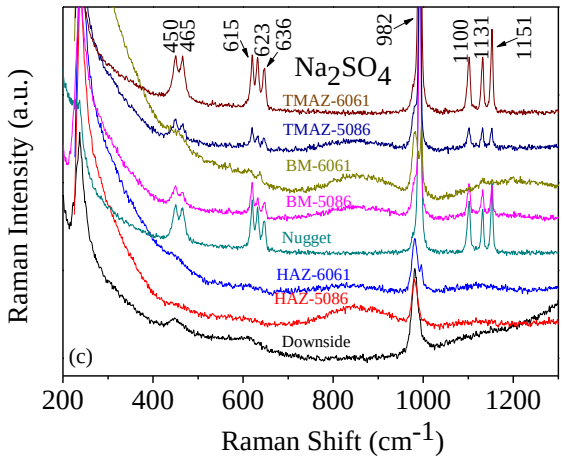

Figure 6.16 Raman spectroscopy of distinct zones of FSW AA5086-AA6061 after 90 days immersion in: (a) 3.15 wt% NaCl, (b) ASTM seawater, and (c) 0.5 M Na_2SO_4 solution

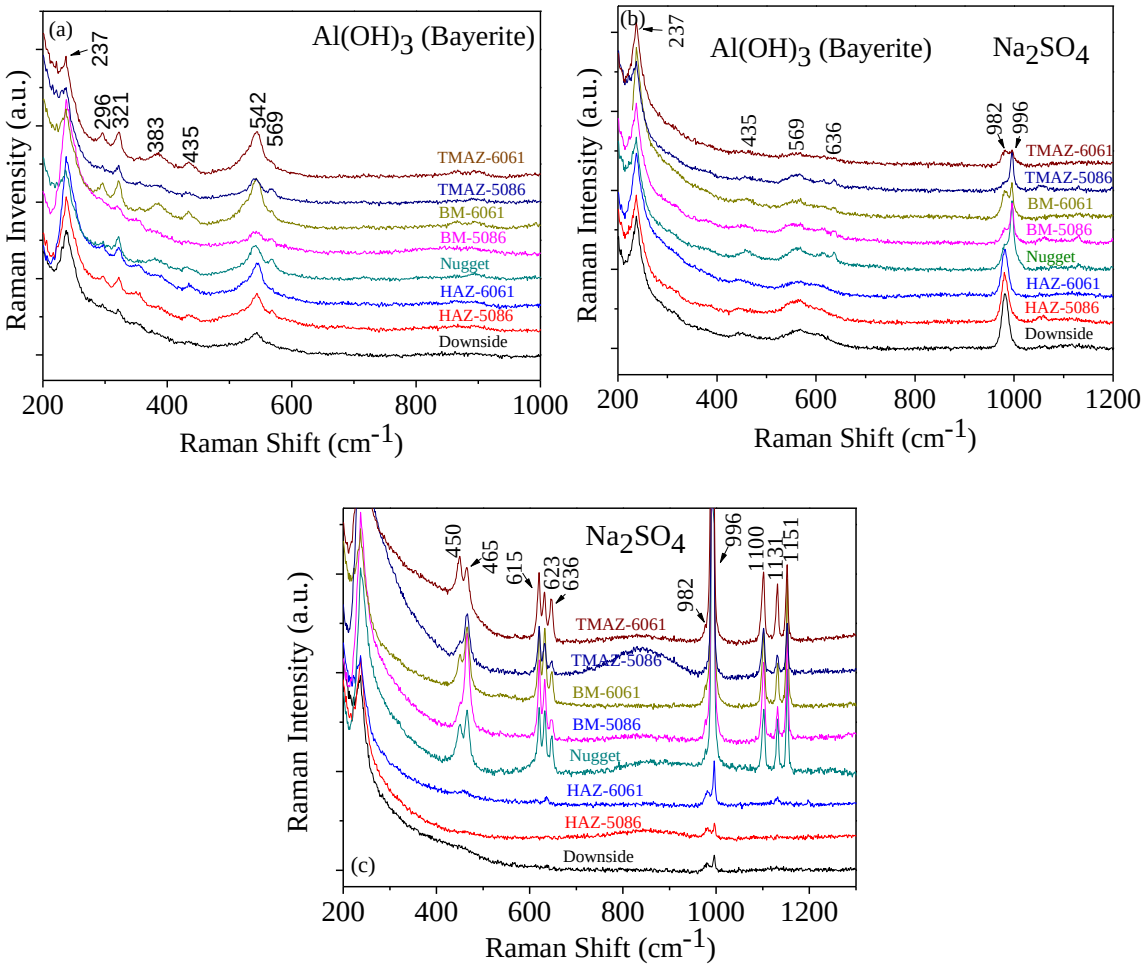

Figure 6.17 Raman spectroscopy of distinct zones of FSW AA5086-AA6061 after 120 days immersion in: (a) 3.15 wt% NaCl, (b) ASTM seawater, and (c) 0.5 M Na_2SO_4 solution

Figures 6.16 and 6.17 show Raman spectra of distinct zones of FSW AA5086-AA6061 after 90 and 120 days immersed in 3.15 wt% NaCl, ASTM seawater, and 0.5 M Na_2SO_4 solution. Due to dissimilar alloys that were welded together, the TMAZ, BM, and HAZ should be different on the AA5086 and AA6061 sides for FSW AA5086-AA6061. Therefore, we characterized both the AA5086 and AA6061 sides for TMAZ, BM, and HAZ via Raman spectroscopy. In Figure 6.16 (a) and Figure 6.17 (a), characteristic bands of $Al(OH)_3$ (237, 296, 321, 383, 435, 542, and 569 cm^{-1}) were observed for distinct regions. TMAZ-AA5086, BM-AA5086, and HAZ-AA5086 had lower Raman intensity than the 6061 side, because there was less corrosion product on the AA5086 side, as shown in Figure 6.4. In Figure 6.16 (b) and Figure 6.17 (b), characteristic bands of $Al(OH)_3$ (237, 435, 569, and 636 cm^{-1}) and Na_2SO_4 (982, and 996 cm^{-1}) were observed for all regions of FSW AA5086-AA6061 immersed in 0.5 M Na_2SO_4 solution. In Figure 6.16 (c) and Figure 6.17 (c), characteristic bands of Na_2SO_4 were observed in TMAZ-AA6061, TMAZ-AA5086, BM-AA6061, BM-AA5086, and NZ. However, only bands of 982 and 996 cm^{-1} were found in the regions of HAZ-AA6061, HAZ-AA5086, and downside. Raman data of $Al(OH)_3$ bands for FSW AA5086-AA6061 coupons immersed in 0.5 M Na_2SO_4 solution were still missing, probably because there was insufficient corrosion product present.

6.6 Scanning Electron Microscopy

A Hitachi S-3400N SEM equipped with an Oxford Instruments energy dispersive X-ray analyzer (EDXA) system was used to characterize the corrosion products of FSW AA5086-AA5086, AA6061-AA6061, and AA5086-AA6061 after being immersed for 90 and 120 days in 3.15 wt% NaCl, ASTM seawater, and 0.5 M Na_2SO_4 solution. We also

characterized five distinct regions: TMAZ, HAZ, NZ, BM, and downside. The results of SEM/EDXA were viewed as supplementary to the Raman and XRD analysis. The following figures and tables depict the results obtained via SEM/EDXA for 90 days of immersion.

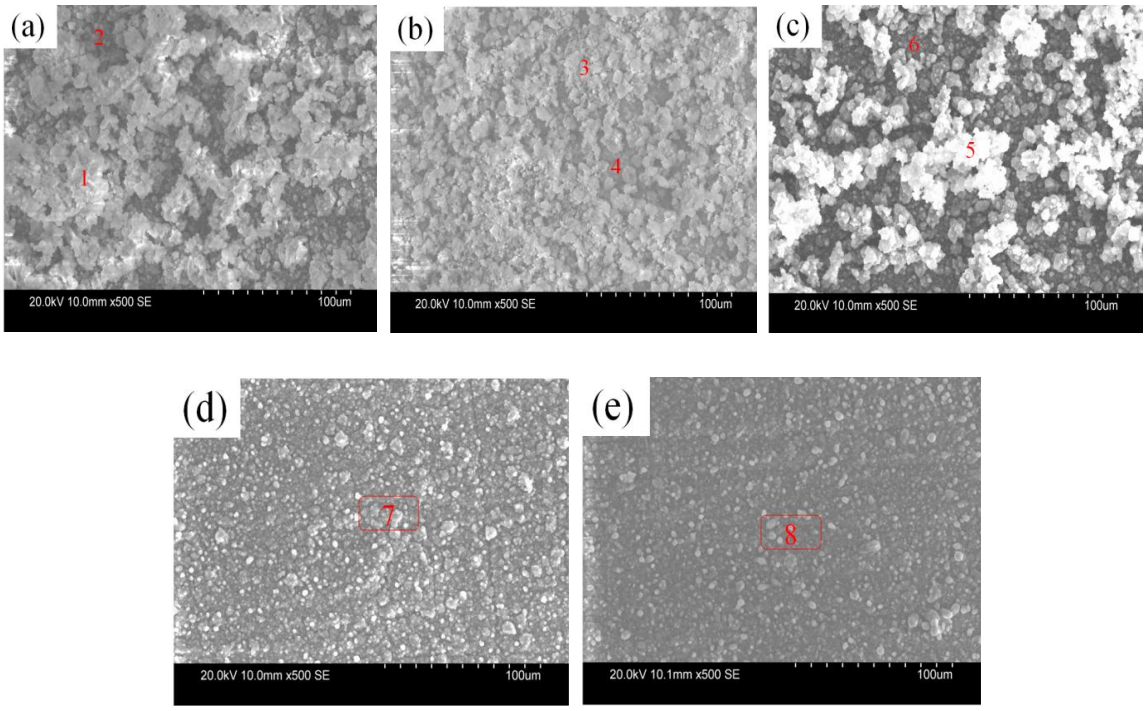

Figure 6.18 SEM of FSW AA5086-AA5086 after 90 days of immersion in 3.15 wt% NaCl: (a) TMAZ, (b) BM, (c) Nugget, (d) HAZ, and (f) downside

Table 6.2 EDXA quantification results of eight points in Figure 6.18

Element [at. %]	C	O	Na	Al	Cl	Mn	Yb
Spectrum 1 (TMAZ)	2.76	69.88	0.18	26.74	0.35	0.09	0.00
Spectrum 2 (TMAZ)	0.00	74.90	0.00	20.56	2.46	1.27	0.81
Spectrum 3 (BM)	4.16	69.38	0.65	25.19	0.63	0.00	0.00
Spectrum 4 (BM)	1.93	74.67	0.34	22.25	0.82	0.00	0.00
Spectrum 5 (NZ)	3.06	73.01	0.29	23.23	0.33	0.07	0.00
Spectrum 6 (NZ)	0	75.36	0.24	23.06	1.35	0.00	0.00
Spectrum 7 (HAZ)	4.36	74.91	0.00	20.40	0.32	0.00	0.00
Spectrum 8 (Downside)	1.93	74.67	0.34	22.25	0.82	0.00	0.00

Figure 6.18 shows the SEM of five regions (TMAZ, BM, Nugget, HAZ, and downside) of FSW 5086-5086 after 90 days of immersion in 3.15 wt% NaCl. EDXA quantification results shown in Table 6.2 reveal corrosion product high in oxygen and aluminum, which agrees with the XRD (Figure 6.6 (a)) and Raman results (Figure 6.12 (a)). The main corrosion product on the five regions was $Al(OH)_3$. As shown in Figure 6.18, there was more corrosion product in the TMAZ, BM, and NZ than in the HAZ and downside, which means that the corrosion resistance of the HAZ was better than the TMAZ, BM, and NZ. The low corrosion on the downside could be caused by the microstructure or the specimen orientation. For FSW 5086-5086 after 120 days immersion in 3.15 wt% NaCl, ASTM seawater, and 0.5 M Na_2SO_4 solution, oxygen concentration in five regions increased but aluminum concentration decreased. The main corrosion product of five regions was still $Al(OH)_3$ (Figure 6.7 (a) and Figure 6.13 (a)).

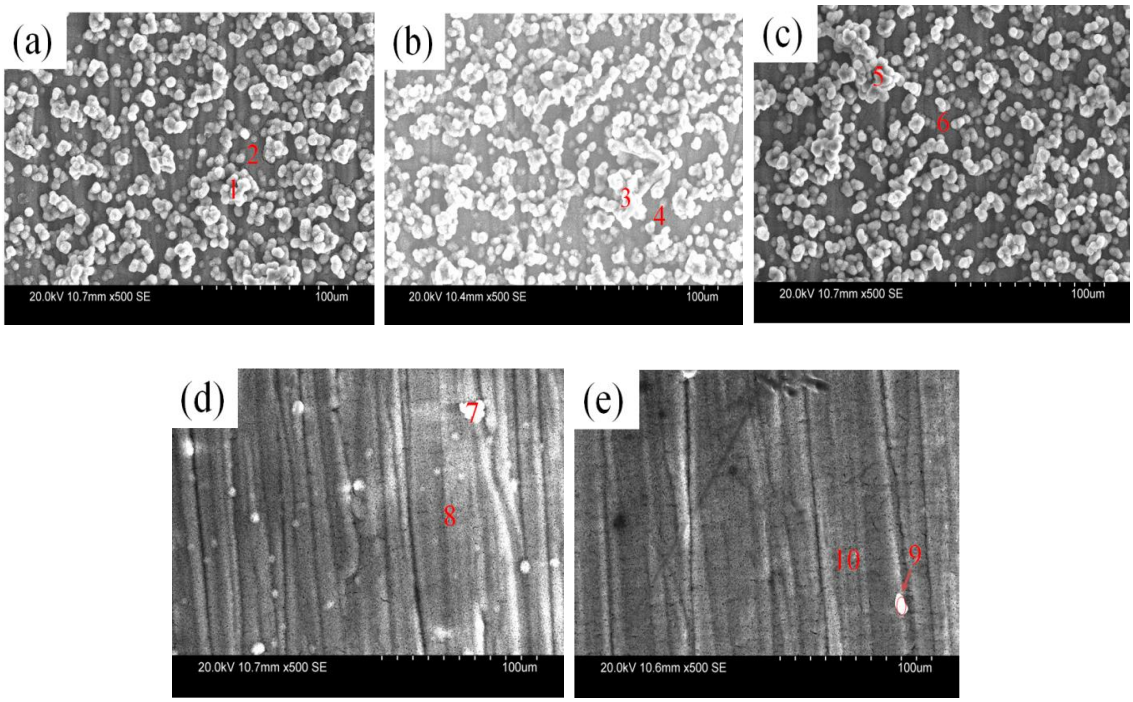

Figure 6.19 SEM of FSW AA5086-AA5086 after 90 days immersion in ASTM seawater: (a) TMAZ, (b) BM, (c) Nugget, (d) HAZ, and (f) downside

Table 6.3 EDXA quantification results of ten points in Figure 6.19

Element [at. %]	S	O	Na	Al	Cl	Mg	Yb
Spectrum 1 (TMAZ)	2.13	67.61	2.47	17.15	4.40	5.79	0.46
Spectrum 2 (TMAZ)	3.42	66.43	3.65	13.35	6.46	6.69	0.00
Spectrum 3 (BM)	2.55	63.39	7.40	10.84	8.15	6.07	1.60
Spectrum 4 (BM)	2.76	59.27	6.42	16.51	8.46	5.90	0.67
Spectrum 5 (NZ)	3.11	67.65	4.29	12.85	5.11	6.98	0.00
Spectrum 6 (NZ)	5.34	69.26	0.00	18.93	0.00	0.00	6.47
Spectrum 7 (HAZ)	3.05	72.14	0.55	19.14	1.53	2.84	0.75
Spectrum 8 (HAZ)	2.40	65.82	0.37	23.34	0.91	5.12	2.04
Spectrum 9 (downside)	4.67	62.10	5.47	14.52	8.48	4.65	0.11
Spectrum 10 (downside)	2.72	66.82	0.59	22.23	1.28	6.07	0.29

Figure 6.19 shows the SEM of five regions (TMAZ, BM, NZ, HAZ, and downside) of FSW 5086-5086 after 90 days immersion in ASTM seawater. There was more corrosion product on the surface of the TMAZ, BM, and Nugget than on the HAZ and downside. EDXA quantification results in Table 6.3 reveal that the corrosion product was also high in oxygen and aluminum. Sulfur and magnesium came from the immersion solution (ASTM seawater), which must have remained on the coupons. The oxygen concentration of coupons in ASTM seawater was lower than those immersed in 3.15 wt% NaCl. The oxygen concentration in five distinct regions immersed for 90 days to 120 days also increased (Appendix). SEM/EDXA results agree with the results of XRD and Raman.

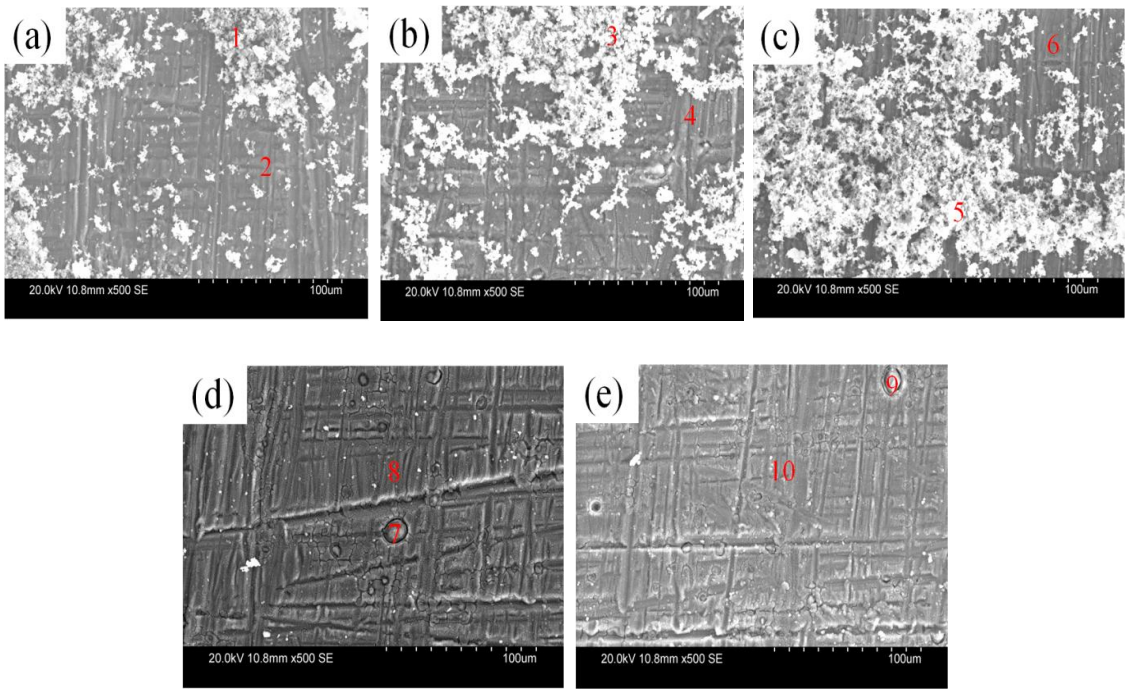

Figure 6.20 SEM of FSW AA5086-AA5086 after 90 days immersion in 0.5 M Na_2SO_4 (a) TMAZ, (b) BM, (c) Nugget, (d) HAZ, and (f) downside

Table 6.4 EDXA quantification results of ten points in Figure 6.20

Element [at. %]	S	O	Na	Al	C	Mg
Spectrum 1 (TMAZ)	7.20	59.53	11.71	12.80	8.77	0.00
Spectrum 2 (TMAZ)	0.96	28.85	0.81	66.29	0.00	3.09
Spectrum 3 (BM)	5.18	65.85	10.31	12.91	5.23	0.52
Spectrum 4 (BM)	0.77	28.83	0.58	61.65	5.28	2.89
Spectrum 5 (NZ)	8.21	66.00	15.49	10.30	0.00	0.00
Spectrum 6 (NZ)	0.66	26.78	0.67	68.56	0.00	3.33
Spectrum 7 (HAZ)	3.24	65.85	2.29	20.57	8.05	0.00
Spectrum 8 (HAZ)	0.49	31.57	0.00	64.95	0.00	2.99
Spectrum 9 (downside)	1.36	54.93	1.55	35.72	6.44	0.00
Spectrum 10 (downside)	0.40	24.16	0.38	71.79	0.00	3.27

The SEM of five regions of FSW 5086-5086 after 90 days immersion in 0.5 M Na_2SO_4 solution is shown in Figure 6.20. The EDXA analysis depicted in Table 6.4 revealed that the corrosion product was high in oxygen and aluminum. According to the XRD results (Figure 6.6 (c)) and Raman analysis (Figure 6.12 (c)), the white particles on the surface of the TMAZ, BM, and NZ was Na_2SO_4. Pits with different sizes were also observed in the HAZ (Figure 6.20 (d)) and the downside regions (Figure 6.20 (e)). The pits around the constituent particles likely formed as a result of cathodic reduction [4]. Cathodic reduction on the constituent particles can increase the alkalinity in the surrounding solution, leading to the dissolution of the aluminum matrix. SEM/EDXA results agree with those from the XRD (Figure 6.6 (c)) and Raman analysis (Figure 6.12 (c)).

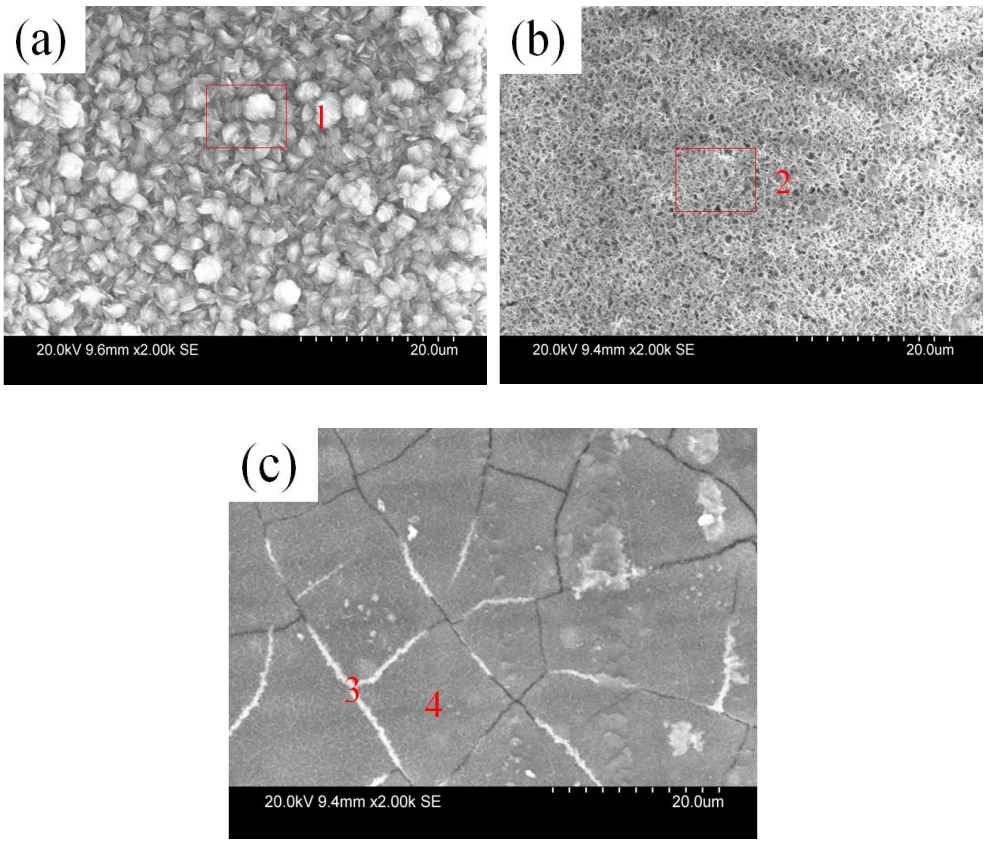

Figure 6.21 SEM of downside region of FSW AA6061-AA6061 after 90 days immersion in (a) 3.15 wt% NaCl, (b) ASTM seawater, and (c) 0.5 M Na_2SO_4 solution

Table 6.5 EDXA quantification results of four points in Figure 6.21

Element [at. %]	S	O	Na	Al	C	Cl	Mg
Spectrum 1	0.00	77.27	0.00	22.45	0.00	0.28	0.00
Spectrum 2	2.11	70.43	0.26	22.07	0.00	0.88	4.04
Spectrum 3	1.50	57.38	2.39	11.90	26.83	0.00	0.00
Spectrum 4	2.08	56.14	2.34	34.72	4.72	0.00	0.00

SEM of downside region of FSW AA6061-AA6061 after 90 days in 3.15 wt% NaCl, ASTM seawater, and 0.5 M Na_2SO_4 is shown in Figure 6.21. As shown in Figure 6.21, the structure of the corrosion products was largest in the 3.15 wt% NaCl. There were many pits on the coupon surfaces after 90 days immersion in ASTM seawater (Figure 6.21(b)). Cracking was found on the downside region of FSW AA6061-AA6061 after immersion in 0.5 M Na_2SO_4 solution (Figure 6.21(c)). The cracking could be either in the corrosion product film or in the metallic alloy. The specimens have to be cleaned to determine the actual region of the cracking. If cracking occurred in the metallic alloy, the following three condition would have to be met [71]: 1) the presence of a corrosive medium, 2) a difference in potential in the order of 100 mV, and 3) a continuous network of intermetallics at the grain boundaries. In Table 6.5, quantitative EDXA results reveal corrosion product high in oxygen and aluminum. The oxygen concentration of the coupon immersed in 3.15 wt% NaCl was higher than that in ASTM seawater, while the aluminum concentration was similar. SEM/EDXA results agreed with XRD and Raman results.

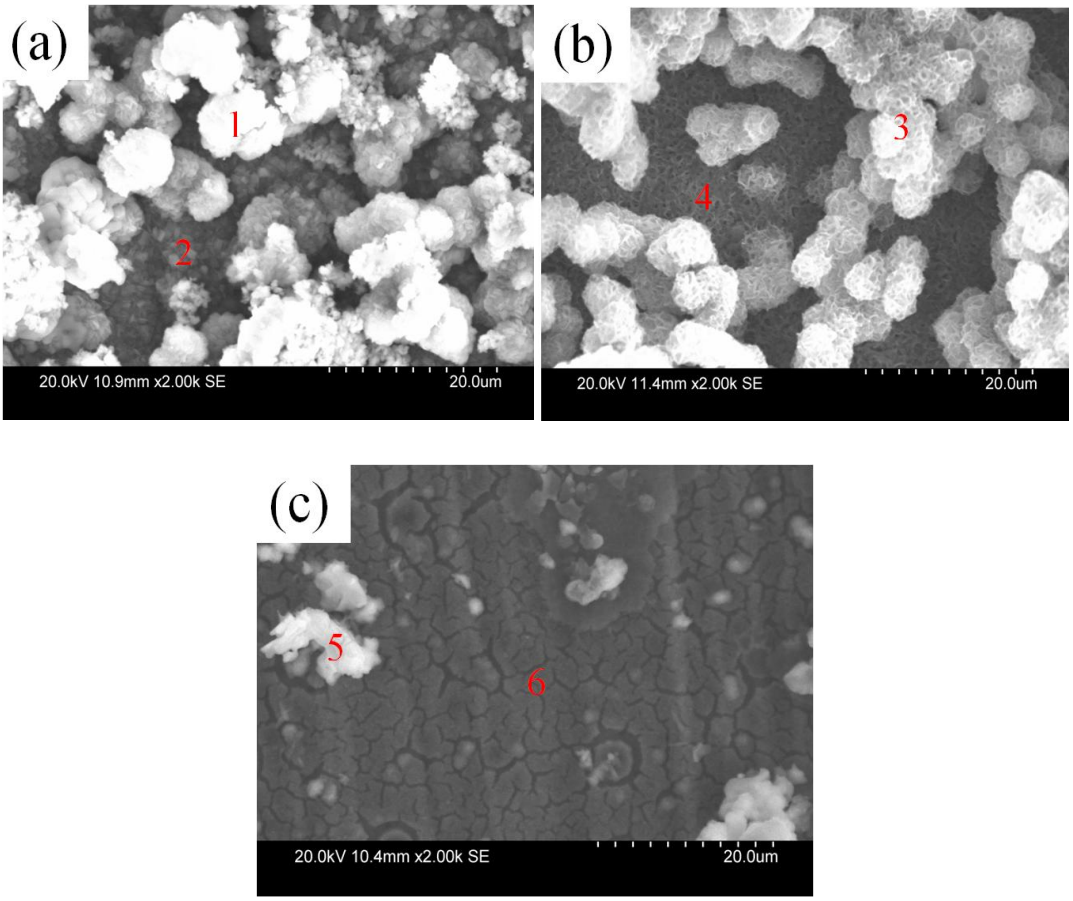

Figure 6.22 SEM of NZ of FSW AA5086-AA6061 after 120 days immersion in (a) 3.15 wt% NaCl, (b) ASTM seawater, and (c) 0.5 M Na_2SO_4 solution

Table 6.6 EDXA quantification results of six points in Figure 6.22

Element [at. %]	S	O	Na	Al	Cl	Mg
Spectrum 1	0.00	78.34	1.09	19.55	1.03	0.00
Spectrum 2	0.00	66.12	0.80	29.98	3.10	0.00
Spectrum 3	2.59	66.89	4.27	10.84	5.81	9.61
Spectrum 4	4.30	54.01	0.00	21.87	12.56	7.26
Spectrum 5	10.34	62.70	22.88	4.08	0.00	0.00
Spectrum 6	1.42	41.30	1.55	55.73	0.00	0.00

Figure 6.22 shows SEM of NZ of FSW AA5086-AA6061 after 120 days immersion in 3.15 wt% NaCl, ASTM seawater, and 0.5 M Na_2SO_4 solution. The EDXA analysis depicted in Table 6.6 revealed corrosion product high in oxygen and aluminum. According to XRD results (Figure 6.11) and Raman analysis (Figure 6.17), the corrosion products on the surface of the coupon immersed in 3.15 wt% NaCl (Figure 22 (a)) and ASTM seawater (Figure 22 (b)) was $Al(OH)_3$. A denser layer of corrosion products appeared to cover the coupon exposed in the NaCl solution (Figure 22 (a)) as compared to the coupon exposed in the ASTM seawater (Figure 22 (b)). The oxygen concentration of the two locations shown in Figure 22 (a) (specimen previously exposed to NaCl solution) was also higher than in Figure 22 (b) (specimen previously exposed to the ASTM solution). As shown in Figure 6.22 (c), cracking on the surface of the specimen exposed to the 0.5 M Na_2SO_4 solution was also found. The cracks are likely to be in the aluminum oxide corrosion layer.

6.7 Weight Loss

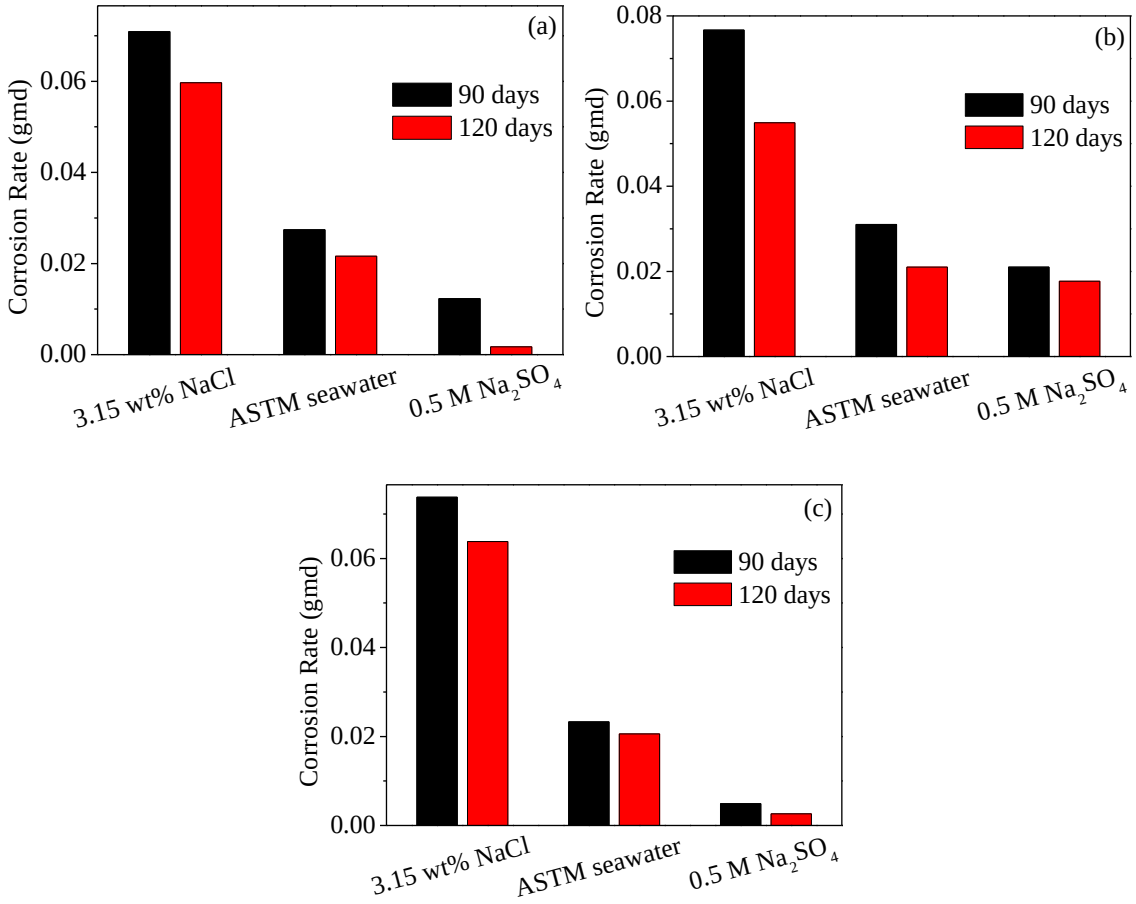

Figure 6.23 Corrosion Rate of specimens after 90 and 120 days immersion in 3.15 wt% NaCl, ASTM seawater, and 0.5 M Na_2SO_4 solution for (a) FSW AA5086-AA5086, (b) FSW AA6061-AA6061, and (c) FSW AA5086-AA6061

The results of corrosion rate of FSW AA5086-AA5086, FSW AA6061-AA6061, and FSW AA5086-AA6061 by weight measurement are shown in Figure 6.23. The corrosion rate of FSW AA-5086-AA5086, FSW AA6061-AA6061, and FSW AA5086-AA6061 decreased from 90 days to 120 days in three solutions. The corrosion rate of FSW AA-5086-AA5086, FSW AA6061-AA6061, and FSW AA5086-AA6061 from highest to lowest for three solutions was as follows: 3.15 wt% NaCl > ASTM seawater > 0.5 M Na_2SO_4. The maximum value of corrosion rate was obtained from FSW AA6061-AA6061 in 3.15 wt% NaCl solution after 90 days immersion. In 3.15 wt% NaCl solution

after 90 days immersion, the corrosion rate of FSW AA6061-AA6061 and FSW AA5086-AA6061 was higher than that of FSW AA5086-AA5086 because AA6061 corroded at a higher rate than AA 5086 from Figure 6.2, Figure 6.3, and Figure 6.4.

Chapter 7

Summary

In this study, the microstructure, mechanical properties, and corrosion behavior of FSW AA5086 and AA6061 aluminum alloys were examined. For the microstructure of FSW AA6061-AA6061, the grains within the NZ were much smaller than the grain in other regions. The order of average grain size in different weld zones was as follow: BM > HAZ > cross-section > downside > TMAZ > NZ.

For FSW AA5086-AA5086, the minimum hardness (107.7 HV) was obtained in the TMAZ/HAZ regions, and the maximum value (115.8 HV) occurred in the BM. All FSW AA5086-AA5086 specimens showed significant decreases in both tensile and yield strengths, while the ductility increased. The tensile specimens of FSW AA5086-AA5086 failed in the TMAZ/HAZ regions. In deaerated 3.15 wt% NaCl solution, the potential E_{corr} and E_{pit} of the different weld zones shifted to more positive values from the BM (-953 mV_{SCE}). The minimum value of I_{corr} appeared in the HAZ region. In aerated 3.15 wt% NaCl, the various weld zones of FSW AA5086-AA5086 show Tafel behavior. The I_{corr} values of HAZ (0.65 $\mu A/cm^2$) and downside (0.64 $\mu A/cm^2$) were lower and much smaller than the other regions. For the 90 and 120 day immersion tests of the FSW AA5086-AA5086, the highest amount of corrosion products formed in 3.15 wt% NaCl, followed by that in the ASTM seawater, and then in 0.5 M Na_2SO_4. The welded region of the FSW AA5086-AA5086 coupons became dark in color after being immersed in 3.15 wt% NaCl for 90 and 120 days. XRD and Raman results revealed that $Al(OH)_3$ (bayerite) was the main corrosion product on the FSW AA5086-AA5086 coupons immersed in the three

solutions. Quantitative EDXA results revealed that the corrosion products were high in oxygen and aluminum. The corrosion resistance of the HAZ and downside was better than that of the TMAZ, BM, and NZ. The oxygen concentration in the weld zones increased with immersion time; whereas, the concentration of aluminum decreased with immersion time. This was likely caused by the thickening of the bayerite layer, which impeded the electron beam from entering the substrate aluminum, thereby limiting the Al X-ray signal to originate only from the bayerite layer.

For FSW AA6061-AA6061, the minimum hardness of 85.0 HV was obtained in the HAZ region, and the maximum value of 106.5 HV was present in the BM. The tensile and yield strengths of the FSW AA6061-AA6061 tensile specimens were less than that of the BM tensile specimens. In comparisons to the properties of the BM, the ductility of FSW AA6061-AA6061 increased in the longitudinal tensile test specimens (that consisted of the NZ), but decreased in the transverse tensile specimens that cut through all of the weld zones. Fracture occurred in the HAZ region, which had the lowest hardness of all of the weld zones. In deaerated 3.15 wt% NaCl solutions, the various weld zones of FSW AA6061-AA6061 showed a passive region that was larger than that in FSW AA5086-AA5086. The potential E_{corr}, and E_{pit} shifted to more positive values, and the current I_{corr} decreased to values that were lower than that of the BM (E_{corr} = -1114 mV_{SCE}, E_{pit} = - 724 mV_{SCE}, I_{corr} = 2.44 $\mu A/cm^2$). The minimum value of I_{corr} appeared in the HAZ (0.76 $\mu A/cm^2$) region. During cathodic polarization in aerated 3.15 wt% NaCl, the various weld zones of FSW AA6061-AA6061 showed diffusion-limited oxygen reduction as the predominant cathodic reaction. The potential E_{corr} shifted to more positive potentials, and the current I_{corr} decreased to values lower than that of the BM (E_{corr} = -750 mV_{SCE}, I_{corr} =

8.57 μA/cm^2). The minimum value of I_{corr} appeared in the HAZ (2.87 μA/cm^2) region. The BM of FSW AA6061-AA6061 coupons became much blacker in appearance than did the welded region in 3.15 wt% NaCl after 90 days immersion. XRD and Raman results revealed $Al(OH)_3$ as the main corrosion product on FSW AA6061-AA6061 coupons immersed in the three solutions. Quantitative EDXA results revealed that the corrosion products were high in oxygen and aluminum. Cracking was observed in the downside region of FSW AA6061-AA6061 after 90 days immersion in the 0.5 M Na_2SO_4 solution. The cracking was likely in the bayerite layer. The corrosion resistance of the HAZ and downside was better than in the TMAZ, BM, and NZ. Based on the EDXA results of the various weld zones, the oxygen concentration increased, but the aluminum concentration decreased as immersion time increased. This was likely due to the thickening of the bayerite layer.

For FSW AA5086-AA6061, the minimum hardness of 88 HV was obtained in the HAZ region of AA6061 side, and the maximum value of 113.2 HV occurred in the BM of the AA5086 section. Compared with BM-AA5086 and BM-AA6061, the tensile and yield strengths of the FSW AA5086-AA6061 show significant decreases. The ductility of FSW AA5086-AA6061 increased in the longitudinal direction (that contained the NZ), but it decreased in the transverse direction that cut through all weld zones. The tensile specimens of FSW AA5086-AA6061 failed in the HAZ region of the AA6061 section. In deaerated 3.15 wt% NaCl solutions, the E_{corr} values of the weld zones of FSW AA5086-AA6061 shifted to more positive potentials compared to those of the BM-AA5086 and BM-AA6061. The E_{corr} values of the NZ (-962 mV_{SCE}) was between those of the BM-AA5086 and the BM-AA6061. The current I_{corr} values for the various weld zones

decreased from that of the BM-AA5086 (1.70 μA/cm^2) and BM 6061 (2.44 μA/cm^2). The minimum value of I_{corr} appeared in the HAZ-AA5086 (0.54 μA/cm^2) region. In aerated 3.15 wt% NaCl during cathodic polarization, the weld zones on theAA6061 side showed diffusion-limited oxygen reduction behavior; whereas, the cross-section, downside, and weld zones on the AA5086 side show Tafel behavior. The current I_{corr} of the weld zones decreased from that of the BM-AA5086 (1.27 μA/cm^2) (Figure 6.20 (e)) and BM-AA6061 (8.57 μA/cm^2). In 3.15 wt% NaCl and ASTM seawater, the BM-AA6061 side was much darker than the BM-AA5086 side. XRD and Raman results revealed $Al(OH)_3$ as the main corrosion product on FSW AA5086-AA5086 coupons immersed in the three solutions. Quantitative EDXA results revealed that the corrosion products were high in oxygen and aluminum. Cracks were found on the surface of the NZ region after 120 days immersion in the 0.5 M Na_2SO_4 solution. The cracks were likely in the bayerite corrosion products. The corrosion resistance of the HAZ and downside was better than that of the TMAZ, BM, and NZ. Oxygen concentration in the eight weld sections increased as the immersion time increased; whereas, the aluminum concentration decreased with immersion time, which was likely caused by the thickening of the bayerite layer.

References

[1] W.M. Thomas, E.D. Nicholas, J.C. Needham, M.G. Murch, P. Temple-Smith, C.J. Dawes, Friction Welding, in: United States Patent, 460,317, The Welding Institute, Cambridge, GB (Ed.), 1995.

[2] M. Ericsson, R. Sandström, Influence of welding speed on the fatigue of friction stir welds, and comparison with MIG and TIG, International Journal of Fatigue, 25 (2003) 1379-1387.

[3] E. Bousquet, A. Poulon-Quintin, M. Puiggali, O. Devos, M. Touzet, Relationship between microstructure, microhardness and corrosion sensitivity of an AA 2024-T3 friction stir welded joint, Corrosion Science, 53 (2011) 3026-3034.

[4] M. Jariyaboon, A.J. Davenport, R. Ambat, B.J. Connolly, S.W. Williams, D.A. Price, The effect of welding parameters on the corrosion behaviour of friction stir welded AA2024–T351, Corrosion Science, 49 (2007) 877-909.

[5] W.M. Thomas, E.D. Nicholas, Friction stir welding for the transportation industries, Materials & Design, 18 (1997) 269-273.

[6] S.W. Williams, Welding of airframes using friction stir, Air & Space Europe, 3 (2001) 64-66.

[7] B.R. Ghosh, R.K. Gupta, S. Biju, P.P. Sinha, Modified Welding Technique of a Hypo-Eutectic Al-Cu Alloy for Higher Mechanical Properties, Journal of Solid Mechanics and Materials Engineering, 1 (2007) 469-479.

[8] K.S. Rao, G.M. Reddy, K.P. Rao, Studies on partially melted zone in aluminium–copper alloy welds—effect of techniques and prior thermal temper, Materials Science and Engineering: A, 403 (2005) 69-76.

[9] R.A. Prado, L.E. Murr, D.J. Shindo, K.F. Soto, Tool wear in the friction-stir welding of aluminum alloy 6061+20% Al2O3: a preliminary study, Scripta Materialia, 45 (2001) 75-80.

[10] J.Q. Su, T.W. Nelson, R. Mishra, M. Mahoney, Microstructural investigation of friction stir welded 7050-T651 aluminium, Acta Materialia, 51 (2003) 713-729.

[11] S. Benavides, Y. Li, L.E. Murr, D. Brown, J.C. McClure, Low-temperature friction-stir welding of 2024 aluminum, Scripta Materialia, 41 (1999) 809-815.

[12] D. Field, T. Nelson, Y. Hovanski, K. Jata, Heterogeneity of crystallographic texture in friction stir welds of aluminum, Metall and Mat Trans A, 32 (2001) 2869-2877.

[13] L.E. Murr, G. Liu, J.C. McClure, Dynamic recrystallization in friction-stir welding of aluminium alloy 1100, Journal of Materials Science Letters, 16 (1997) 1801-1803.

[14] G. İpekoğlu, S. Erim, G. Çam, Investigation into the Influence of Post-Weld Heat Treatment on the Friction Stir Welded AA6061 Al-Alloy Plates with Different Temper Conditions, Metall and Mat Trans A, 45 (2014) 864-877.

[15] D.A. Wadeson, X. Zhou, G.E. Thompson, P. Skeldon, L.D. Oosterkamp, G. Scamans, Corrosion behaviour of friction stir welded AA7108 T79 aluminium alloy, Corrosion Science, 48 (2006) 887-897.

[16] J.B. Lumsden, M.W. Mahoney, G. Pollock, C.G. Rhodes, Intergranular Corrosion Following Friction Stir Welding of Aluminum Alloy 7075-T651, Corrosion, 55 (1999) 1127-1135.

[17] Y. Li, L.E. Murr, J.C. McClure, Flow visualization and residual microstructures associated with the friction-stir welding of 2024 aluminum to 6061 aluminum, Materials Science and Engineering: A, 271 (1999) 213-223.

[18] K.V. Jata, S.L. Semiatin, Continuous dynamic recrystallization during friction stir welding of high strength aluminum alloys, Scripta Materialia, 43 (2000) 743-749.

[19] M.A. Sutton, B. Yang, A.P. Reynolds, R. Taylor, Microstructural studies of friction stir welds in 2024-T3 aluminum, Materials Science and Engineering: A, 323 (2002) 160-166.

[20] L.E. Murr, G. Liu, J.C. McClure, A TEM study of precipitation and related microstructures in friction-stir-welded 6061 aluminium, Journal of Materials Science, 33 (1998) 1243-1251.

[21] M.A. Sutton, A.P. Reynolds, B. Yang, R. Taylor, Mode I fracture and microstructure for 2024-T3 friction stir welds, Materials Science and Engineering: A, 354 (2003) 6-16.

[22] H.G. Salem, Friction stir weld evolution of dynamically recrystallized AA 2095 weldments, Scripta Materialia, 49 (2003) 1103-1110.

[23] K.A.A. Hassan, A.F. Norman, D.A. Price, P.B. Prangnell, Stability of nugget zone grain structures in high strength Al-alloy friction stir welds during solution treatment, Acta Materialia, 51 (2003) 1923-1936.

[24] C.S. Paglia, R.G. Buchheit, A look in the corrosion of aluminum alloy friction stir welds, Scripta Materialia, 58 (2008) 383-387.

[25] R.W. Fonda, P.S. Pao, H.N. Jones, C.R. Feng, B.J. Connolly, A.J. Davenport, Microstructure, mechanical properties, and corrosion of friction stir welded Al 5456, Materials Science and Engineering: A, 519 (2009) 1-8.

[26] D. Rao, K. Huber, J. Heerens, J.F. dos Santos, N. Huber, Asymmetric mechanical properties and tensile behaviour prediction of aluminium alloy 5083 friction stir welding joints, Materials Science and Engineering: A, 565 (2013) 44-50.

[27] M. Peel, A. Steuwer, M. Preuss, P.J. Withers, Microstructure, mechanical properties and residual stresses as a function of welding speed in aluminium AA5083 friction stir welds, Acta Materialia, 51 (2003) 4791-4801.

[28] W. Xu, J. Liu, G. Luan, C. Dong, Temperature evolution, microstructure and mechanical properties of friction stir welded thick 2219-O aluminum alloy joints, Materials & Design, 30 (2009) 1886-1893.

[29] I. Dinaharan, K. Kalaiselvan, S.J. Vijay, P. Raja, Effect of material location and tool rotational speed on microstructure and tensile strength of dissimilar friction stir welded aluminum alloys, Archives of Civil and Mechanical Engineering, 12 (2012) 446-454.

[30] D.H. Jeong, U. Erb, K.T. Aust, G. Palumbo, The relationship between hardness and abrasive wear resistance of electrodeposited nanocrystalline Ni–P coatings, Scripta Materialia, 48 (2003) 1067-1072.

[31] W. Xu, J. Liu, Microstructure and pitting corrosion of friction stir welded joints in 2219-O aluminum alloy thick plate, Corrosion Science, 51 (2009) 2743-2751.

[32] P.B. Srinivasan, K.S. Arora, W. Dietzel, S. Pandey, M.K. Schaper, Characterisation of microstructure, mechanical properties and corrosion behaviour of an AA2219 friction stir weldment, Journal of Alloys and Compounds, 492 (2010) 631-637.

[33] K.A.A. Hassan, P.B. Prangnell, A.F. Norman, D.A. Price, S.W. Williams, Effect of welding parameters on nugget zone microstructure and properties in high strength aluminium alloy friction stir welds, Science and Technology of Welding and Joining, 8 (2003) 257-268.

[34] J.-H. Cho, W. Jae Kim, C. Gil Lee, Texture and microstructure evolution and mechanical properties during friction stir welding of extruded aluminum billets, Materials Science and Engineering: A, 597 (2014) 314-323.

[35] Y. Sato, S. Park, H. Kokawa, Microstructural factors governing hardness in friction-stir welds of solid-solution-hardened Al alloys, Metall and Mat Trans A, 32 (2001) 3033-3042.

[36] Y. Sato, H. Kokawa, M. Enomoto, S. Jogan, Microstructural evolution of 6063 aluminum during friction-stir welding, Metall and Mat Trans A, 30 (1999) 2429-2437.

[37] O. Hatamleh, P.M. Singh, H. Garmestani, Corrosion susceptibility of peened friction stir welded 7075 aluminum alloy joints, Corrosion Science, 51 (2009) 135-143.

[38] Z.L. Hu, X.S. Wang, S.J. Yuan, Quantitative investigation of the tensile plastic deformation characteristic and microstructure for friction stir welded 2024 aluminum alloy, Materials Characterization, 73 (2012) 114-123.

[39] M.J. Starink, A. Deschamps, S.C. Wang, The strength of friction stir welded and friction stir processed aluminium alloys, Scripta Materialia, 58 (2008) 377-382.

[40] C. Genevois, A. Deschamps, A. Denquin, B. Doisneau-cottignies, Quantitative investigation of precipitation and mechanical behaviour for AA2024 friction stir welds, Acta Materialia, 53 (2005) 2447-2458.

[41] Y. Chen, H. Liu, J. Feng, Friction stir welding characteristics of different heat-treated-state 2219 aluminum alloy plates, Materials Science and Engineering: A, 420 (2006) 21-25.

[42] T.S. Srivatsan, S. Vasudevan, L. Park, The tensile deformation and fracture behavior of friction stir welded aluminum alloy 2024, Materials Science and Engineering: A, 466 (2007) 235-245.

[43] S.H. Kang, H.-S. Chung, H.N. Han, K.H. Oh, C.G. Lee, S.-J. Kim, Relationship between formability and microstructure of Al alloy sheet locally modified by friction stir processing, Scripta Materialia, 57 (2007) 17-20.

[44] K.V. Jata, K.K. Sankaran, J.J. Ruschau, Friction-stir welding effects on microstructure and fatigue of aluminum alloy 7050-T7451, Metall and Mat Trans A, 31 (2000) 2181-2192.

[45] P.B. Srinivasan, W. Dietzel, R. Zettler, J.F. dos Santos, V. Sivan, Stress corrosion cracking susceptibility of friction stir welded AA7075–AA6056 dissimilar joint, Materials Science and Engineering: A, 392 (2005) 292-300.

[46] P.S. Pao, S.J. Gill, C.R. Feng, On fatigue crack initiation from corrosion pits in 7075-T7351 aluminum alloy, Scripta Materialia, 43 (2000) 391-396.

[47] K.K. Sankaran, R. Perez, K.V. Jata, Effects of pitting corrosion on the fatigue behavior of aluminum alloy 7075-T6: modeling and experimental studies, Materials Science and Engineering: A, 297 (2001) 223-229.

[48] F. Zucchi, G. Trabanelli, V. Grassi, Pitting and stress corrosion cracking resistance of friction stir welded AA 5083, Materials and Corrosion, 52 (2001) 853-859.

[49] M. Jariyaboon, A.J. Davenport, R. Ambat, B.J. Connolly, S.W. Williams, D.A. Price, Corrosion of a dissimilar friction stir weld joining aluminium alloys AA2024 and AA7010, Corrosion Engineering, Science & Technology, 41 (2006) 135-142.

[50] C.S. Paglia, K.V. Jata, R.G. Buchheit, The influence of artificial aging on the microstructure, mechanical properties, corrosion, and environmental cracking susceptibility of a 7075 friction-stir-weld, Materials and Corrosion, 58 (2007) 737-750.

[51] R.-C. Zeng, J. Chen, W. Dietzel, R. Zettler, J.F. dos Santos, M. Lucia Nascimento, K.U. Kainer, Corrosion of friction stir welded magnesium alloy AM50, Corrosion Science, 51 (2009) 1738-1746.

[52] G.L. Song, A. Atrens, Corrosion Mechanisms of Magnesium Alloys, Advanced Engineering Materials, 1 (1999) 11-33.

[53] C.S. Paglia, R.G. Buchheit, Microstructure, microchemistry and environmental cracking susceptibility of friction stir welded 2219-T87, Materials Science and Engineering: A, 429 (2006) 107-114.

[54] B. Jeon, S.K.R.S. Sankaranarayanan, A.C.T. van Duin, S. Ramanathan, Atomistic insights into aqueous corrosion of copper, The Journal of Chemical Physics, 134 (2011) -.

[55] C. Punckt, M. Boelscher, H.H. Rotermund, A.S. Mikhailov, L. Organ, N. Budiansky, J.R. Scully, J.L. Hudson, Sudden onset of pitting corrosion on stainless steel as a critical phenomenon, Science (Washington, DC, U. S.), 305 (2004) 1133-1136.

[56] D.E. Williams, R.C. Newman, Q. Song, R.G. Kelly, Passivity breakdown and pitting corrosion of binary alloys, Nature, 350 (1991) 216-219.

[57] G.S. Frankel, Pitting corrosion of metals. A review of the critical factors, J. Electrochem. Soc., 145 (1998) 2186-2198.

[58] ASTM G110-92, Standard Practice for Evaluating Intergranular Corrosion Resistance of Heat Treatable Aluminum Alloys by Immersing in Sodium Chloride þ Hydrogen Peroxide Solution, 1997.

[59] S.J. Kalita, Microstructure and corrosion properties of diode laser melted friction stir weld of aluminum alloy 2024 T351, Applied Surface Science, 257 (2011) 3985-3997.

[60] M. Büchler, T. Watari, W.H. Smyrl, Investigation of the initiation of localized corrosion on aluminum alloys by using fluorescence microscopy, Corrosion Science, 42 (2000) 1661-1668.

[61] M. Buchler, J. Kerimo, F. Guillaume, W.H. Smyrl, Fluorescence and near-field scanning optical microscopy for investigating initiation of localized corrosion of Al 2024, J. Electrochem. Soc., 147 (2000) 3691-3699.

[62] P. Leblanc, G.S. Frankel, A study of corrosion and pitting initiation of AA2024-T3 using atomic force microscopy, J. Electrochem. Soc., 149 (2002) B239-B247.

[63] Raghu Srinivasan. 2010. Correlation studies between outdoor exposure and accelerated laboratory corrosion tests for galvanic and non-galvanic ceramic-aluminum couples. PhD dissertation, University of Hawaii at Manoa. Ann Arbor: ProQuest/UMI. (Publication No. AAT 3448693.).

[64] ASTM International, West Conshohocken, PA, www.astm.org Standard Practice for Preparing, Cleaning, and Evaluating Corrosion Test Specimens. ASTM G1-03. 2003.

[65] W. Xu, J. Liu, G. Luan, C. Dong, Microstructure and mechanical properties of friction stir welded joints in 2219-T6 aluminum alloy, Materials & Design, 30 (2009) 3460-3467.

[66] K. Surekha, B.S. Murty, K.P. Rao, Microstructural characterization and corrosion behavior of multipass friction stir processed AA2219 aluminium alloy, Surface and Coatings Technology, 202 (2008) 4057-4068.

[67] H.D. Ruan, R.L. Frost, J.T. Kloprogge, Comparison of Raman spectra in characterizing gibbsite, bayerite, diaspore and boehmite, Journal of Raman Spectroscopy, 32 (2001) 745-750.

[68] S. Li, Marine atmospheric corrosion initiation and corrosion products characterization, University of Hawaii Manoa, 205 (2010).

[69] S. Li, L.H. Hihara, In situ Raman spectroscopic study of NaC lparticle-induced marine atmospheric corrosion of carbon steel, Journal of the Electrochemical Society, 159 (2012) C147-C154.

[70] S. Li, L.H. Hihara, In situ Raman spectroscopic identification of rust formation in Evans' droplet experiments, Electrochemistry Communications, 18 (2012) 48-50.

[71] C. Vargel, M. Jacques, M.P. Schmidt, Corrosion of Aluminium, Elsevier, 2004, p. 125.